THE SYNTHESIS AND ELECTROCHEMICAL PROPERTIES OF NANOCONFINED LITHIUM TITANATE, TITANIUM OXIDE, IRON FLUORIDE AND OTHER COMPOUNDS

A Dissertation
Presented to
The Academic Faculty

by

Enbo Zhao

In Partial Fulfillment
of the Requirements for the Degree
Doctor of Philosophy in the
School of Chemistry and Biochemistry

Georgia Institute of Technology
December, 2018

THE SYNTHESIS AND ELECTROCHEMICAL PROPERTIES OF NANOCONFINED LITHIUM TITANATE, TITANIUM OXIDE, IRON FLUORIDE AND OTHER COMPOUNDS

Approved by:

Dr. Gleb Yushin, Advisor
School of Materials Science and Engineering
Georgia Institute of Technology

Dr. Seth Marder, Co-Advisor
School of Chemistry and Biochemistry
Georgia Institute of Technology

Dr. Angus P. Wilkinson
School of Chemistry and Biochemistry
Georgia Institute of Technology

Dr. Mostafa El-Sayed
School of Chemistry and Biochemistry
Georgia Institute of Technology

Dr. Faisal Alamgir
School of Materials Science and Engineering
Georgia Institute of Technology

Dr. Z. John Zhang
School of Chemistry and Biochemistry
Georgia Institute of Technology

Date Approved: August 6, 2018

To my family, friends, and myself.

ACKNOWLEDGEMENTS

There are numerous people who made my life during the past 5 years.

Long in short, I would like to thank my advisor Dr. Gleb Yushin. It's been an incredibly joyful journey working with you. I was a complete novice to energy storage field at the moment of joining the team. It was your generosity, guidance, trust and encouragement that armed me with confidence and skills to face all challenges. Thank you for sharing your knowledge, personal experiences, and drive for excellence. At such a formative age, I appreciate you as my advisor on research, moreover on being a man.

I thank my co-advisor, Dr. Seth Marder, for taking me as your student. It was your help that enabled me to pursue the path I'm passionate about. Your insistence for criticism and accuracy towards research is admirable, and it affects me. I appreciate all the conversations we had. They are concise, but crucial.

I would also like to thank my thesis committee, Dr. Faisal Alamgir, Dr. Mostafa El-Sayed, Dr. Angus P. Wilkinson and Dr. Z. John Zhang. Your suggestions perfected this dissertation. Additional thanks to Dr. John Reynolds for his efforts back in March 2013 that brought me to Georgia Tech.

I save my deepest thanks to my parents for their endless love and support for years. Without their unconditional sacrifice, I wouldn't have made it today.

I thank my beloved girlfriend Yuting for accompanying me. My days have been lightened and colored since we first met. I feel so blessed.

To my friends around the world thank you all for the time we shared, Ting Che Peng, Kaibo Hu, Weiqi Chen, Wen Jin, Mengyao Zhao, Qi Gao, Mengxi Xing, Cheng Chen, Sicheng Zhao, and others that I didn't manage to include here. The friendship with you is the treasure in my lifetime.

Thank the friends I met in the Yushin Group, Wentian, Feixiang, Danni, Hong-Ryun, Sasha, Xinran, Hailei Zhao, Chuanli Qin, Junjun Wei, Hyea, Tim, Chenchen, Xiaobo Zhang, Xiaolei, Wenbin, Qiao, Yiran, Nox, Ani, Dong-Chan, Dan Gordon, and my undergraduate assistants Xiaosi, Ruiying, Jake, Kijana and Hirsh for your time, mentorship, and help along the journey. I joined the group at a very special time point that allows me to see so many wonderful people come and go. I sincerely wish our paths will cross in the future.

TABLE OF CONTENTS

LIST OF TABLES

LIST OF FIGURES

SUMMARY

Performance and cost of battery cells are most strongly affected by their electrode and electrolyte materials, which are the basis of battery electrochemistry that enabled electrochemical energy storage applications today. This thesis systematically investigates the nanoconfinement of metal oxides and metal fluorides as electrode materials, from material selection, synthesis, characterization, to variable control, and methodology optimization.

First, nanoconfined metal oxides were developed for ultra-high-rate performance applications. Uniform lithium titanate particles within 3 nm confined within porous carbon matrix were reported for the first time and delivered up to 12 times higher gravimetric and volumetric capacities than the state-of-the-art activated carbon electrodes. This technique was used to prepare other nanoconfined metal oxides with similar dimensions, including titanium oxide, nickel oxide, manganese oxide, cuprous oxide, among others.

Conversion type cathode materials, widely regarded as the most promising candidates for next-generation lithium-ion batteries (LIBs), were studied for high energy density applications. In particular, I focused on metal fluoride (such as iron (III) fluoride, FeF_3) nanoparticles confined in carbon. Iron (III) fluoride offers very high theoretical capacity, and better safety and cost advantage over conventional intercalation-type cathode materials that require the expensive nickel and cobalt. The cyclic capacity retention of the composite produced by electrospinning followed by gas phase fluorination exceeded the state of the art by nearly an order of magnitude in cells.

Finally, the shell confinement of iron (III) fluoride cathode by *in situ* cathode electrolyte interphase (CEI) was studied. The CEI properties could be controlled by electrolyte optimization. Post-mortem analysis after cell cycling revealed insights on the mechanisms of CEI formation.

CHAPTER 1. INTRODUCTION

1.1 Overview

Today energy storage technology is blooming in response to much more rapidly growing demand. Lithium-ion batteries (LIB) have dominated the consumer electronics market and expanded aggressively to automotive industry, grid storage, and more. Tesla's giant battery plant in Australia went into operation in January 2018 and this project generated $1 million revenue in only 2 days. Most importantly, such LIB plant could be effectively incorporated into the energy mix as an essential support of intermittent renewable energy sources, solar, wind, tidal, ocean wave, geothermal, *etc*., to enable a fully renewable energy economy.

The global LIB market was valued at around $30 billion in 2016 and is expected to generate revenue of $68 billion or more by the end of 2022, growing at a compound annual growth rate exceeding 14%. The oversupply of LIBs is depressing the price and battery customers demand higher performances, triggering the investigation of the next generation energy storage solutions for lower cost and higher energy and power densities, depending on a particular application. A significant portion (sometime up to 50%) of the total cost of a battery cell is affected by electrode and electrolyte materials. Therefore, technology breakthroughs that rely on the use of cheap materials produced from broadly available resources and enabling high capacity and durability are critical.

Research on novel materials to push forward the boundaries of cost, energy/power density, cycle life and safety is becoming a priority. Many promising cathode and anode

materials appear, but most still suffer from relatively poor electrical and ionic conductivity, large volume expansion, undesirable side reactions with organic electrolytes, weak mechanical robustness, low temperature tolerance and other shortcomings. The recent two decades have been an exciting era for research and development to enhance the performances of electrode materials. Common strategies include morphology control, dimension reduction, composite formation, coating and encapsulation.[1] Nanoconfinement is the advanced technique that combines all of the above. At the time of this writing, there are still very few reports on nanoconfinement in open literature. The majority of such studies are narrowed down to the melt-infiltration of sulfur into porous carbon for improved electronic conductivity and confined sulfur particle size.[2] Sulfur is naturally a favorable material for melt-infiltration due to its relatively low melting and boiling points, and so the technique is not feasible for most other electrode materials.

1.2 Objective

The objective of this thesis is to develop a methodology to nanoconfine a broad range of metal oxides and metal fluorides and study the impact of nanoconfinement on the rate and reversibility of electrochemical reactions with liquid electrolytes.

1.3 Hypothesis

The hypotheses to test are:

1. Carbon nanopores may serve as nucleation sites for the formation of precursor particles from the solution.

2. Uniform composites may be formed by infiltration or other strategies to confine precursors into nanoporous carbons.
3. Under optimal parameters, heat-treatment may be able to convert precursor nanoparticles to active material nanoparticles without changing the morphology.
4. The process variables may have profound effects on the morphology, and electrochemical properties.
5. Upon success of nanoconfinement, one may be able to at least partially overcome some of the limitations of common electrode materials, such as poor electronic and ionic conductivities, volume changes, transition metal dissolution, phase separation, particle aggregation, among others.
6. In electrochemical cells, the properties of *in-situ* formed cathode electrolyte interphase (CEI) layer may be controlled by adjusting electrolyte salt(s) composition and affect electrochemical performance and stability of nanoconfined nanoparticles.
7. The mechanism of CEI formation may be related either to chemical decomposition and/or electrochemical decomposition of electrolyte materials and may be affected by the electrode chemistry.

1.4 Experimental Design

Experimental design selected to test the described above hypotheses included the following steps:

1. Select a range of templates and precursors of active materials.

2. Synthesize nanoconfined crystals by vacuum infiltration and/or other strategies under optimal conditions.
3. Characterize as-prepared materials by using appropriate techniques, including but not limited to: x-ray diffraction (XRD) to confirm the crystal phase, thermogravimetric analysis (TGA) to measure the mass ratio in composites, scanning electron microscopy (SEM) to image the surface morphology, transmission electron microscopy (TEM) to reveal internal features at a nanoscale, among others .
4. Study the processing-structure-property relationships by monitoring the changes of morphology, chemistry and microstructure upon changes in synthesis conditions and by analyzing how such changes affect electrochemical performance of the produced samples.
5. Upon successful synthesis of the initial material of choice, develop a methodology to apply similar or modified procedures to other electrochemically active materials.
6. Conduct post-mortem analyses, including electrochemical impedance spectroscopy (EIS), XRD, SEM, X-ray photoelectron spectroscopy (XPS) and others, to reveal how changes in the cathode microstructure, composition and surface chemistry correlate with the changes in cell performance with cycling.

CHAPTER 2. BACKGROUND

2.1 Lithium-Ion Battery – Electrode Materials and Electrolyte

"Battery" is a highly general and inclusive term in academia and should be distinguished from what industry calls the "(battery) module" and "(battery) pack". In most academic scenarios, "battery" is used by researchers to refer to "(battery) cell", which is the most basic unit of an energy storage product. Most academic studies in the battery field concentrate on cells and cell components and aim to solve fundamental problems at the cell, electrode and electrolyte levels, including this thesis. Modules and packs will not be discussed here.

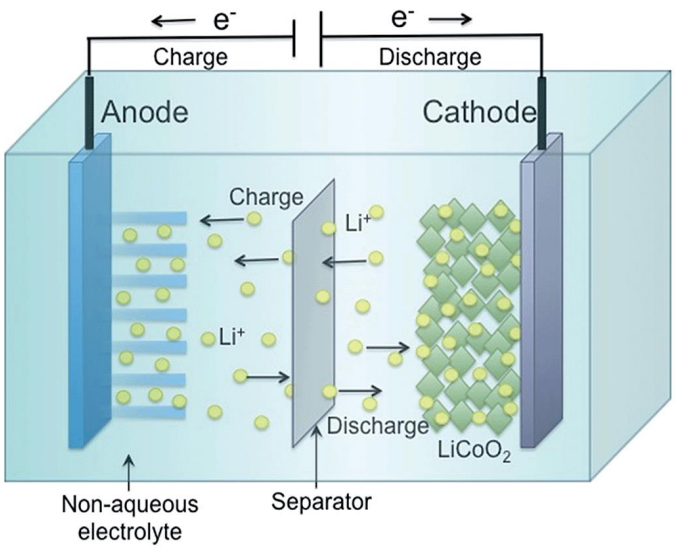

Figure 1. The standard structure layout of a typical energy storage device.[3] Reproduced with permission from The Royal Society of Chemistry.

The standard layout (Figure 1) of a traditional LIB cell includes two electrodes – cathode (higher potential electrode) and anode (lower potential electrode), separated by a

thin sheet of an electrically insulating porous separator membrane, which is soaked in an electrolyte solution that enables the free transports of solvated Li^+ ions.[3] Electrodes are comprised of metal current collector foils (Al, Cu, Ni, *etc*.) coated (mostly on both sides) by a layer of active (Li storing) materials mixed with conductive additives (usually carbon black, carbon fibers, exfoliated graphite or carbon nanotubes) and held together with polymer binder(s). For the sake of simplicity, "electrode material" only refers to "active" material and other components on the current collector (binder, carbon additives, *etc*.) would be out of the scope of this thesis. In Figure 1, the cathode material is $LiCoO_2$, and the anode material is graphite. Figure 2 represents the typical charge-discharge profiles of a typical Li-ion batteries. There're two sharp peaks appear in the CV test (Figure 2a) standing for the reversible electrochemical reaction (one for oxidation, the other reduction). The voltage of the two peaks should be consistent with the plateau voltage in Figure 2b. Flat plateaus are always observed during the charge-discharge test of Li-ion batteries.

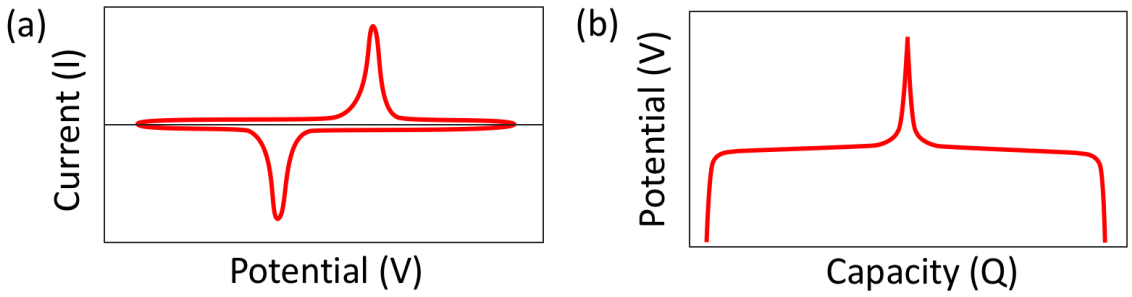

Figure 2. Typical cyclic voltammetry (a) and charge-discharge profile (b) curves of Li-ion batteries.

LIBs have already become the first choice for multiple energy storage applications, improving their "performance to cost" ratio further can greatly expand their use in the market. Dissecting a commercial LIB into its component parts and looking at the materials,

the cost of processing and cobalt in cathodes are the major hurdle of further cutting LIB cell-level cost. A great volume of research in LIBs has been in electrode materials, aiming at higher charge capacity, voltage (for cathodes), and rate capacity to enhance the energy and power densities of LIBs and make them smaller and cheaper. Because the market is already large and rapidly growing it is critical for the materials used not to be too rare.[1]

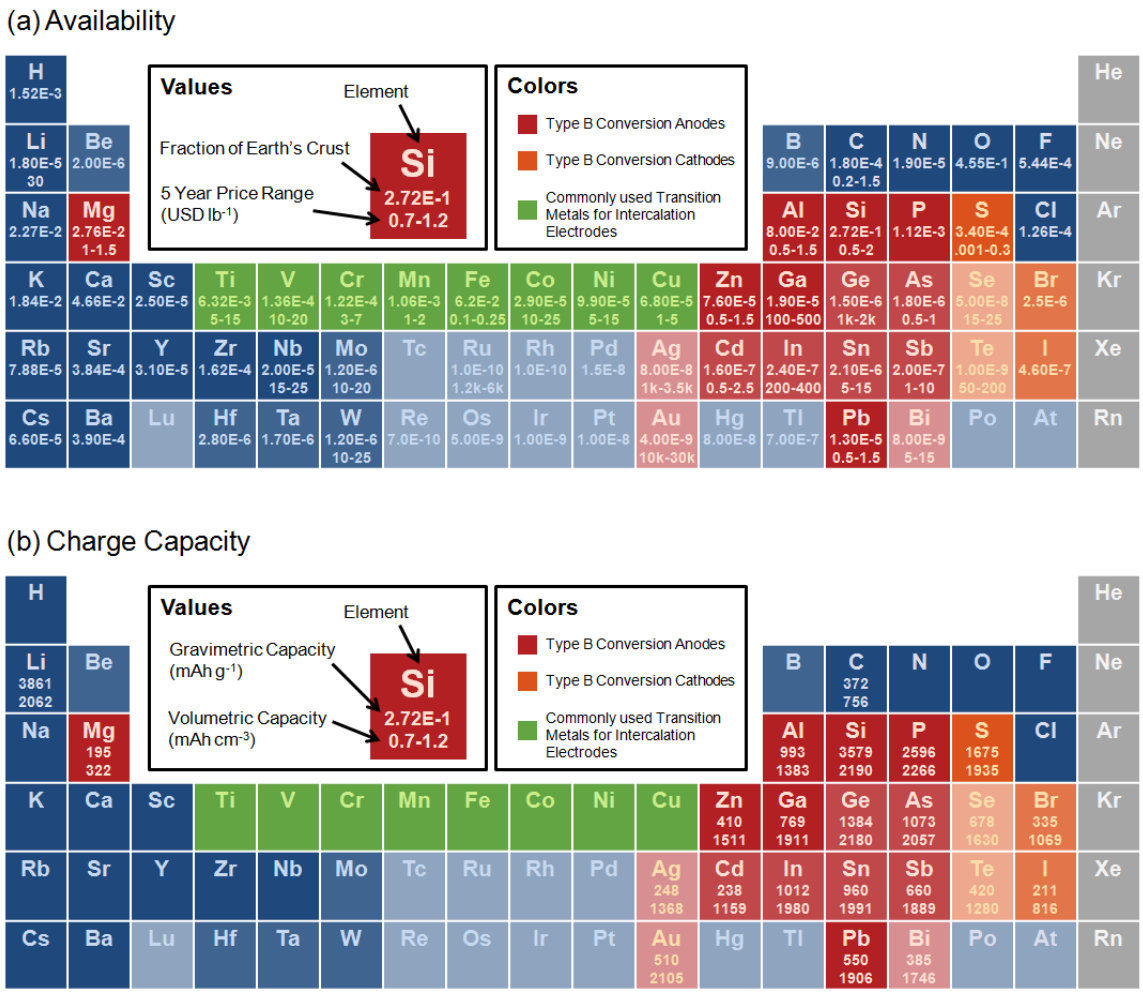

Figure 3. (a) Availability and (b) charge capacity of various alloying materials for Li-ion battery anodes. Gravimetric and volumetric capacities are theoretical values calculated based on delithiated mass and lithiated volume, respectively.[1] Reproduced with permission from Elsevier. (See Appendix A for the permission letter)

Figure 3 shows the abundance, wholesale price, and charge capacity of metals on the Earth's crust.[1] It is clearly indicated that Al, Fe, Mn, Cu, Ni, *etc*. are cheaper alternatives to Co. Accordingly, those metals are doped into conventional LCO and LMO to form new cathodes for compromised performances and cost, such as NCA, NMC, NMO, *etc*. Figure 4 is a systematic summary of the mainstream electrode materials in terms of potential vs. capacity.[1]

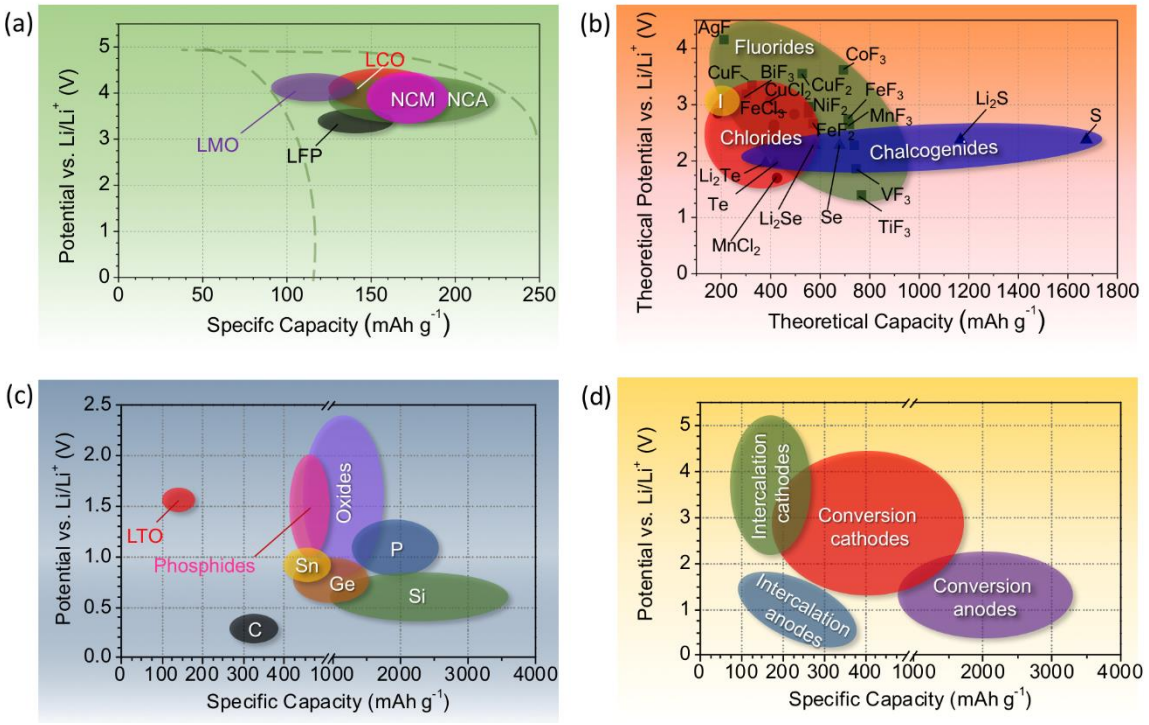

Figure 4. Approximate range of average discharge potentials vs. specific capacity of some of common (a) intercalation cathodes, (b) conversion cathodes, (c) anodes, and (d) the comparison of all three.[1] Reproduced with permission from Elsevier. (See Appendix A for the permission letter)

2.1.1 Cathode Materials

As shown in Figure 4, cathode materials can be categorized into an intercalation type and a conversion type. An intercalation cathode material has a robust crystal structure

that serves as a solid host. Li^+ intercalates into and de-intercalates from the lattice reversibly through specific diffusion channels. Most popular intercalation cathode materials both in academia and industry are transition metal oxides and polyanion compounds. Typically, intercalation cathodes have 100-200 mA h g^{-1} specific capacity and 3-5 V average voltage vs. Li/Li^+. Representative transition metal oxides include $LiCoO_2$ (LCO), $LiNi_{0.8}Co_{0.15}Al_{0.05}O_2$ (NCA), $LiMn_2O_4$ (LMO), $LiNi_{0.5}Mn_{0.5}O_2$ (NMO) and $LiNi_{0.33}Co_{0.33}Mn_{0.33}O_2$ (NCM). Some common drawbacks of these oxides are toxicity from Co, unstable crystal structure during cycling, unstable SEI, limited Li^+ diffusivity, transition metal dissolution, *etc*. Polyanion compounds describe a group of materials with $(XO_4)^{3-}$ (X = S, P, Si, As, Mo, W).[1] $LiFePO_4$ (LFP) is the representative one broadly used in automotive industry. Other examples are $LiMnPO_4$ (LMP), $LiCoPO_4$ (LCP), $LiFeSO_4F$ and $LiV(PO_4)F$. Polyanions are mostly limited by their specific capacity, and low potential. Fluorinated polyanions perform high voltage and capacity, however, the complicated mass production of high quality powders and unstable structure during cycling make them obsolete.

Conversion type cathode materials are introduced in Chapter 2.3.

2.1.2 Anode Materials

Anode materials are much less diverse than cathode materials. Most popular anode materials today are intercalation-type graphitic and hard carbons. However, intercalation-type and conversion-type metal oxides as well as alloying materials are also being explored in literature.[1]

Graphitic and hard carbons are the most broadly adopted anode materials in the battery market due to their low cost, abundance, low potential vs Li/Li^+, high conductivity and small volume change. However, their limited volumetric capacity is gradually pushing researchers to explore other anode candidates (such as Si-based) given the growing demand of high performance LIBs. Furthermore, their limited rate performance and cycle stability also pushes one to explore other anodes, including those that operate at higher potentials (vs. Li/Li^+). Among the metal oxides, intercalation-type $Li_4Ti_5O_{12}$ (LTO) has been successfully commercialized for some applications due to its superior mechanical and electrochemical stability, high rates, despite the higher cost and higher Li^+ insertion/extraction potential (note that their reduced cell-level voltage lowers cell-level energy density compared to graphite anodes). LTO is on the top list of anode materials for high power applications and dominates this market segment, in contrast to other metal oxide options, e.g. TiO_2, Mn_xO_y, Fe_xO_y, *etc*., which have not shown comparable rates, stability and overall performance and thus are not currently commercially used. Alloying materials here refer to the elements that electrochemically alloy with Li and form compound phases. This category is usually regarded as the most promising choice for next generation LIBs with higher energy density by both academia and industry. They have extremely high volumetric and gravimetric capacities, but are also notorious for their colossal volume change, expanding to several times the original volume upon lithiation. The most attractive one is Si due to its abundance, low cost, non-toxicity, chemical stability, relatively low average Li^+ insertion/extraction potential (only slightly higher than that of graphite) and the highest theoretical volumetric and gravimetric capacities, which exceed ones for graphite by nearly 3 and 10 times, respectively.

2.1.3 Electrolyte

As an electrochemical bridge ionically connecting cathode and anode, LIB electrolyte plays a key role in a battery cell in terms of electrochemical cycling stability, rate capacity, voltage window, acceptable temperature of operation, among other properties. Overall, electrolyte solution is composed of a Li salt solute, solvent mixture, and additives (minor (1-5%) co-solvents added to enhance voltage or cycle stability or to reduce flammability). Solvent mixture is used instead of a single solvent primarily due to its high solubility, tuned physical properties. Traditional LIBs typically use 0.8-1.2 M $LiPF_6$ solution in a mixture of such co-solvents as ethylene carbonate (EC), dimethyl carbonate (DMC), diethyl carbonate (DEC) and other (mostly cyclic and linear carbonate-based) co-solvents. $LiPF_6$ is the most commonly used salt due to its reasonable cost, high conductivity, stable chemical properties at room temperature, good solubility in organic solvents and passivation of Al current collectors. $LiPF_6$ becomes unstable at elevated temperatures (e.g., > 60 °C) and tends to decompose into fluorides, in which case Lithium bis(trifluoromethanesulfonyl)imide (LiTFSI) (as standalone or as a co-salt) is often considered as a substitute. However, LiTFSI causes pitting corrosion on Al current collectors at > 3.55V, thus particular solvents or passivating additives are need.[4] Other lithium salts, such as lithium perchlorate ($LiClO_4$), lithium bis(oxalate)borate (LiBoB) and lithium tetrafluoroborate ($LiBF_4$) are rarely seen in practical applications, except for particular research purposes.

Table 1 shows some of the properties for some common electrolyte co-solvents.[1] Cyclic carbonates (EC and propylene carbonate (PC) here) are particularly qualified electrolyte solvents with wide operating temperature and high dielectric constants, which

gives high polarity to promote the dissociation of electrolyte, and can form stable SEI layer on the anode. Linear carbonates (DMC, DEC, ethyl methyl carbonate (EMC)) serve as a co-solvent to tailor the viscosity, solubility, and temperature window. As the conversion electrode materials came to the stage these years, ether-based solvents, dimethoxyethane (DME) and 1,4-dioxane (DIOX), are used for the compatibility with the relatively active nature of these materials.

Table 1. Relevant physical properties of common electrolyte solvents.[5]

	Melting Point (°C)	Boling Point (°C)	Dielectric Constant (@ 25°C)	Viscosity (cP @ 25 °C)
EC	36.4	248	89.78	
PC	-48.8	242	64.92	2.53
DEC	-74.3	126	2.805	0.75
DMC[6]	4.6	91	3.107	0.585
EMC	-53	110	2.958	0.65
1,3-DIOX	-95	76	7.13	0.59
Monoglyme	-58	84	7.2	0.46
Diglyme	-64	162	7.23	
Triglyme[7]	-45	216	7.62	1.95

Electrolyte additive is an emerging field of LIB research with a principal of "moving the earth by a lever". The essence of additives is to tune the Li^+ conductivity, viscosity, dielectric constant, anode solid electrolyte interphase (SEI) and cathode solid electrolyte interphase (CEI) properties through adding trace amount(s) (typically, 0.1-5 vol.%) of salts and/or solvents. More details will be discussed in Chapter 2.4.

2.2 Lithium-Ion Capacitor – Compromise and Progress

High power electrochemical energy storage devices, such as electrochemical capacitors (also called supercapacitors) and high power Li-ion batteries, are becoming critical components of grid energy storage systems, hybrid electric vehicles, hybrid forklifts and hybrid cranes, the latest generation of energy-efficient ships, wind turbines, uninterruptable power supplies and specialized electronic devices.[1, 8-9] When compared with traditional Li-ion batteries, supercapacitors generally offer longer cycle life, broader temperature window of efficient operation and higher power, but commonly suffer from low volumetric energy density and the resulting high cost (per energy stored). The majority of commercial supercapacitors belong to the class of electrical double layer capacitors (EDLCs) comprising porous carbon (mostly - activated carbon, AC) in both positive and negative electrodes symmetrically and storing charge electrostatically (Figure 6a). In order to increase the energy density of supercapacitors, asymmetric electrochemical capacitors (often termed asymmetric capacitors) had been proposed. At least one of the AC electrodes in such devices is replaced by a pseudocapacitive or battery-type electrode.[10]

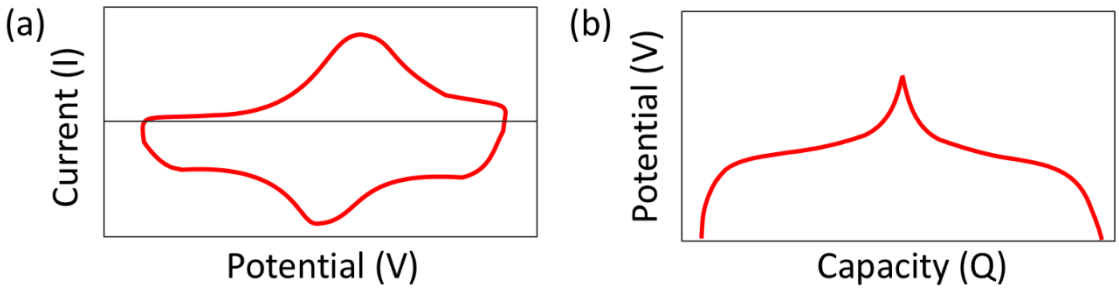

Figure 5. Typical cyclic voltammetry (a) and charge-discharge profile (b) curves of Li-ion capacitors.[11] Reproduced with permission from WILEY-VCH. (See Appendix A for the permission letter)

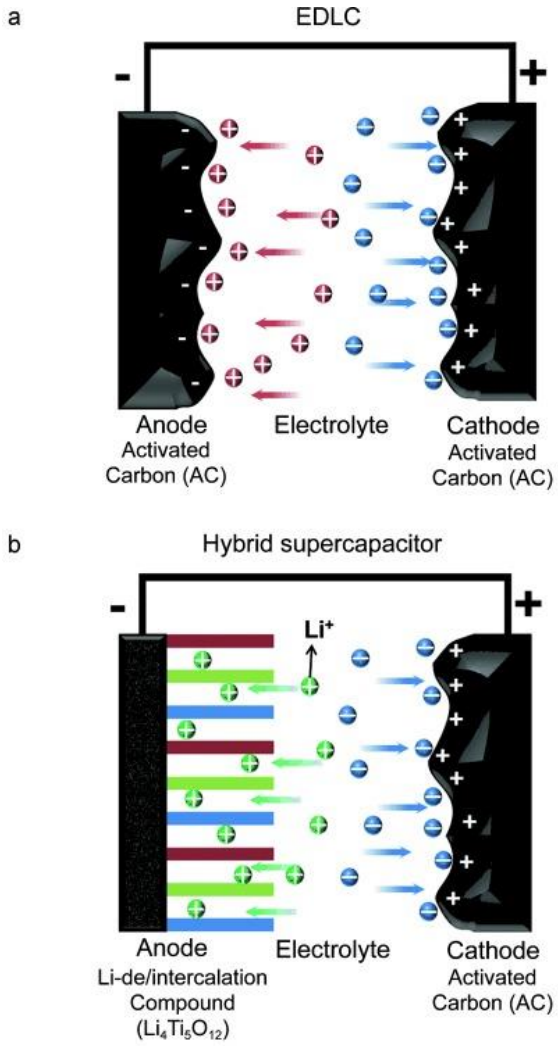

Figure 6. Schematic of the structure of a typical Li-ion capacitor, (a) EDLCs and (b) hybrid supercapacitors.[12] Reproduced with permission from WILEY-VCH. (See Appendix A for the permission letter)

Out of the family of asymmetric capacitors, Li-ion capacitors are constructed from an EDLC-type electrode and a LIB-type electrode, separated by a Li salt based electrolyte (Figure 6b).[12] Different from Li-ion batteries (Figure 2), the charge-discharge profiles of Li-ion capacitors are more like those with round corners (Figure 5).[11] Commonly, the electrochemistry associated with such device are represented by ion adsorption/desorption at the cathode surface and Li^+ intercalation/de-intercalation at the anode surface

simultaneously. That being said, the coupling of Faradaic and non-Faradaic reactions provides a solution to compromise and improve both the energy and power density simultaneously (Figure 7).[11]

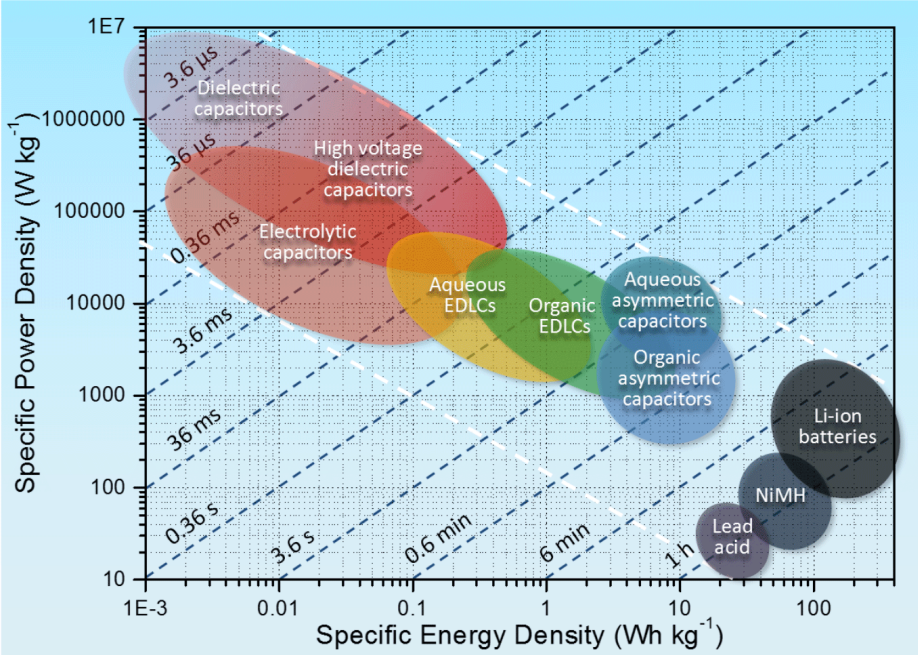

Figure 7. Approximate range of specific power density vs. energy density of common energy storage devices.[11] Reproduced with permission from WILEY-VCH. (See Appendix A for the permission letter)

2.2.1 Electrolytes

Electrolytes of Li-ion capacitors can be either aqueous or organic. Aqueous solutions preform low viscosity thus high mobility, despite the limited voltage range and voltage window. In contrast, organic electrolytes are able to afford high voltage up to 3 V but with high viscosity thus low ionic conductivity.

Popular aqueous electrolytes include basic solutions (e.g., LiOH), acidic solutions (e.g., H_2SO_4 and Li_2SO_4), and neutral solutions (e.g., $LiNO_3$) with concentration of 0.1-6

M. Aqueous electrolytes is an independent and inclusive research area with rich history. Solute selection (cations and anions), concentration and additives all play a key role in the performance, but further discussion will be out of the scope of this thesis. Most commercial Li-ion capacitors comprise organic electrolytes. Their electrolyte selection usually overlaps with that of the relevant LIB electrolytes with appropriate optimization for lower viscosity and higher ionic conductivity, for example, replacement of EMC by acetonitrile, lowering the concentration, *etc*.

2.2.2 Electrode Materials

Commonly used electrode materials in Li-ion capacitors are carbonaceous materials (high surface area activated carbon used by industry, carbon nanotube, graphene, and other novel materials used in academic studies), metal oxides and hydroxides, various Li^+ intercalation compounds and their composites. The proper balance of the absolute value of power and energy of the two electrodes is critical in the net operating potential and long-term performance retention.

In aqueous Li-ion capacitor systems, metal oxides, such as NiO, MnO_2, V_xO_y, and Fe_xO_y, have been used as cathode materials, while AC serve as anode materials in a balanced cell. Manganese oxides are usually considered as promising materials due to low cost and low toxicity. But similar to Mn-based battery materials, degradation from Mn dissolution remains to be a challenge.

Non-aqueous systems usually adopt AC, metal oxides, hydroxides and polyanions as cathode materials, such as $LiMn_2O_4$ and $LiCoPO_4F$, while $Li_4Ti_5O_{12}$ and TiO_2, as anode materials. Overall, the kinetics of Li^+ intercalation in those materials are much lower

compared with EDLCs. Researchers are interested in controlling the particle size and morphology, or introducing highly conductive additives to overcome this issue.

2.3 Conversion-Type Cathode Materials

Electrochemical energy storage devices have been developing for more than a century, and are now broadly applied in our daily life. As evolution of technology is rapidly being pushed forward, there is a consistently growing demand for next-generation energy storage devices that is cheaper, lighter, smaller and safer. Unfortunately, LIBs utilizing conventional intercalation-type electrodes approach to their theoretical limits and further improvements in their energy storage characteristics are limited.[1, 13] With a relatively successful progress of advanced anode materials,[10] conventional cathode materials based on intercalation chemistries, such as LCO, NCA, NMC, are becoming an energy-limiting factor typically only able to store less than one Li^+ in each compound (Figure 8a).[14] In addition, the transition metal contents in such materials (particularly cobalt (Co) and to a less extent nickel (Ni)) are expensive, limited in world reserves, heavy and toxic. Therefore, it is critical to explore other chemistries and achieve sufficient performance breakthroughs to meet the strong need for improved cathodes produced from cheap and abundant transition metals.

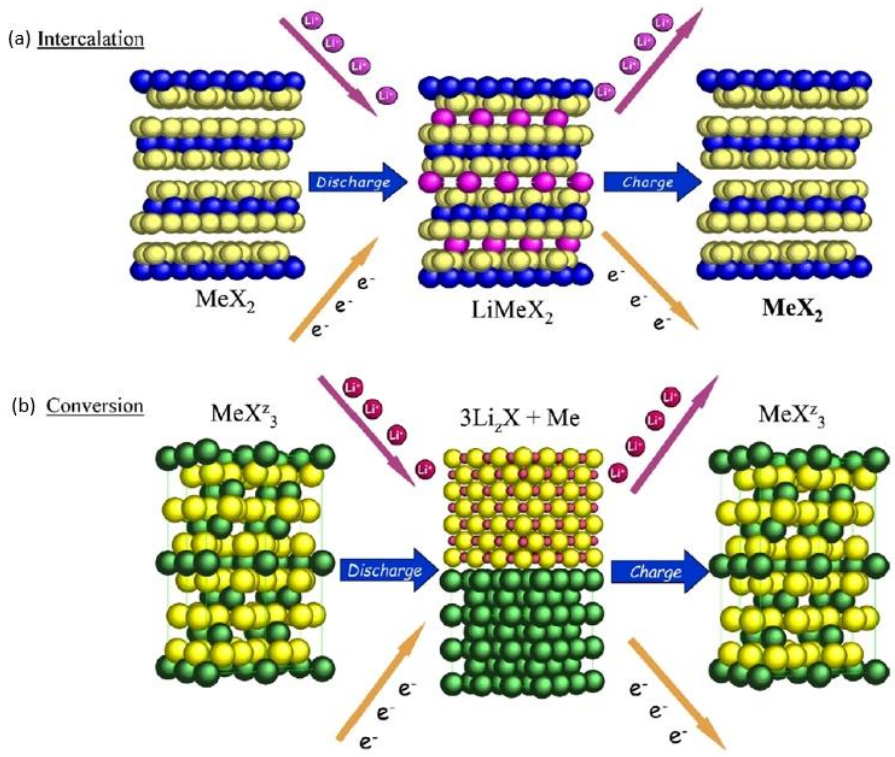

Figure 8. Mechanism comparison of (a) intercalation-type and (b) conversion-type electrode materials during charge (delithiation) and discharge (lithiation).[14] Reproduced with permission from Elsevier. (See Appendix A for the permission letter)

Relatively new LIB cathode materials, such as metal chalcogenides and metal halides, based on conversion chemistries are now attracting renewed interest (Figure 4d). They overcome the limits of intercalation materials by accommodating multiple Li^+ per compound as shown in Equation 1, yielding lithium or transition metals (M) and Li_nX phases (X = S, F, Cl, *etc*.) during discharge and re-generating M_aX_b upon charge:

$$M_aX_b + nbLi^+ + ne^- \leftrightarrow bLi_nX + aM \quad (1)$$

Such materials are called conversion cathode materials and there's a major change in their crystalline structure involved during lithiation/delithiation, which breaks and reforms chemical bonds repeatedly (Figure 8b).

2.3.1 Metal Fluorides and Metal Chlorides

Metal fluorides and chlorides have been attracting increasing attention in the academia recently as promising cathode candidates due to their high theoretical energy density, resulting from the intermediately high voltages and specific capacities (Figure 4b). Metal fluorides and chlorides generally suffer from poor conductivity, large charge-discharge hysteresis, severe volume expansion, undesirable side reactions and metal dissolution. These materials are notorious for poor electronic conductivity resulting from the large band gap induced.[1]

It has been found that some of such conversion reaction could badly pulverize the initial morphology of metal fluorides and chlorides into metal nanoparticles, which catalyze the decomposition of cyclic carbonates. In addition, Fe, Cu, *etc*. nanoparticles could be oxidized to related cations and dissolve in the electrolyte readily, which is very challenging to conquer. Some metal fluorides and chlorides are even susceptible to dissolution in common electrolyte solvents, making it unrealistic to be considered for practical application unless a new type of cell design is introduced, such as solid-state battery. The volume expansion, however, is modest compared with chalcogenides.

The state-of-the-art strategy to overcome these drawbacks is constructing protective shells either from materials design or tailing CEI. Combination with conductive additives seems to be an effective way to improve the conductivity. Overall, the high

oxidation state of the transition metals and thus active chemical properties complicates the research study of metal fluorides and chlorides by magnitudes.

2.3.2 Sulfur and Selenium

The past seven years are big years of sulfur. It has never been this hot in the energy storage material history. Sulfur, one of the most abundant elements in the Earth's crust, was found to have potential application as a cathode material for lithium batteries, with remarkably high theoretical capacity of 1675 mA h/g (Figure 4b). In spite of high capacity, S performs low potential vs. Li/Li^+, which drags its energy density down. It also suffers from serious dissolution of intermediates formed during charge-discharge (polysulfides), and low vaporization temperature, which induces loss of S under vacuum. S also expands by 80% after fully lithiation, which destroys the electrical contact in standard electrodes. Substantial efforts have been put to solve these problems, including nanostructure design, S encapsulation, replacement by Li_2S, electrolyte optimization, *etc*. However, more cost-efficient approaches still need to be developed. Selenium, benefiting from the development of sulfur, also attracted attention recently. Similar to S, Se has high specific capacity but with higher conductivity, and also suffers from dissolution issue and dramatic volume change. The main limitation of Se comes from its lower abundance, comparable to Ag and Au, and relatively high price, making it almost impossible to be used in high volume applications.

2.4 Electrolyte and Solid-Electrolyte Interphase (SEI and CEI)

Solid-electrolyte interphase, SEI, is a layer that forms at the interface between electrode and electrolyte with 10^0-10^2 nm thickness.[15-16] The growth of SEI primarily is a

result of electrochemically and/or chemical decomposition reaction between active materials and the electrolyte solution. The exact mechanisms are very complicated and sometimes mysterious, however, SEI is critical to the stability and failure of LIBs. For example, capacity loss in a full cell is usually because of loss of active materials or total lithium inventory, while active materials can be consumed for the growth of SEI locally. Such effect can be exacerbated at elevated temperatures, as this process is diffusion driven.

SEI objectively forms on both cathode and anode, though more apparently on the anode side. Cathode SEI is often referred to as "CEI". The composition of SEI and CEI is highly dependent on the electrode materials, electrolyte, voltage window, temperature, cell aging, purity of cell components, *etc*. For $LiPF_6$ based cells, the anode SEI usually contains Li_2CO_3, organic semi-carbonates, LiF, P_xF_y and $P_xO_yF_z$.[17-19] Electrolyte additives could tune the composition of SEI effectively, but it's often case by case and very difficult to control.

FEC and VC are two common solvent additives for anode SEI formation. Please be mindful that solvent additives also change the viscosity and dielectric constant of electrolyte, making the justification more arbitrary. Solute additives are lithium salts that contain B, N, P, S, F, Cl, Br, I, *etc*. for special purposes.[20]

Native oxides can affect SEI properties. A good example is that Si anodes fabricated in air will inevitably be covered by a native oxide layer. This layer will be irreversibly transformed into Li-Si-O compound at first charge (lithiation), which might be applicable to other conversion anodes.[18]

CHAPTER 3. LITHIUM TITANATE NANOCONFINED IN POROUS CARBON FOR LITHIUM ION CAPACITORS

Porous carbons suffer from low specific capacitance, while intercalation-type active materials suffer from limited rate when used in asymmetric supercapacitors. This chapter demonstrates that nanoconfinement of intercalation-type lithium titanate ($Li_4Ti_5O_{12}$) nanoparticles in carbon nanopores yielded nanocomposite materials that offer both high ion storage density and rapid ion transport through open and interconnected pore channels. The use of titanate increased both the gravimetric and volumetric capacity of porous carbons by more than an order of magnitude. High electrical conductivity of carbon and the small size of titanate crystals allowed the composite electrodes to achieve characteristic charge and discharge times comparable to that of the electric double-layer capacitors. The proposed composite synthesis methodology is simple, scalable, and applicable for a broad range of active intercalation materials, while the produced composite powders are compatible with commercial electrode fabrication processes.[10]

3.1 Introduction

As one of the anode materials for high-rate LIBs, spinel $Li_4Ti_5O_{12}$ (LTO), has attracted significant attention due to its "near-zero" volume change during repeatable lithiation and delithiation, which contributes to its excellent cyclic stability.[21-23] One drawback of LTO to be qualified for high-rate performance is its poor electrical conductivity (10^{-13} to 10^{-9} S cm^{-1}).[24-26] The commonly explored routes for improving LTO electrical conductivity involved doping of metal or nonmetal ions (Mg^{2+}, Al^{3+}, Zn^{2+}, Zr^{4+}, W^{6+}, F^-, Br^-, *etc.*) into Li, Ti or O sites of LTO. Unfortunately, the cyclic stability of such doped LTO was often found to be impaired and the resulting rate performance was not as high as desired.[27-28] Conductive carbon coating on the LTO surface may increase its electrical conductivity, but, unfortunately, at the expense of significantly higher ionic resistance, which becomes a rate-limiting step in electrochemical reactions. The Li^+ transport in the bulk of LTO is also substantially slower than that in liquid electrolytes, which makes LTO electrodes sluggish compared to typical supercapacitor electrodes.[29] To address the slow ion transport, high surface area LTO morphologies, such as hollow nanostructures,[30] composite nanoparticles,[31-32] nanosheets and nanowires,[33-35] and others,[22, 25-26, 31, 36] have been explored. In spite of the promising results and significant progress in this field, the overall rate performance characteristics of nanostructured LTO are still 1–2 orders of magnitude slower than that in EDLCs. Further reduction in characteristic dimensions of LTO and thus Li^+ diffusion distance has been a challenge because the high annealing temperatures required during synthesis (700–800 ^oC) induce growth of LTO crystals due to Ostwald ripening. In addition, many of the recently explored nanostructures still suffer from low electrical conductivity, are difficult to handle and

utilize in commercial electrode fabrication processes and may additionally induce health hazards (particularly nanowires and nanoparticles).

Similar to LTO, most of the other battery and pseudocapacitive materials suffer from relatively low electrical conductivity. Several methods (in addition to physical mixing) to deposit ion-storing metal oxides and conductive polymers on the surface of electrically conductive carbon have been explored to improve the capacity retention and to reduce cell resistance of asymmetric capacitors.[37-43] The majority of studies utilized graphene and carbon nanotubes (CNTs), which have large pores between the particles that are available for oxide or hydroxide depositions, but are often too costly and often too difficult to use in commercial electrode fabrication equipment. In addition, uniformity of such deposition is mostly limited. Some of the techniques that have been explored, such as atomic layer deposition (ALD) processes, offer well-controlled and extremely uniform deposition of smooth metal oxide-based coatings on electrically conductive porous materials,[44-45] which maximizes utilization of the active material in asymmetric capacitors (and high power batteries) at high charge and discharge rates. However, ALD currently remains prohibitively expensive.[46]

This chapter reports on a novel facile strategy for the synthesis of uniform and spherical $Li_4Ti_5O_{12}$ activated carbon nanocomposites (LTO-ACs), where crystalline sub-4 nm LTO nanoparticles are uniformly distributed and confined in the nanopores of the carbon matrix but do not block these open and interconnected carbon pores. Carbon pore walls not only serve as spatial confinements to control the growth of LTO nanocrystals but also provide effective pathways to supply electrons directly to individual LTO nanoparticles. The interconnected open pores remaining in the LTO-AC composites allow

for the rapid transport of Li^+ ions. As a result, the best LTO-AC samples comprising a small volume of mesopores demonstrated remarkable performance characteristics, showing more than 100 mA h g^{-1} at the ultrahigh rate of 350C (> 60 A g^{-1}, 1C = 175 mA g^{-1}), where charge or discharge takes place in ~ 6 s. At this rate, the LTO-AC shows 12 times higher gravimetric capacity and 12 times higher volumetric capacity than pure AC. When compared with recently published LTO-based and other material-based supercapacitors, the reported LTO-AC composites show significantly higher specific capacity at higher current rates. In contrast to the previously reported nanosized particles of various shapes and sizes, which are difficult to handle and utilize in electrodes, micron-scale LTO-AC powders have the potential to serve as a drop-in replacement for AC powders in electrode production.

3.2 Experimental Methods

Activated carbon was provided by collaborator Sila Nanotechnologies, Inc. Sol-gel method was firstly used to synthesize nanosized LTO but only yield LTO particles sizing 5 nm or larger. Given the most pore size of active carbon within 3 nm, the sol-gel path was discontinued. Nanosized TiO_2 particles within 5 nm were also successfully synthesized, however, they tend to agglomerate severely at crystallization temperature (> 600 ^oC), making it unfeasible to be infiltrated in the carbon pores.

3.2.1 Synthesis of LTO-ACs

LTO-ACs were then prepared by a vacuum impregnation technique. In a typical synthesis, 340 mg of titanium(IV) butoxide (reagent grade, 97%, Sigma-Aldrich, USA) and 57 mg of lithium acetate (99.95%, Sigma-Aldrich, USA) were dissolved in 2 mL of

methanol (anhydrous, 99.8%, Sigma-Aldrich, USA) by ultrasonication for 5 min to obtain a transparent solution with a bright yellow color as the precursor. In an argon-filled glovebox, the precursor solution was then added dropwise to 200 mg spherical nanoporous activated carbon. Vacuum was applied during the interval of every second addition. The precursor–AC composites were then preheated in air at 300 ^{o}C for 1 h, followed by calcination at 800 ^{o}C in argon atmosphere for 10 h, yielding LTO-ACs. All three LTO-ACs were produced identically, using the same amount of starting materials and contained identical LTO to AC ratio in mass.

3.2.2 Material Characterization

XRD patterns were collected on a X'Pert PRO Alpha-1 (PANalytical, The Netherlands) with Cu Kα radiation at a voltage of 40 kV and a current of 20 mA. SEM images and EDS elemental mapping were acquired on Hitachi SU8010 (Japan). HR-TEM and STEM images with EDS line scans were performed on a Tecnai F30 (FEI, The Netherlands). The BET surface area and pore size distribution by the DFT method were analyzed on a Tristar porosimeter (Micromeritics, USA). Thermogravimetric analysis was performed on a Pyris 1 TGA.

3.2.3 Electrochemical Measurements

Electrochemical characterization was carried out using type 2032 coin cells at room temperature. The thin-film cathode consisted of commercial active carbon (YP-17D) and polytetrafluoroethylene (60% dispersion in H_2O, Sigma-Aldrich,USA) in a weight ratio of 90:10, while the anode consisted of active material (LTO-ACs), carbon black (added for comparison with prior studies on LTO), and poly(acrylic acid) (MW ~450000,

Polysciences, Inc., USA) in a weight ratio of 70:15:15, casted on Cu foil. The electrodes were dried in vacuum at 70 ^{o}C for 12 h. The electrolyte was composed of 1.0 M $LiPF_6$ in acetonitrile. Coin cells were assembled identically in an argon-filled glovebox. The cyclic voltammetry studies and galvanostatic charge–discharge tests were performed using a Solartron 1480 Multistat (USA) and an Arbin BT-2043 (Arbin Instruments, USA), respectively. Volumetric capacities were calculated at the active material (individual particle) level by considering total porosity of the composite powders, mass fractions of C, and LTO as well as their densities.

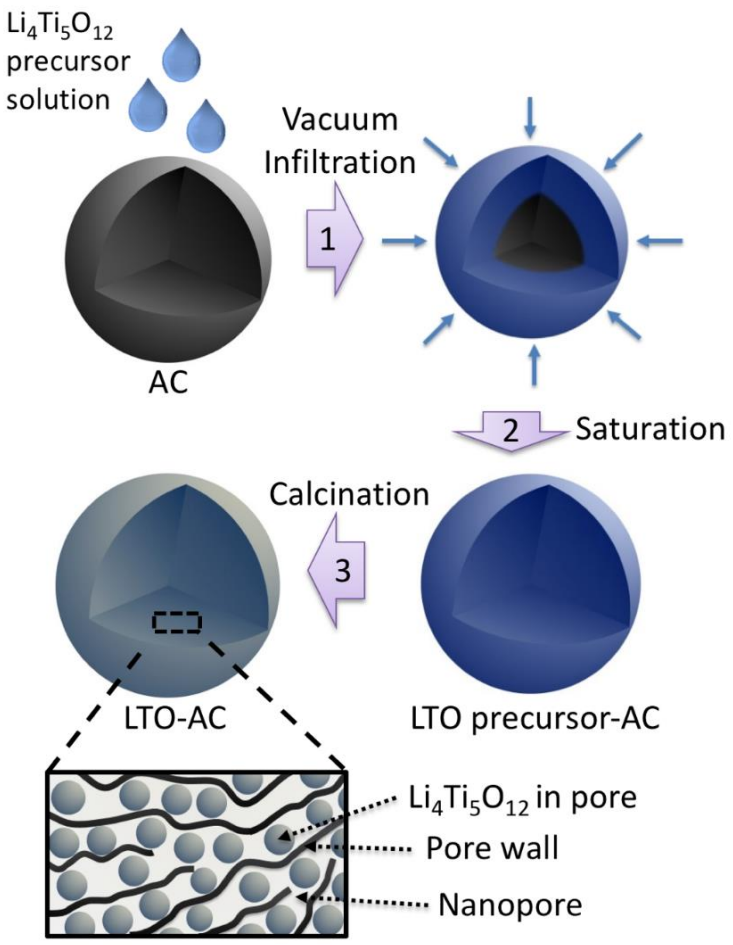

Figure 9. Schematic illustration of the synthesis of LTO-ACs: (1) vacuum infiltration of the precursor solution into AC; (2) saturation of the precursor solution; (3) calcination and crystallization.

3.3 Results and Discussion

The proposed synthesis protocol for LTO-ACs is schematically illustrated in Figure 9. The synthesis of hydrophilic spherical AC particles was previously described by our group.[47] Three types of porous AC (AC #1, #2, and #3) with different pore size distribution were used in this work in order to reveal the impact of pore size distribution and particle size on the electrochemical characteristics of thus-produced electrode materials. As a first step, a clear concentrated solution of a Ti source (this work used titanium (IV) butoxide)

and a Li source (this work used lithium acetate) in methanol was prepared and then slowly dropped into AC powders, followed by periodic vacuum-drying steps to evaporate methanol and confine the precursor mixture within the AC pores. The low surface tension of methanol in combination with strong capillary forces facilitated the successful impregnation of LTO precursors inside the AC pores, rather than deposition on the external surface of AC particles. In order to achieve higher loadings of LTO, these steps can be repeated several times. After infiltration of the sufficient content of the LTO precursor, the composites were preheated in air at ~300 °C to decompose titanium (IV) butoxide and lithium acetate into TiO_2 and Li_2O, respectively. The temperature should be sufficiently low to prevent the oxidation of AC pore walls. The final synthesis step involved calcination (annealing) in an inert gas (argon) to obtain the LTO-ACs (LTO-AC #1, #2 and #3 respectively). The amount of the starting materials, Ti/Li sources and ACs, was controlled to be identical during the preparation, leading to the same mass ratios of LTO to AC in all three samples and eliminating the impact of chemical composition on the electrochemical properties. It should also be clarified that the proposed process is general and the same procedures could be utilized for a broad range of other porous carbon materials, such as carbide-derived carbons, ordered mesoporous carbons, and zeolite-templated carbons, to mention a few.[47-49]

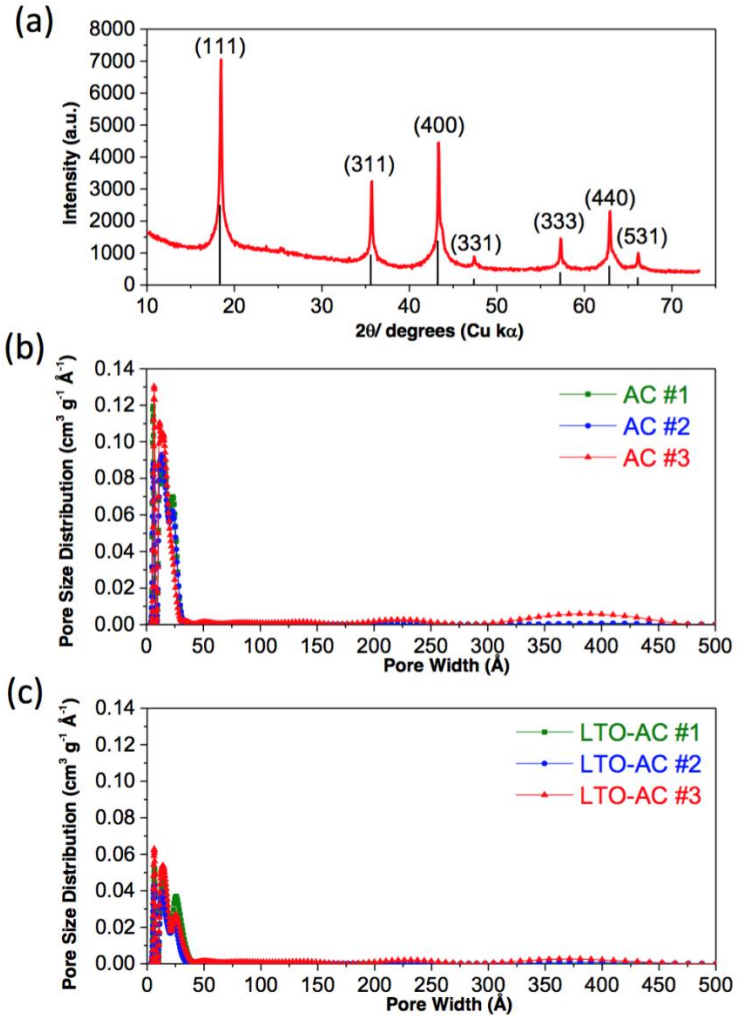

Figure 10. (a) XRD patterns of LTO-AC (LTO-AC #3 here, as an example); pore size distribution of different AC spheres without (b) and with (c) LTO loading.

Figure 10 shows results of the selective characterization techniques. Figure 10a shows the X-ray diffraction (XRD) pattern of LTO-ACs. All of the Bragg peaks can be ascribed to the spinel LTO phase (JCPDS card no. 49-0207, space group: *Fd* 3*m*) without any significant content of residues or parasitic phases detected.[33] An interesting observation herein is the inconsistency of the anticipated LTO size (< 3 nm) with full width at half maximum of XRD peaks. This may due to the signal overlapping of the particles in micropores and those in mesopores, resulting in peaks with broad bottoms but sharp tops.

Thermogravimetric analysis (TGA) conducted in air could be utilized for determination of the carbon and LTO content in the LTO-ACs. A noticeable weight loss observed at 400–500 ^{o}C corresponds to the oxidation of carbon in LTO-ACs (to CO and CO_2 gases), revealing the LTO weight fraction (52 wt % in this case; see Figure 11). Nitrogen sorption measurements of AC powders before and after impregnation with LTO nanoparticles reveal a decrease of Brunauer-Emmett-Teller (BET) surface area from 3100- 3500 m^2 g^{-1} to 1300-1700 m^2 g^{-1}. This decrease is expected due to the increase in the mass of the samples. Despite this, the remaining volume of still open and interconnected pores might be sufficiently large to promote rapid electrolyte penetration to support electrochemical reactions at high rates (*vide infra*). The pore size distribution curves calculated by nonlocal density functional theory (NLDFT) of the empty AC spheres (AC #1, #2 and #3) and LTO-ACs (LTO-AC #1, #2 and #3) are plotted in Figure 10b and Figure 10c, respectively. More detailed information is present in Figure 13a (0- 50 Å) and 10c (50- 100 Å). All the AC and LTO-ACs have a majority of pores within 4 nm. However, AC #3 and LTO-AC #3 also contain a small amount of mesopores (30- 50 nm). The pores in the range of 1-4 nm facilitate electron tunneling from the conductive AC pore walls to LTO reaction sites since the average distance between conductive carbon and LTO is less than 1-2 nm, while the larger pores (up to ~ 50 nm, particularly well-developed in AC #3, Figure 13c) may provide pathways for faster Li^+ ion transport from the surface to the bulk of the composite.

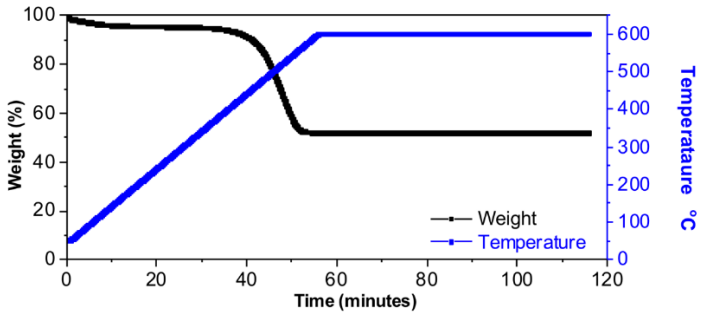

Figure 11. TGA curve of LTO-ACs at 10 ºC min^{-1} in air.

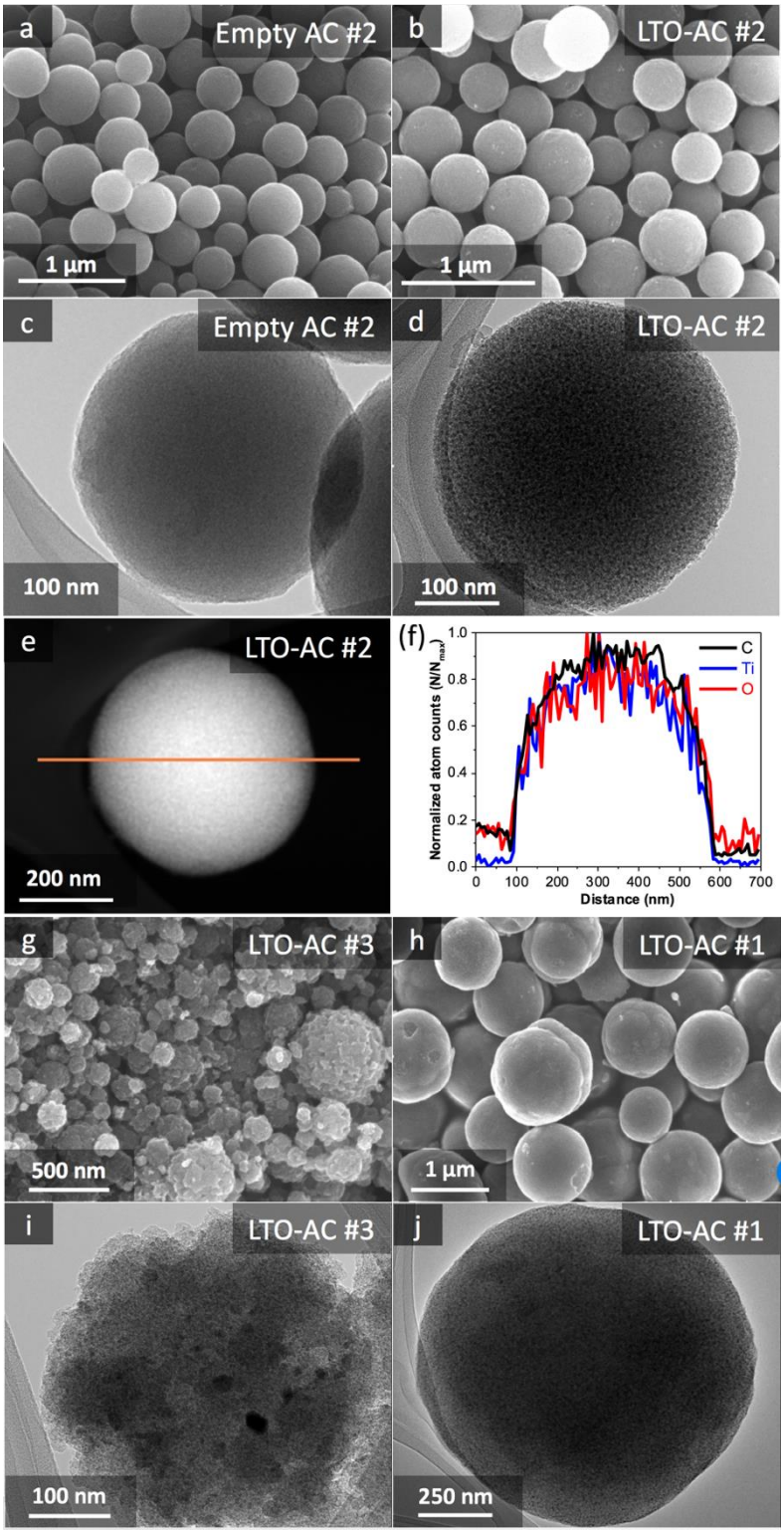

Figure 12. SEM and TEM images of as-synthesized empty AC and LTO-ACs: (a, c) empty AC #2; (b, d) LTO-AC #2; (g, i) LTO-AC #3; (h, j) LTO-AC #1; STEM image

(e) and EDS line scan results (f) of LTO-AC #2 nanocomposites, showing uniform distribution of LTO within a sphere.

The morphologies and microstructures of the empty AC templates and the produced LTO-ACs have been examined by scanning electron microscopy (SEM) and high-resolution transmission electron microscopy (HR-TEM) studies. Figure 12a shows empty AC #2 particles, which exhibit nearly perfect spherical shape and high uniformity with an average diameter of ~400 nm. After LTO loading, the morphology of LTO-AC #2 stays consistent with empty AC #2 and no distinct LTO nanoparticles could be seen on the outer surface of the spheres (Figure 12b). Figure 12c and Figure 12d compare the transmission electron microscopy (TEM) micrographs of an empty AC #2 sphere and a LTO-AC #2 particle, where the LTO nanoparticles are dispersed uniformly in AC #2 (Figure 12c). As seen in Figure 12d, the LTO particle size ranges from 2 to 4 nm, which is consistent with the AC #2 pore size distribution (Figure 10b and Figure 13a). Since LTO nanoparticles are formed in the AC pores their dimensions are restricted by the pore size. The scanning transmission electron microscope (STEM) micrograph (Figure 12e) represents the so-called Z-contrast imaging, where Z refers to the atomic number (the number of electrons per atom). In a Z-contrast image, the signal is proportional to the number of electrons per unit of illuminated area of a sample, which is strongly influenced by Ti (Z = 22) and O (Z = 8) atoms and thus LTO uniformity could be directly visualized (in this case – as a nearly perfect projection of a uniformly-dense spherical particle). EDS line-scan analysis (Figure 12f) confirms such observations and demonstrates that both Ti and O are uniformly distributed within the AC #2 spheres. LTO-AC #1, #2 and #3 samples were prepared using an identical process. The SEM and HR-TEM images of LTO-AC #3 and LTO-AC #1 are

shown in Figure 12g, i and Figure 12h, j, respectively. All three samples impregnate LTO uniformly and no LTO particles are observed outside the AC.

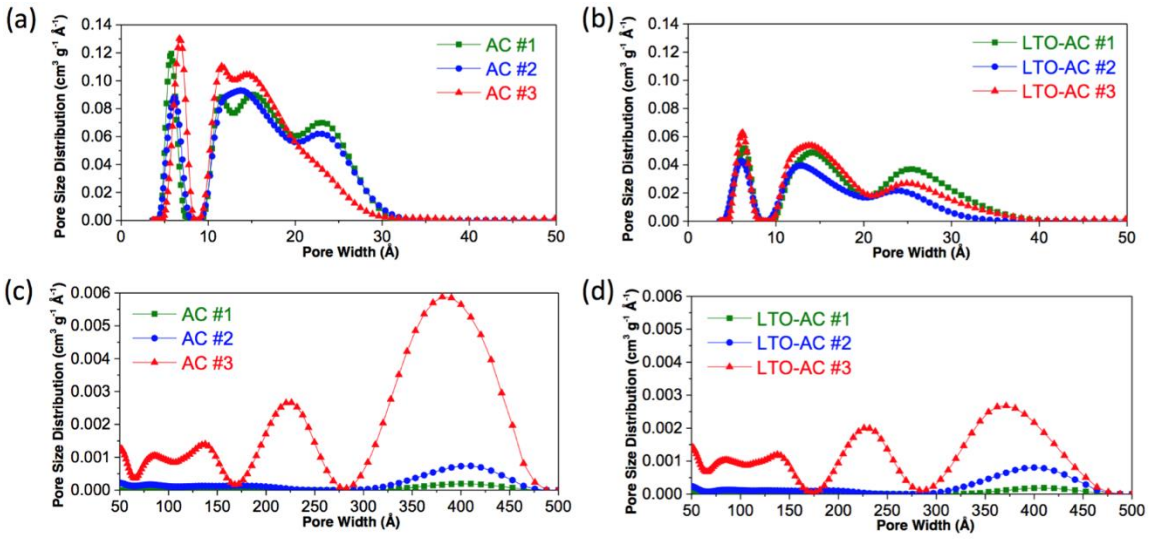

Figure 13. Pore size distribution of AC spheres: without (a) and with (b) $Li_4Ti_5O_{12}$ loading (within 50 Å); without (c) and with (d) $Li_4Ti_5O_{12}$ loading (50- 500 Å).

I'd like to emphasize the great flexibility that this approach offers for the design of such composite particles because their particle size distribution as well as LTO particle size and pore size distribution of the LTO-ACs could be easily tuned by adjusting size and porosity of the AC powders (or other types of porous carbon powders) used for the vacuum impregnation process.[50-52] Thus, the electrochemical, physical and even mechanical properties of the composites are adjustable. This work will demonstrate that relatively small variations in the porosity and morphology of the LTO-ACs dramatically impact their electrochemical performance characteristics.

Many previously reported studies utilized so-called half-cell configurations for electrochemical characterizations, where lithium (Li) foil was used as a counter electrode (an anode).[26, 30, 33] While such cells are certainly easy to make, the results (both the reaction

rate and cell stability) might be significantly different than that of the real cells. This is because the Li losses in this system are hidden by the huge excess of Li present in half-cells because a majority of the side reactions take place on the Li anode (due to it lower potential) and because possibly harmful oxidation reactions are eliminated by the lack of the high-voltage cathodes in such cells. In addition, the rate of lithium ionization and deposition that occurred at the Li foil (Equation 2) may be either slower or faster than the Li insertion and extraction rate into the cathode. In the case where Li plating/ionization (Equation 2) is slower than Li insertion/extraction into/from LTO (Equation 3), the rate performance of half-cells will no longer accurately reflect the rate capability of LTO.

$$Li^+ + e^- \rightleftarrows Li(s) \tag{2}$$

$$Li_4Ti_5O_{12}(s) + 3Li^+ + 3e^- \rightleftarrows Li_7Ti_5O_{12}(s) \tag{3}$$

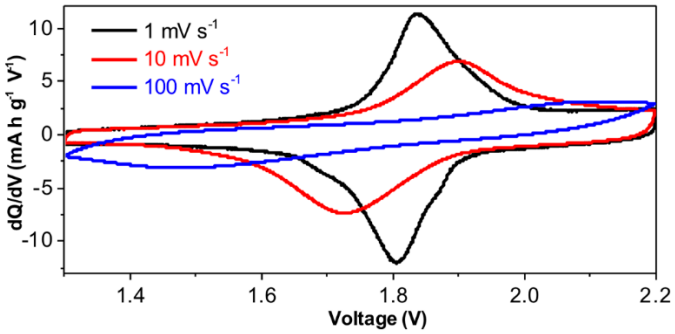

Figure 14. Cyclic voltammetry curves of AC//LTO-ACs full cells.

Therefore, electrochemical tests of the produced LTO-AC anodes against a commercial activated carbon (AC) double-layer cathode were carried out, and asymmetric capacitor full cells were built. The cathode areal capacity exceeded that of the anode by at

least 10% to make sure the overall performance is anode-limited. By examining cyclic voltammetry (CV) of such cells (Figure 14) and revealing the potentials of the corresponding oxidation and reduction reactions, the full cell range of 1.3-2.2 V was selected for this study. At the scan rate of 1 mV s^{-1}, two strong peaks at ~1.82 V are observed when Li^+ ions are both intercalated or extracted from LTO (Equation 3) and additionally adsorbed/desorbed onto/from the AC surface of the LTO-ACs, while the counterions are adsorbed/desorbed onto/from the surface of the commercial AC cathode. No side-reaction peaks could be seen.

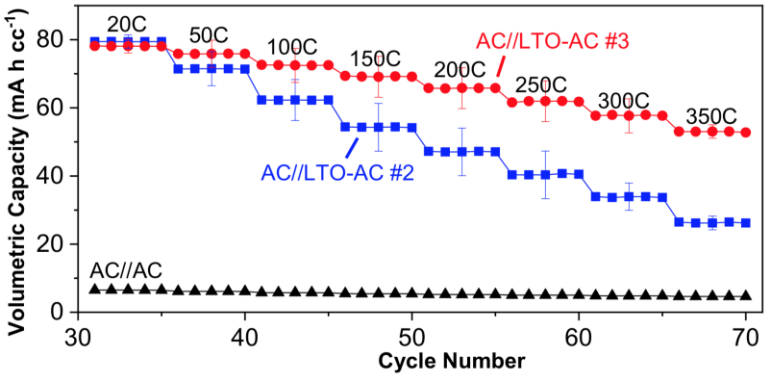

Figure 15. Specific volumetric performance Specific volumetric performances of different AC//LTO-AC full cells in comparison with AC//AC full cell. AC//LTO-ACs are cycled between 1.3-2.2 V while AC//AC is 0.5-2.7 V.

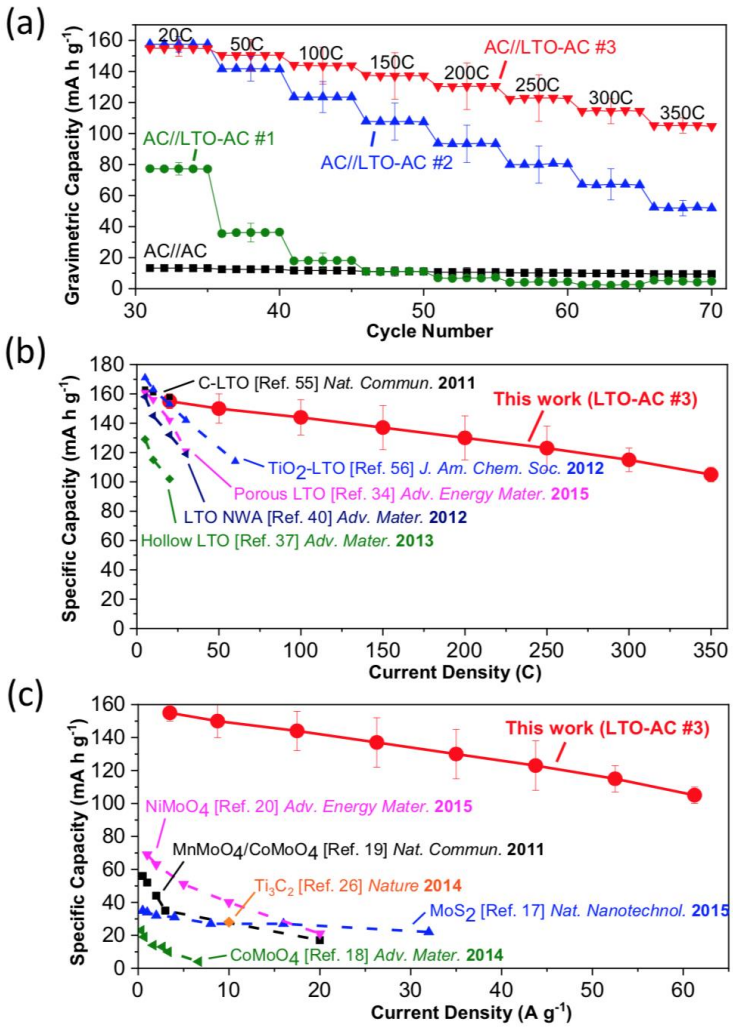

Figure 16. Specific gravimetric performances of different AC//LTO-AC full cells in comparison with the AC//AC full cell (a); AC//LTO-AC #3 in comparison with recently reported LTO-based half cells (b) and other supercapacitor electrode materials (c).

In EDLC and supercapacitor research it is conventional to express ion storage abilities of the materials in the units of F g^{-1}. However, in the LTO-AC anodes it might be more appropriate to use mA h g^{-1} units because the LTO exhibits relatively narrow reduction/oxidation peaks. Figure 16a and Figure 15 illustrate the specific gravimetric and volumetric capacities of different LTO-ACs in full-cell configuration at various charge-discharge rates, and then compare LTO-AC #3 with some recent reports. As a direct

comparison, AC//AC full cells were also fabricated, with commercial AC as a cathode and the spherical AC as an anode, and applied with the same current rates but a wider voltage range (0.5-2.7 V) to exclude the capacity contribution of spherical AC to LTO-ACs and, meanwhile to clarify the improvement of LTO-ACs. Figure 16a shows the impact of the composites' morphology and porosity on their capacity retention at ultrahigh rates. LTO-AC #1 with the smallest fraction of the mesopores (Figure 10c and Figure 13d) performs relatively poorly even at the lowest shown rate of 20C and at 50C or higher rates its capacity drops to the level close to that of a pure AC (Figure 16a). Similarly sized LTO-AC #2 with a larger (but still relatively small) content of 30-50 nm mesopores performs significantly better and retains up to 50% of its capacity at the 200C rate. LTO-AC #3 with the largest (although still moderate, Figure 10c) content of broadly distributed mesopores (Figure 13d) and the smallest average particle size (Figure 12g) showed remarkable rate performance characteristics, with specific gravimetric capacities as high as ~105 mA h g^{-1} at 350C (61 A g^{-1}). Because the majority of LTO nanoparticles are confined within the 0.5-4 nm electrically conductive carbon pores of approximately similar size in all three composites (Figure 10c), the results suggest that the rate-limiting step in the electrochemical reactions (Equation 3) is the transport of lithium ions, which is further supported by electrochemical impedance spectroscopy data (Figure 17).

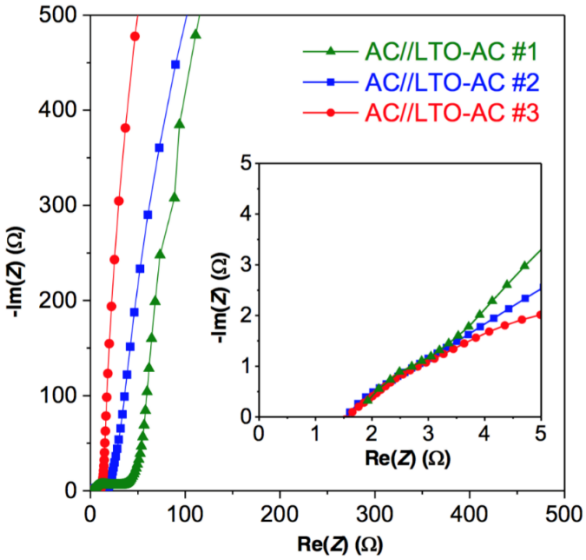

Figure 17. Electrochemical impedance spectroscopy data of the AC//LTO-ACs full cells. The inset shows the magnified high-frequency region.

For practical applications (when one needs to maximize the energy storage in a given device), it is very important to achieve high volumetric capacities of 53-78 mA h cc^{-1} could also be achieved in LTO-AC #3 at 350C-20C rates (Figure 15). These are up to 12 times higher than those of the empty AC spheres when tested in identical configurations (3-15 mA h cc^{-1} at comparable rates), thus providing dramatic improvements over state-of-the-art supercapacitor technology.

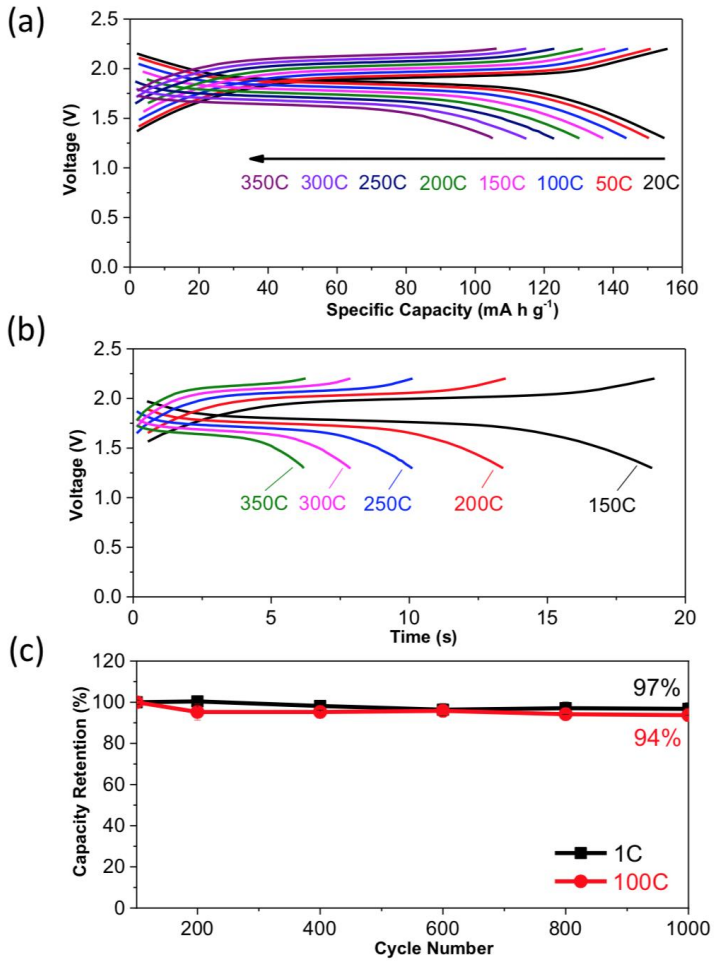

Figure 18. Electrochemical characterization of AC//LTO-AC #3 cells: (a) voltage-capacity profiles; (b) voltage-time profiles; (c) capacity retention over 1000 cycles at the rates of 1C and 100C.

In contrast to flat slopes in the galvanostatic charge-discharge voltage profiles of EDLCs (AC//AC full cells, Figure 19), the voltage profiles of AC//LTO-AC #3 cells exhibit a characteristic plateau (Figure 18a**)**. This is expected because the ion storage characteristics of the LTO-AC #3 electrode are dominated by the high capacity LTO nanoparticles. The rate performance of the LTO nanoparticles embedded within AC #3 is quite remarkable, and even when current densities are increased to very high values (150-350C) polarization (Figure 18a, b) remains small. Figure 18b also demonstrates

characteristic charge and discharge times at selected rates. It can be seen that at the highest current (350C), the LTO-AC #3 full cell can deliver 100 mA h cc^{-1} in ~ 6 s, which is comparable with that of the similarly built AC//AC cell in the same electrolyte (Figure 19). The cycle stability tests conducted on AC//LTO-ACs full cells (asymmetric electrochemical capacitor configuration) showed minimal capacity loss for over 1000 cycles at the rates of 1C and 100C (Figure 18c), which is important for commercial applications.

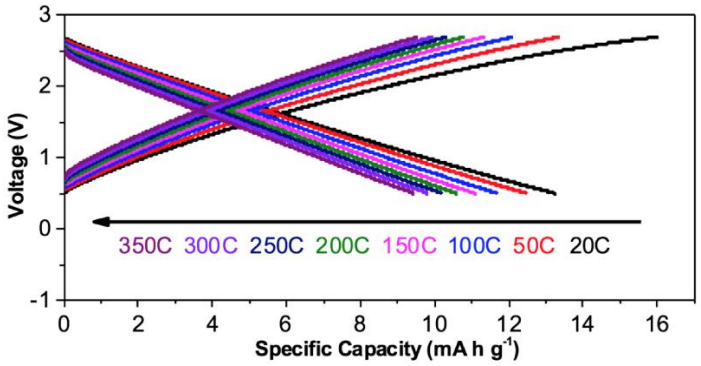

Figure 19. Voltage profiles of AC//AC full cells. Voltage range is 0.5-2.7 V.

Comparison with the highest-rate LTO electrodes reported in open literature, including carbon-coated LTO,[53] rutile-TiO_2-coated LTO,[54] hierarchically porous LTO,[26] LTO hollow spheres[30] and hydrogenated LTO nanowire arrays[33] shows a clear rate-performance advantage of the approach described here (Figure 16b) - the discharge rate of LTO-AC #3 is nearly an order of magnitude faster than that of the best nanostructured LTO electrodes reported so far. In fact, previous work on LTO seldom involves a performance study at the rates higher than 50C. In order to compare the results with some of the very promising recently reported supercapacitor materials, such as $NiMoO_4$ nanosheets,[55] hierarchical $MnMoO_4/CoMoO_4$ nanowires,[43] MoS_2 nanosheets,[42] titanium carbide "clay"[56]

and $CoMoO_4$-graphene,[57] their rate-performance curves were present in Figure 16c. It should be clear, however, that the comparison with the state-of-the art given in these two panels (Figure 16b and c) should be considered only qualitatively because many of such cells were constructed differently, using slightly different electrolytes and cell potential ranges. However, attractive capacity and rate performance characteristics of LTO-AC #3 materials are clearly visible and emphasize a great promise of the proposed approach to embed nanoparticles of intercalation-type materials (such as LTO) into microporous carbons for high-energy and high-power asymmetric supercapacitor applications.

In contrast to prior work, LTO-ACs described here contain the smallest (< 4 nm) and uniformly distributed LTO in a conductive porous carbon matrix, preventing the aggregation of these nanocrystals. The nanoporous–mesoporous structure of the composites allows for the significantly faster ion diffusion and charge transfer, thus manifesting superior rate capacities at all current densities and particularly at high rates (> 50C). Future work on the use of other porous carbons and optimizing the composite microstructure, density, and composition is expected to further enhance their performance. In addition to LTO, this innovative approach may be adjusted for use with other alkaline ion (Li, Na, K, *etc*.) intercalation-type active materials, thus offering multiple avenues for the formation of high-power energy storage devices to satisfy the rapidly growing industrial demands.

3.4 Conclusions

In summary, an efficient approach to prepare nanoporous carbons with LTO nanocrystals embedded into the carbon pores without inducing any significant pore

blockage has been demonstrated. XRD studies confirmed the LTO crystal structure. SEM and TEM analyses demonstrated that no LTO nanoparticles are present on the outer surface of the electrically conductive porous carbon particles. TEM studies in combination with EDS line scans further showed very uniform distribution of LTO within the porous carbon particles, which is quite remarkable considering the simplicity of this approach. Using a hybrid full-cell system with activated carbon counter electrodes allowed us to objectively characterize the real rate performance of LTO-AC powder samples. Such studies revealed a major impact of the porosity of such composites on their rate performance characteristics, and further suggested that carbon pores successfully provided rapid access of electrons directly to the electrochemical reaction sites within individual LTO nanoparticles, making ionic transport a rate-limiting step for this system and allowing optimization of the pore size distribution for the desired energy-power balance. The best composite samples with only a modest content of broadly distributed mesopores (5–50 nm) showed charge–discharge rates comparable to that of the pure AC double layer capacitor electrodes of comparable areal capacity loading, while offering significantly higher rate capability. More specifically, in comparison with pure AC, the produced LTO-ACs showed 12 times higher gravimetric capacity and 12 times higher volumetric capacity. Therefore, the proposed use of intercalation-type active material nanocrystals embedded into the nanoporous carbon pores shows great promises for use in asymmetric hybrid capacitors with high-power density and high-energy density characteristics.

CHAPTER 4. FROM LITHIUM TITANATE TO OTHER METAL OXIDES

4.1 Introduction

Inspired by the LTO-AC work in Chapter 3, I was interested to examine if this synthetic method fits for a broader scale of metal oxides-porous carbon nanocomposites which enable ultra-high charge/discharge rates. As a similar electrode material to LTO in terms of both chemical and electrochemical properties, TiO_2 has attracted enormous interest in the past decades, owing to its abundance, low cost, environmental compatibility and safety, *etc*. exceeding those of LTO. TiO_2 also delivers higher specific capacity than LTO.

TiO_2 exhibits a flat lithiation potential plateau at a little higher voltage than LTO, ~1.75 V *vs*. Li/Li^+. However, different from the "near-zero" volume change during (de)lithiation of LTO, TiO_2 has less than 4% volume expansion, which is also small enough for maintaining a robust crystal structure. On the other hand, TiO_2 suffers from poor electronic conductivity and lithium ion diffusivity, resulting in poor cyclability and rate-capability at high current rates. Researchers have reported nanostructured TiO_2 in combination with highly conductive materials, such as carbon nanotube (CNT) and graphene, to improve both ionic and electronic conductivities. However, in most cases, the very close packing of nanosized TiO_2 leads to severe agglomeration and leaves very limited access of the interior particles to the electrolyte. In addition, nanostructured TiO_2 is also time and cost consuming to process.

4.2 Experimental Methods

The synthesis of TiO_2-ACs is similar but not identical to LTO-ACs. Specifically, 250 mg colorless titanium(IV) butoxide (reagent grade, 97%, Sigma-Aldrich, USA) was directly added dropwise to 100 mg spherical nanoporous activated carbon (AC) in an argon-filled glovebox. Vacuum was applied during the interval of every two additions. The precursor-AC composites were then preheated in air at 300 ^oC for 1 h, followed by hydrolysis of Ti precursors in hydrothermal condition at 120 ^oC for 6 h, yielding immature TiO_2 crystal structure. Finally, the as-prepared composites were calcined at 800 ^oC in argon atmosphere for 10 h to crystalize TiO_2.

Materials Characterization and *Electrochemical Measurements* are identical to Chapter 3.

4.3 Results and Discussion

Following the synthetic method of LTO-AC, the synthesis of TiO_2- activated carbon nanocomposites (TiO_2-AC) has been studied similarly, however, the *in-situ* formation of crystalline TiO_2 proved to be different. Initially, the same experimental method adopted in LTO-AC synthesis was used – infiltration of Ti precursors followed by pre-heat in air and high-temperature annealing. Interestingly, only amorphous phase of decomposed precursor in AC was detected. In result, low temperature (< 600 ^oC) solid calcination failed to crystalize TiO_2, while at high temperature (> 600 ^oC) Ti(0) was yielded, indicating the reduction of amorphous Ti(IV) by ACs. Different from LTO, the precursor decomposition, TiO_2 formation and crystallization demanded a hydrolysis process. Note that oxidizing Ti(IV) butoxide in air produced crystalline TiO_2. Therefore,

the nanoconfinement by nanoporous AC clearly played a significant role affecting this synthesis. Carbon nanopores may possibly constraint the accessibility of Ti precursor to the moisture needed for the formation of TiO_2. Therefore, given this obstacle, in order to activate the hydrolysis of TiO_2 precursor, hydrothermal treatment was introduced in combination with solid state synthesis. After amorphous phase in AC was formed, the powder was placed in an autoclave filled by DI water only, and hydrothermal conditions were applied for 6 h.

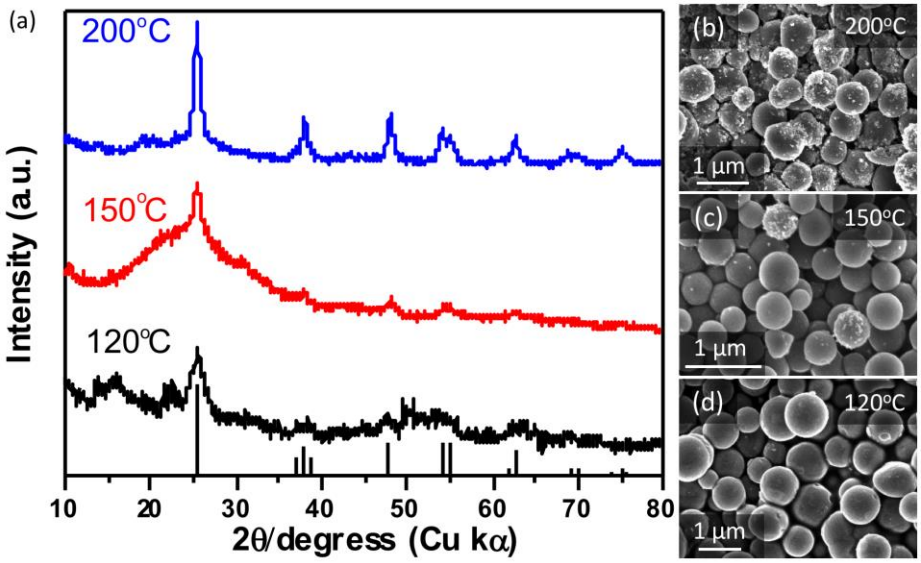

Figure 20. (a) XRD patterns of the precursor powder treated at different temperatures in hydrothermal reaction; SEM images of the powders after (b) 200 °C, (c) 150 °C, and (d) 120 °C treatment.

As shown in the Figure 20, crystalline TiO_2 was successfully produced at 120 °C, 150 °C and 200 °C. The crystalline structure becomes more ordered as temperature grows, primarily due to the increasing mobility of semi-amorphous TiO_2 and the large difference in the surface energy between carbon (AC pores) and Ti-O compounds. Right after the hydrothermal treatment at 120 °C, the composite was annealed in argon (Ar) at 800 °C,

yielding pure phase anatase TiO_2 (Figure 21b). TGA (Figure 21a) data revealed that the ratio of TiO_2 to AC was 1:1 by weight. Microscopic characterization can be found in Figure 19. Similar to the LTO composites in Chapter 3, the morphology of TiO_2-AC composites was as uniform as fresh ACs. Dark dots in the TEM image and EDX line scan clearly demonstrated the uniform distribution of TiO_2 nanoparticles within porous carbon spheres.

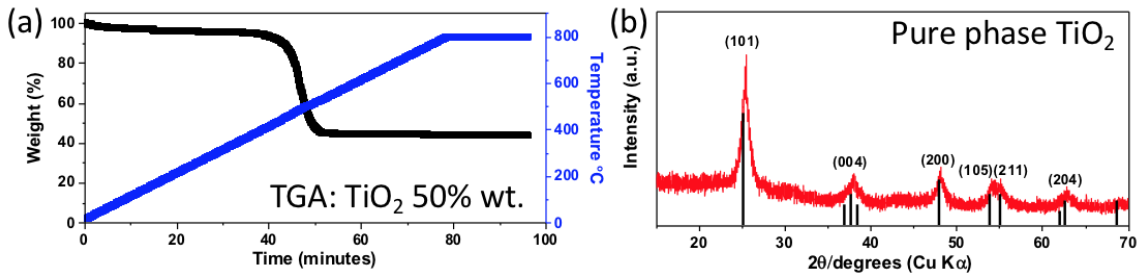

Figure 21. (a) TGA curve of LTO-ACs at 10 ºC min^{-1} in air; (b) XRD patterns of the annealed TiO_2-AC composite.

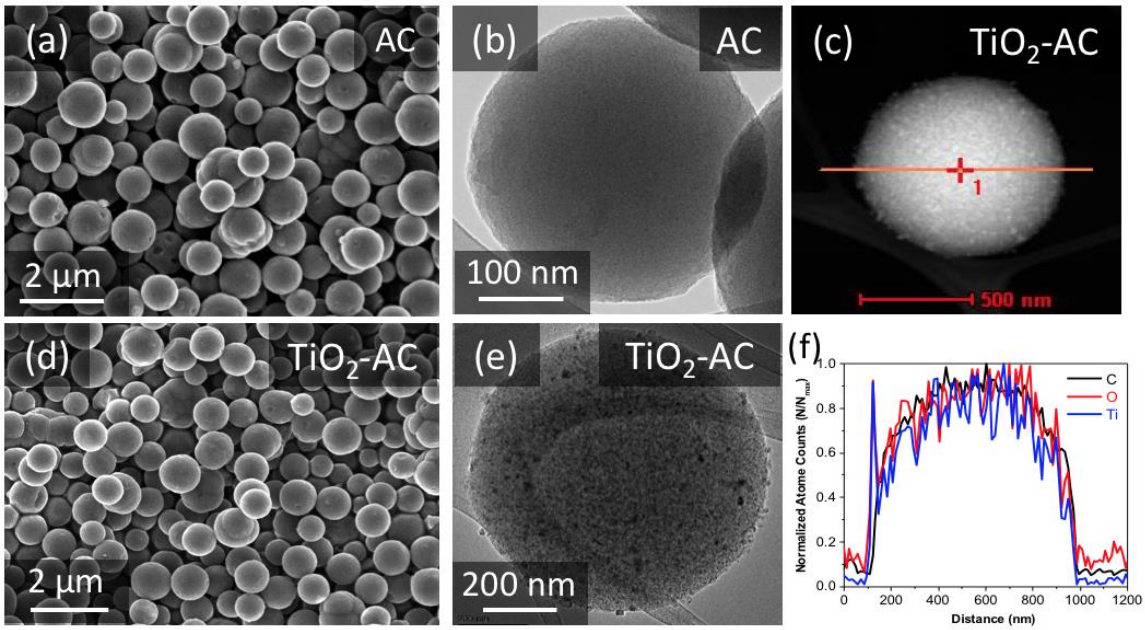

Figure 22. SEM and TEM images of as-synthesized empty AC and TiO_2-AC composite: (a, b) empty AC; (d, e) TiO_2-AC; STEM image (c) and EDS line scan results (f) of TiO_2-AC nanocomposites, showing uniform distribution of TiO_2 within a sphere.

Electrochemical characterization of the TiO_2-AC composite in a full-cell configuration (coin cell) revealed excellent rate performance and good stability (Figure 23), 75 mA h g^{-1} at the current rate of 300C (1C= 167.5 mA g^{-1}) with near 100% capacity retention after 500 charge-discharge cycles. This result outperforms most of the previously reports to my knowledge.

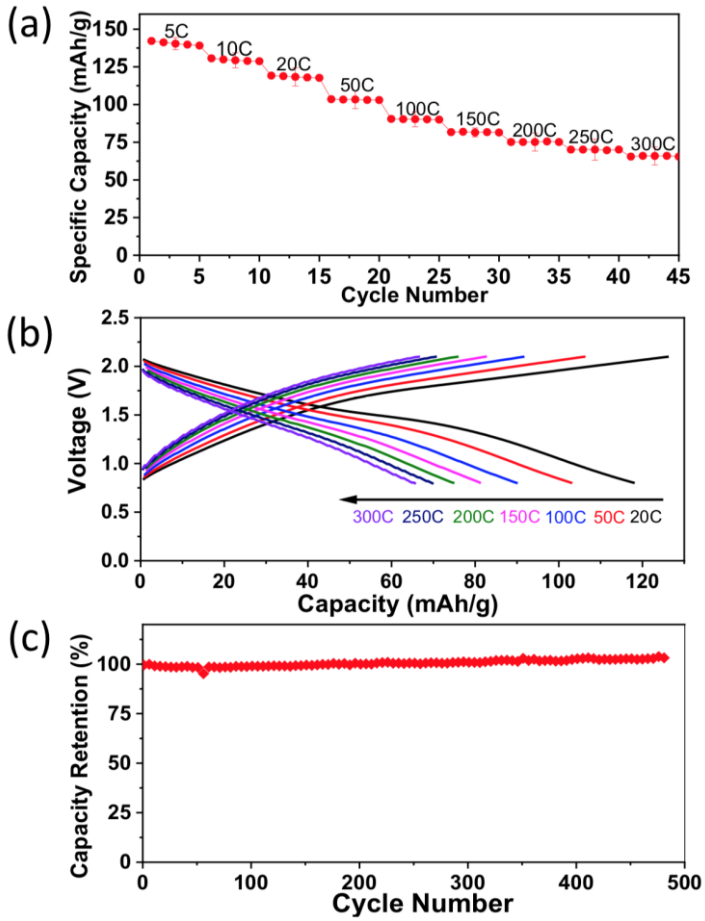

Figure 23. Electrochemical characterization of AC// TiO_2-AC cells: (a) specific gravimetric performances and (b) voltage-capacity profiles at different current rates; (c) capacity retention over ~ 500 cycles at the rate of 1C.

4.4 Conclusions

So far, the strategy of infiltrating LTO and TiO_2 into porous carbon has been proven to be an effective approach to improve both electronic and ionic conductivity. Additionally, NiO, MnO and Cu_2O were also nanoconfined in the carbon pores using Mn(II) acetate as shown in Figure 24, Ni(II) acetate, tetrahydrate and $Cu(BF_4)_2 \cdot xH_2O$ as precursors, respectively. In most cases, at least one organometallic compound can be found that is either in liquid state at room temperature or highly soluble in organic solvents and that could be converted into specific metal oxides. A series of precursor infiltration, pre-heat decomposition in air, hydrothermal condition, high-temperature annealing could be developed into a successful methodology for a variety of metal oxides. AC substrate with tunable surface properties may have a significant impact on the infiltration procedure. The chemical properties of the metal oxides are also critical to this process considering their compatibility with carbon. Some transitional metal oxides that could catalyze the oxidation of carbons (such as Fe, Co, Ni, Mn, Cu, *etc*.) may only be produced at their low oxidation states by such a strategy.

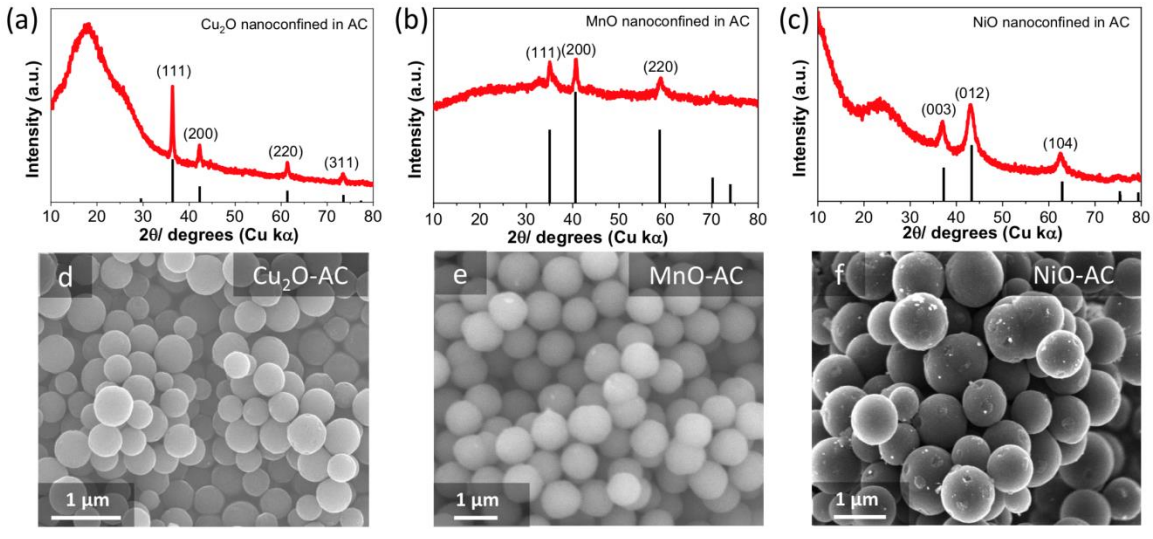

Figure 24. XRD and SEM of nanoconfined Cu_2O (a, d), MnO (b, e), and NiO (c, f).

CHAPTER 5. IRON (III) FLUORIDE NANOCONFINED IN CARBON NANOFIBERS AS FREE-STANDING CATHODES FOR HIGH-ENERGY LITHIUM BATTERIES

Reproduced from **Advanced Functional Materials**, 2018, 1801711, †W. Fu, †E. Zhao, Z. Sun, X. Ren, A. Magasinski, G. Yushin, *Iron Fluoride-Carbon Nanocomposite Nanofibers as Free-Standing Cathodes for High-Energy Lithium Batteries*, Copyright (2018), with permission from WILEY-VCH Verlag GmbH & Co. KGaA, Weinheim. (See Appendix A for the permission letter)

The development of low-cost, high-energy cathodes from non-toxic, broadly available resources is a big challenge for the next-generation rechargeable lithium or lithium-ion batteries. As a promising alternative to traditional intercalation-type chemistries, conversion-type metal fluorides offer much higher theoretical capacity and energy density than conventional cathodes. Unfortunately, these still suffer from irreversible structural degradation and rapid capacity fading upon cycling. To address these challenges, this chapter harnesses a versatile and effective strategy for the development of metal fluoride-carbon (C) nanocomposite nanofibers as flexible, free-standing cathodes. By taking iron trifluoride (FeF_3) as a successful example, assembled FeF_3-C/Li cells with a high reversible FeF_3 capacity of 550 mAh g^{-1} at 100 mA g^{-1} (3 times that of traditional cathodes, such as lithium cobalt oxide (LCO), lithium nickel cobalt aluminum oxide (NCA) and lithium nickel cobalt manganese oxide (NCM)) and excellent stability (400+ cycles with little-to-no degradation) are demonstrated. The promising characteristics could be attributed to the nanoconfinement of FeF_3 nanoparticles, which minimizes the segregation

of Fe and LiF upon cycling, the robustness of the electrically conductive C network and the prevention of undesirable reactions between the active material and liquid electrolyte using the composite design and electrolyte selection.[58]

5.1 Introduction

Beyond the intercalation chemistry, conversion-type cathodes have recently attracted significant attention.[59] Featuring high theoretical capacity (1675 mAh g^{-1}; 1935 mAh cc^{-1}), low cost and abundance in the Earth crust, sulfur (S) has been extensively studied in Li-S battery systems.[60-63] However, several issues are still facing S cathodes, such as low potential versus Li/Li^+ and the dissolution of intermediate lithium polysulfides in electrolyte.[64-66] Metal fluorides (*e.g.* FeF_3, FeF_2, NiF_2, *etc.*) hold great promise for cathode applications due to their high energy and low cost.[67-70] Fe, in particular, is well known as the fourth most abundant element in the Earth crust and the cheapest metal in the market. The high theoretical capacity of FeF_3 (712 mAh g^{-1} and 2196 mAh cc^{-1} gravimetric and volumetric capacities, respectively) and higher theoretical potential than S make this material particularly promising.[70-72] Unfortunately, most metal fluorides (including FeF_3 and LiF, the product of the conversion reaction: $3Li + FeF_3 \rightarrow 3LiF + Fe$) are reported to exhibit very poor electric conductivity because of the high ionic strength of the metal-fluoride bond and the resulting large band gap.[72-74] The large interfacial energy of the metal (e.g., Fe)/LiF interface encourages the growth of large metal and LiF clusters during cycling, which increases the mass transport resistance. The unfavorable interactions between this cathode and electrolyte additionally increase the cell resistance and contribute to Fe dissolution and degradation, thus leading to low rate capability along with irreversible structural changes and rapid capacity fading upon cycling.[67, 75]

To overcome these issues, several strategies have been recently proposed. For instance, Ma *et al*. developed a conductive polymer coating on microporous FeF_3 by *in situ* polymerization and achieved an enhanced capacity of 210 mAh g^{-1} at a current density of 20 mA g^{-1} and 120 mAh g^{-1} at 1 A g^{-1}.[76] Reddy *et al*. synthesized nanoscale FeF_2 crystallites clamped in graphite matrix and obtained a specific capacity of up to 418 mAh g^{-1} at 40 °C after 25 cycles.[77] Recently, our group infiltrated FeF_2 into porous activated carbon to produce FeF_2-C composite cathodes, which can realize 90% of its theoretical capacity at a slow C/20 rate with 80% capacity retention at 150 mA g^{-1} after 200 cycles.[69] Although these strategies enhanced the electrochemical performance to some extent, further substantial progress in the development of stable FeF_3 and other metal fluoride cathodes is urgently needed. In addition, there is a growing need to develop flexible battery electrodes for wearable electronics and other applications.[78-80]

Herein, this chapter demonstrates that Li-FeF_3 batteries with long cycle life can be produced by utilizing nanocomposite FeF_3-carbon nanofiber (NF) cathode. The conductive NF network not only effectively nanoconfines the fluoride nanoparticles within an electrically conductive matrix preventing their irreversible aggregation and separation, but also protects them from structural damages, provides ultrafast pathways for ion diffusion and electron transport and minimizes undesirable reactions with liquid electrolyte. As a result, this work achieved a high reversible capacity of over 500 mAh g^{-1} with almost 100% capacity retention for 400+ cycles, substantially exceeding performance of the state of the art. Other metal fluorides may be similarly integrated into such flexible, free-standing electrode using the proposed methodology.

5.2 Experimental Methods

Efforts have been made to infiltrate Fe precursors in carbon pores, similar to Chapter 3 and 4. Actually, $FeCl_3$ particles were successfully infiltrated using methanol as the solvent. However, after the gas-phase fluorination with NF_3 at 300 ^oC, FeF_3 was diffused outside pores. This may due to the weak bonding between activated carbon surface and metal halides. Therefore, to freeze the movement of FeF_3 precursor, one-step electrospinning followed by carbonization was proposed.

5.2.1 Fabrication of Free-Standing Cathodes

The FeF_3-C NFs are fabricated by a combination of electrospinning, carbonization/reduction and fluorination procedures. First, 1.5 g ferric acetylacetonate ($Fe(acac)_3$, Alfa Aesar, USA) was dissolved into 11.5 g N, N-dimethylformamide (DMF, Sigma Aldrich, USA) by magnetic stirring for 30 min to form a homogeneous solution. Then 1 g polyacrylonitrile (PAN, M_w = 150 000, Sigma Aldrich) was added into the solution and stirred at 50 °C for 12 h to form a gel precursor solution. The electrospinning was conducted using a syringe loaded with a needle and 3 mL of as-prepared solution at 20 kV for 3 h. A piece of aluminum foil (15 cm × 15 cm) was used as the collector and the distance between the needle tip and aluminum collector was 20 cm. After electrospinning, the obtained precursor membrane was peeled off, cut into discs with a diameter of 16 mm and then stabilized in air at 220 °C for 1 h. After that, the samples were carbonized in argon (Airgas, USA) at 600 °C for 2 h and reduced in hydrogen (4% hydrogen in argon, Airgas) gas to form Fe-C NFs. Finally, the Fe-C NFs were treated with NF_3 gas (2% NF_3 in helium, Linde Electronics & Specialty Gases, USA) at 300 °C for 2 h to obtain FeF_3-C NFs. After fabrication, the samples were immediately transferred into in a glove box filled with argon gas at room temperature for future use.

5.2.2 Material Characterization

The crystal structure and chemical composition of prepared samples were identified by X-ray diffraction (XRD, X'pert PRO, Alpha-1, USA) with a Cu Kα radiation at 40 kV and X-ray photoelectron spectrometer (XPS, Thermo K-Alpha XPS,). The microstructure was examined using scanning electron microscopy (SEM, Hitachi SU8010, Japan) and transmission electron microscopy (TEM, FEI Tecnai G2 F30, Netherlands). Energy dispersive X-ray spectroscopy (EDS) was performed using Tecnai G2 F30. Thermogravimetric analysis (TGA) was cuducted on Q600 TGA/DSC system (TA Instruments, USA). The Brunauer–Emmett–Teller (BET) analysis was conducted using TriStar II 3020 surface area and porosity measurement system (Micromeritics Inc., GA, USA).

5.2.3 Electrochemical Measurements

Coin-type cells (2032-type) were assembled using as-prepared FeF_3-C NFs as a free-standing, additive-free cathode, lithium metal as counter and reference electrodes and a piece of polypropylene membrane (2400 type, Celgard, USA) as a separator. Lithium bis(fluorosulfonyl)imide (LiFSI, Nippon Shokubai, Japan) was dissolved into dimethoxyethane (DME, Sigma Aldrich) to yield 4.6 M electrolyte. All the assembly process was carried out in a glove box filled with argon gas at room temperature. The electrochemical performance was characterized using cyclic voltammetry (CV), electrochemical impedance spectroscopy (EIS) and galvanostatic charge-discharge tests. The CV and EIS were performed on a Gamry Potentiostat (Gamry Instruments, USA).

Galvanostatic charge-discharge was conducted using an Arbin system (Arbin Instruments, USA).

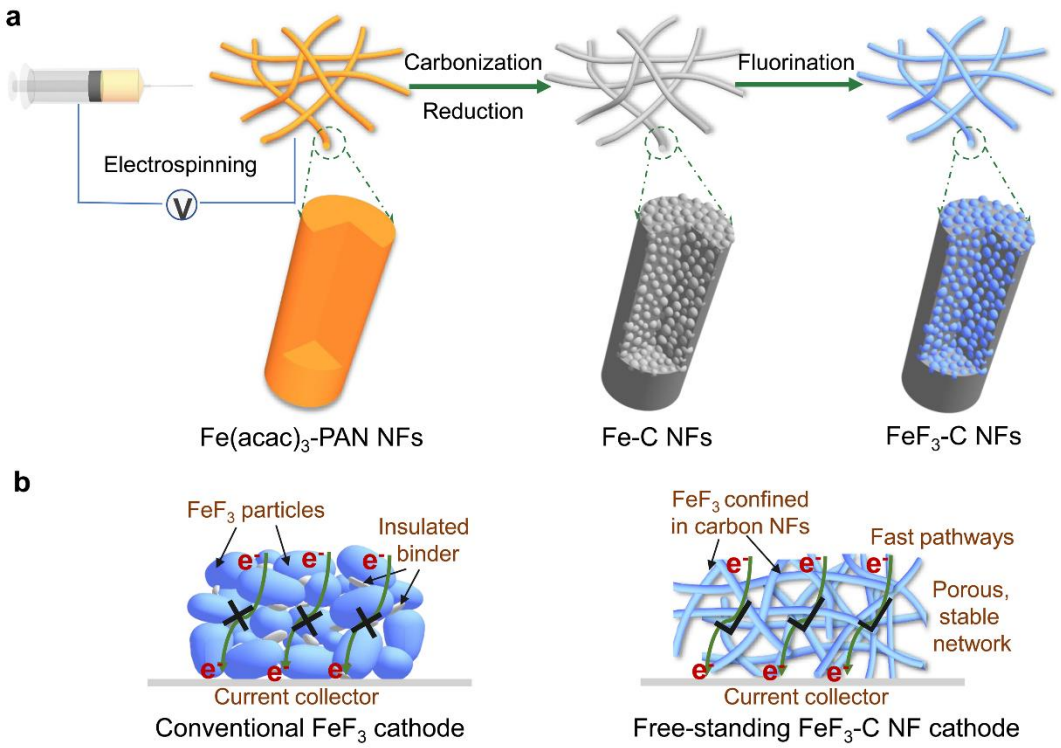

Figure 25. (a) Schematic fabrication of free-standing FeF_3-C NF cathodes, which involves electrospinning precursor nanofibers, carbonization/reduction and fluorination processes; (b) a schematic comparison of conventional cathodes and this flexible, free-standing cathodes, the later providing more robust pathways for electron transport and faster pathways for ion transport.

5.3 Results and Discussion

Figure 25a illustrates this methodology for the formation of flexible, free-standing nanocomposite nanofiber (NF) - based cathodes. In brief, a ferric acetylacetonate ($Fe(acac)_3$)-polyacrylonitrile (PAN) solution was electrospun onto aluminum foil collector producing a nanofiber membrane, which was peeled off and cut into discs for further treatments and subsequent electrochemical testing in cells. The nanofiber membrane

samples were carbonized in argon (Ar) at 600 °C for 2 hours and then the Fe precursor was reduced in hydrogen (H_2) at 500 °C for 1 hour to form Fe-C nanocomposite NFs. After the subsequent treatment with diluted NF_3 gas at 300 °C for 2 hours, the Fe-C NFs were finally converted into FeF_3-C nanocomposite NFs.

Conventional FeF_3 electrodes (Figure 25b) are historically prepared by coating a slurry comprising active materials (or active materials ball-milled with carbon or oxide materials to form composites), polymer binder and conductive additives onto a current collector. The low conductivity of fluorides in combination with the insulating nature of a binder and volume changes in the active material typically lead to an electrical/electrochemical separation of active material during cycling. In addition, the relatively large size of the active particles, relatively small pores within the electrode and high pore tortuosity in combination with electrolyte decomposition (with the subsequent formation of the insulative and blocking solid electrolyte interphase, SEI) commonly increase electrolyte diffusion time within the electrode and Li^+ diffusion time within the particles and leads to undesirable rise of the cell resistance. Furthermore, conventional electrodes cannot be flexed to a low bending radius without being fractured. In contrast, the NF shape of FeF_3-C nanocomposite materials allows for sufficient material flexibility in the NF-based electrodes, the conductive C in the NFs allows for rapid access to electrons, and the small NF diameter allows for rapid Li^+ transport to/from electrochemical reaction sites (Figure 25b). Furthermore, the confinement of FeF_3 nanoparticles within NF prevents their irreversible clustering and segregation of Fe and LiF, which otherwise lead to rapid cell resistance increase. The lack of any binders and additives and relatively large porosity within the free-standing electrode structure contribute to faster electrolyte diffusion at the

electrode level, while the electrically conductive nature of the interconnecting nanocomposite NFs not only enhances the electrode conductivity, but also provides excellent mechanical stability needed for long-term cycling performance.

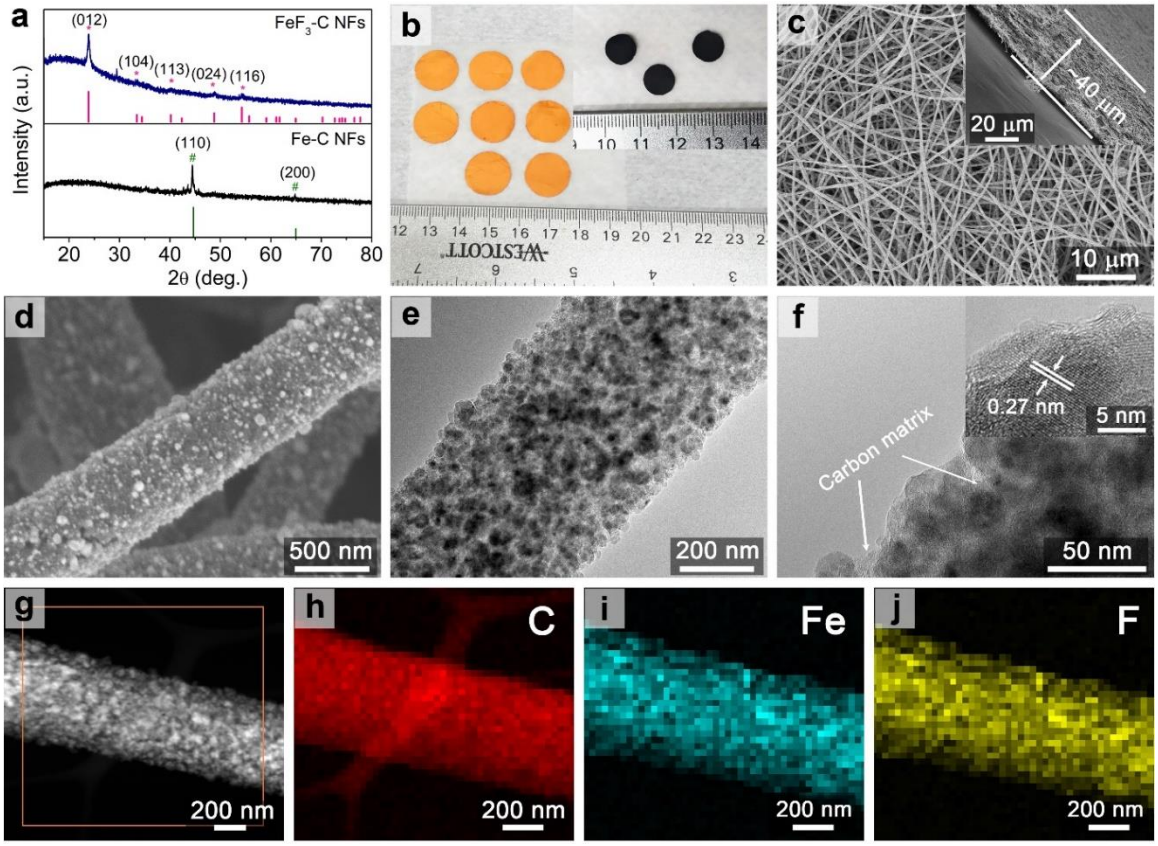

Figure 26. (a) XRD patterns of as-prepared Fe-C NFs and FeF_3-C NFs; (b) photos of the electrospun membrane discs (orange) and the eventually obtained FeF_3-C (inset of b, black); (c, d) SEM and (e, f) TEM micrographs of the FeF_3-C NFs; (g–j) EDS element maps of the FeF_3-C NF from the selected area.

Figure 26 illustrates structural and morphological features of the produced FeF_3-C NF samples. X-ray diffraction (XRD) patterns of as-prepared Fe-C NFs revealed successful decomposition of the $Fe(acac)_3$-based precursor and its transformation to cubic Fe (JCPDS card no. 85-1410) after carbonization and reduction (Figure 26a). During fluorination, the NF_3 gas reacts with metallic Fe nanoparticles and evidently converts them into anhydrous,

rhombohedral FeF_3 (JCPDS card no. 33-0647) within FeF_3-C NFs (Figure 26a). There's an unknown peak at 29°, which disappears in repeat testing. Note that the gas fluorination process did not damage the conductive carbon structure. The chemical composition of FeF_3-C NFs was additionally confirmed by X-ray photoelectron spectroscopy (XPS). The survey spectrum (Figure 27) indicates that the FeF_3-C NFs consists of C, N, F and Fe elements and among them the C and N are mainly from the N-doped C derived from PAN.

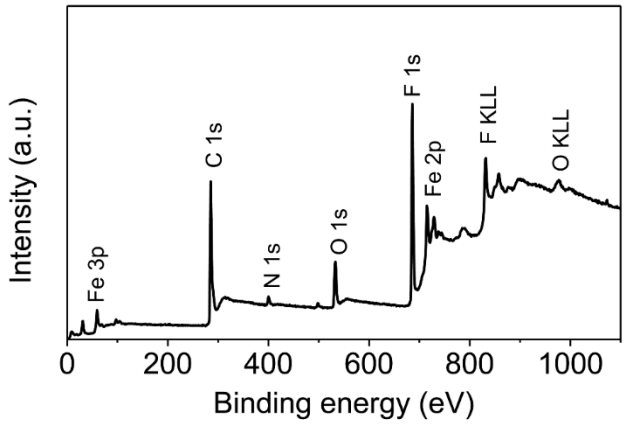

Figure 27. XPS survey spectrum of the FeF_3-C NF 600.

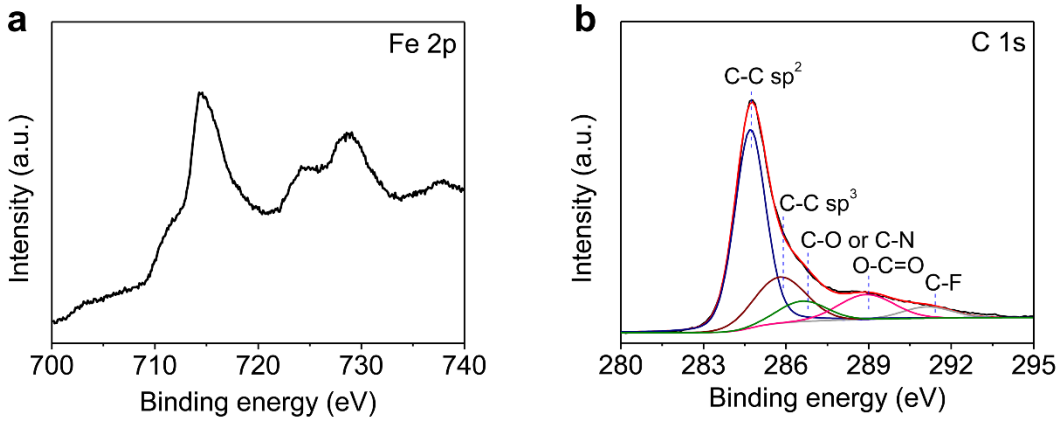

Figure 28. High-resolution XPS spectra of Fe_{2p} (a) and C_{1s} (b) for the FeF_3-C NF 600.

The high-resolution spectra of Fe 2p and C 1s (Figure 28) reveal the Fe^{3+} species and Fe-F bond in the FeF_3 and a strong graphitic C-C bond at (284.7 eV) in the carbon NFs.

Three peaks at 285.8, 286.6 and 289 eV can be assigned to sp^3 type carbon, C-O (or C-N) and O-C=O groups, respectively.[81-82] Besides, the C 1s scans indicate very low fraction of C-F bonds at 291.2 eV (Figure 28). The digital optical images of the NF membrane (Figure 25b) demonstrate that the black FeF_3-C NF membranes keep the shape but exhibit a smaller diameter (~8.5 mm) compared with the orange membrane precursor (~16 mm). The black color of the FeF_3-C is consistent with a very small fluorination of carbon (note that carbon monofluoride, CF_x, is white). To detail their microstructure further, scanning electron microscopy (SEM) and transmission electron microscopy (TEM) analyses were conducted. The FeF_3-C composite samples are composed of many ultra-long NFs with a diameter of 300–500 nm (Figure 26c, d) and these NFs interconnect with each other to foam porous, free-standing membranes. From the cross-section SEM micrographs (inset in Figure 26c), the typical thickness of the produced free-standing electrode was estimated to be ~40 μm. It should be noted that the thickness can be easily controlled by adjusting the electrospinning time and spinning conditions. The NFs have a rough surface with some small FeF_3 nanoparticles visible, presumably due to the substantial shrinkage of the PAN precursor during carbonization. As expected, pure carbon NFs prepared using the same method without Fe precursors show a very smooth surface (Figure 29).

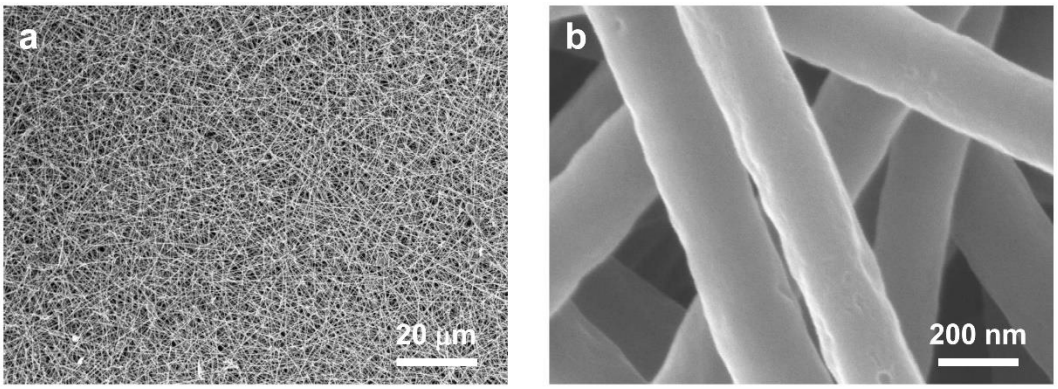

Figure 29. SEM images of pure carbon nanofibers.

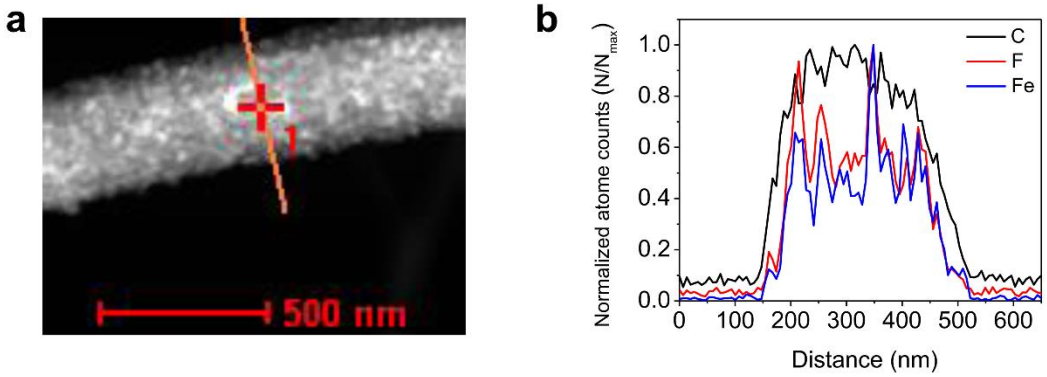

Figure 30. EDS linear scan for the FeF_3-C NF. (a) STEM image and (b) obtained spectra for C, F and Fe.

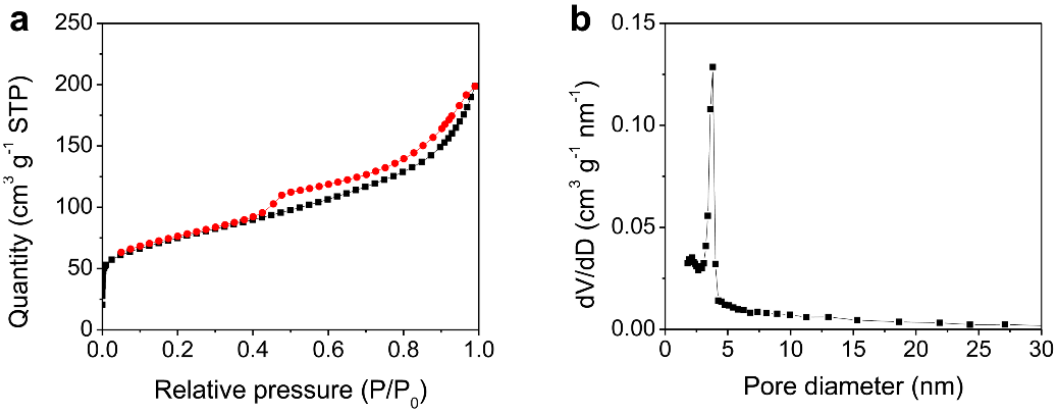

Figure 31. (a) Nitrogen absorption/desorption isotherms and the corresponding pore size distribution (b) of the FeF_3-C NFs. The calculated surface area is ~ 262 m^2 g^{-1}.

TEM and scanning TEM (STEM) micrographs (Figure 26e, f) clearly show that these FeF_3 nanoparticles exhibit an average size of 20–50 nm and are homogeneously distributed within the bulk of the NFs and confined by carbon matrix to form uniform one-dimensional nanocomposite structures. The high-resolution TEM micrograph shows an interplanar spacing of ~0.27 nm corresponding to the (104) plane of crystalline FeF_3 (inset in Figure 26f). In addition, energy dispersive spectroscopy (EDS) element maps of C, F and Fe explicitly indicate the homogeneity of each component in the NFs (Figure 26g–j), in agreement with the EDS spectra from a linear scan across the fiber (Figure 30). In addition, nitrogen adsorption/desorption isotherms reveal that the FeF_3-C NFs have a high surface area of 262 $m^2 g^{-1}$ with pore diameters of 2–5 nm (Figure 31), which can benefit the electrolyte diffusion.

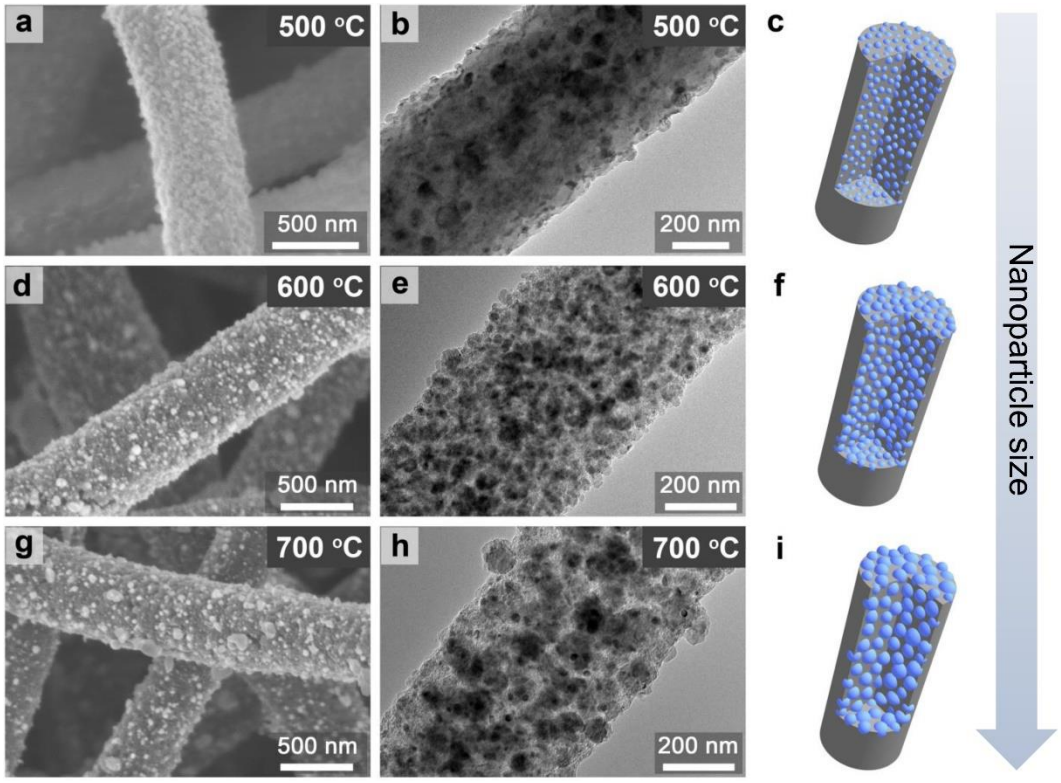

Figure 32. Morphological characterization of prepared FeF_3-C NFs using different carbonization temperatures (500, 600 and 700 °C); (a, d and g) SEM micrographs, (b, e and h) TEM micrographs, and (c, f and i) schematics, illustrating coarsening of the FeF_3 nanoparticles at higher temperature.

Generally, carbonization temperature plays a vital role in determining the size of nanoparticles in carbon fibers. To reveal the effect of different carbonization temperature, herein the FeF_3-C NF samples using different carbonization temperatures (500, 600 and 700 °C, the samples were named as FeF_3-C NF 500, 600 and 700, respectively) were prepared and their morphology using SEM and TEM (Figure 32) were investigated. All the three conditions resulted in a successful formation of FeF_3-C NFs, however, larger-sized nanoparticles formed in the FeF_3-C NF 700 sample than in the others due to nanoparticle coarsening at such a high temperature (Figure 32c, f and h). It is surprising that the nanoconfinement of Fe within the PAN-derived C matrix effectively prevented formation

of micron-scale particles of Fe (and eventually FeF_3), which were typically observed when Fe nanoparticles are annealed under similar conditions. Still, some FeF_3 coarsened to a sufficiently large diameter (up to ~100 nm) on the NF surface. It is also possible that a few of the nanoparticles might have diffused out of surface layer of the NFs. Higher carbonization temperatures should improve electrical conductivity of C while reducing the carbonization yield and thus increase the fraction of FeF_3 in the nanocomposites. To estimate the FeF_3 content, thermogravimetric analysis (TGA) for the three samples were conducted and summarized as shown in Figure 33. The FeF_3 fraction gradually increases from ~36 wt.% in the FeF_3-C NF 500 to 56 wt.% for the FeF_3-C NF 600 and 60 wt.% for the FeF_3-C NF 700. Increasing the mass ratio of the $Fe(acac)_3$/PAN precursor may increase the wt.% FeF_3 further, but at the expense of reduced mechanical properties, where samples can no longer be used as free-standing electrodes (Figure 34).

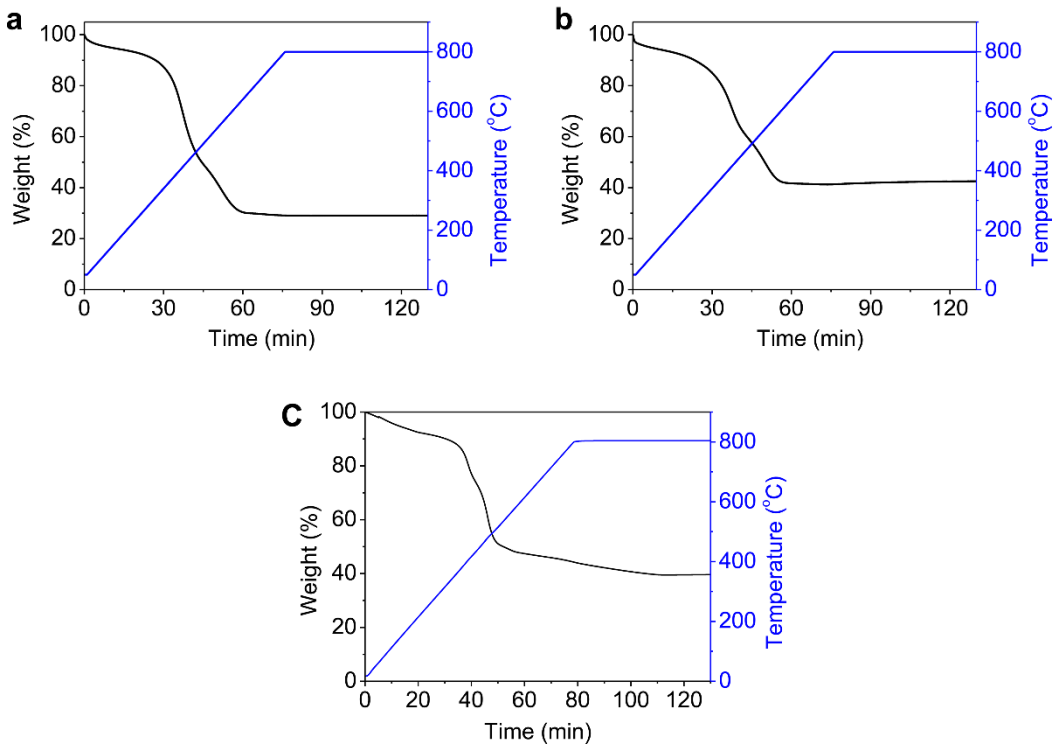

Figure 33. TGA plots of the obtained FeF_3-C NF samples with different carbonization temperatures, (a) 500 °C, (b) 600 °C and (c) 700 °C. The FeF_3 can totally convert into Fe_2O_3 after TGA tests. Based on the Fe atomic mass, the amount ratios of FeF_3 in the samples (500, 600 and 700) are ~36%, 56% and 60%, respectively.

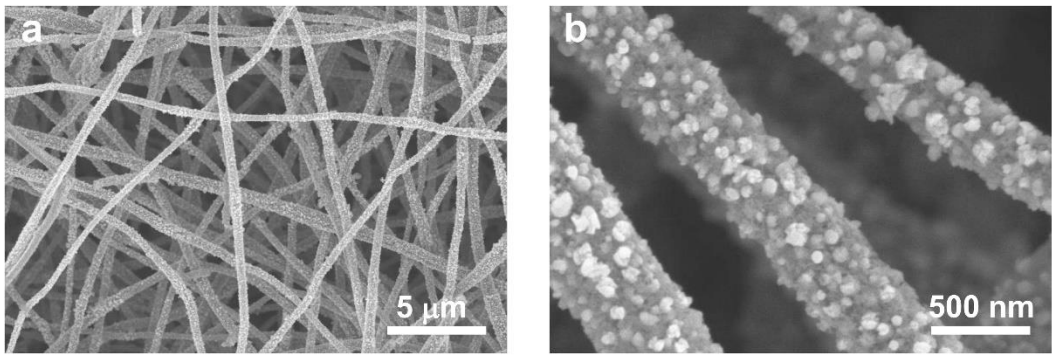

Figure 34. High-content FeF_3-C NFs. The mass ratio of the $Fe(acac)_3$/PAN in their precursor solution is 2:1.

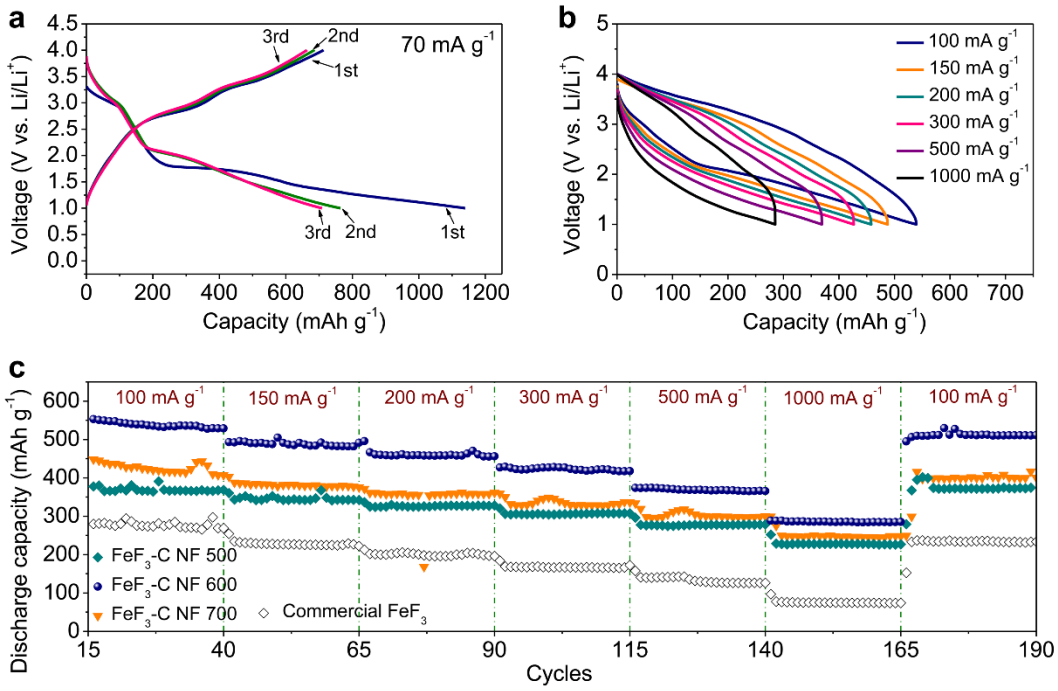

Figure 35. (a) Galvanostatic discharge/charge curves of the FeF_3-CNF 600 electrode at a current density of 70 mA g^{-1} with a voltage range of 1–4 V (vs. Li/Li^+); (b) voltage profiles of the FeF_3-C NF 600 electrode at various current densities (100–1000 mA g^{-1}); (c) rate capability of the FeF_3-C NF samples (500, 600, 700) in comparison with that of commercial FeF_3 nanoparticles (ball-milled with C additives; at the same or higher total C content in the electrode) at different current densities. Tester instrument error < 1%.

In the previous studies of our group, the advantages of using lithium bis(fluorosulfonyl)imide (LiFSI)-based electrolyte for the formation of *in situ* protection for conversion-type cathodes has been demonstrated.[83-84] To investigate the electrochemical performance of the produced samples, Li/FeF_3-C coin-type cells were assembled by using as-prepared FeF_3-C NFs as free-standing, additive-free cathodes, Li metal as counter and reference electrodes, and 4.6 M LiFSI/DME as electrolyte. Figure 35a shows the galvanostatic discharge-charge profiles of the FeF_3-C NF 600 electrode at a current density of 70 mA g^{-1} with a voltage range of 1–4 V (versus Li/Li^+). Two pairs of voltage plateaus are found at each discharge-charge curve, which can be ascribed to the

reversible conversion reactions between FeF_3/Li^+ and Fe/LiF associated with lithiation/delithiation process,[84-85] matching well with the redox peaks in the cyclic voltammogram (CV) curves (Figure 36). The first discharge curve shows a plateau at ~3 V, indicating that the Fe^{3+} from FeF_3 is gradually reduced to Fe^{2+} during Li intercalation ($Li^+ + e^- + FeF_3 \rightarrow LiFeF_3$). The second plateau at lower potential corresponds to the conversion reaction ($2Li^+ + 2e^- + LiFeF_3 \rightarrow 3LiF + Fe$).[86] The lower and longer plateau observed during the first discharge may be attributed to the initial over-potential often observed in conversion reactions,[66, 84] the lithiation of the slightly fluorinated carbon and the formation of cathode solid electrolyte interphase (CEI). Note that the CEI is rapidly passivating and after 15 cycles, the electrode shows a stable reversible capacity of ~580 mAh g^{-1} at 70 mA g^{-1} with a coulombic efficiency (CE) of 99.6% (Figure 37).

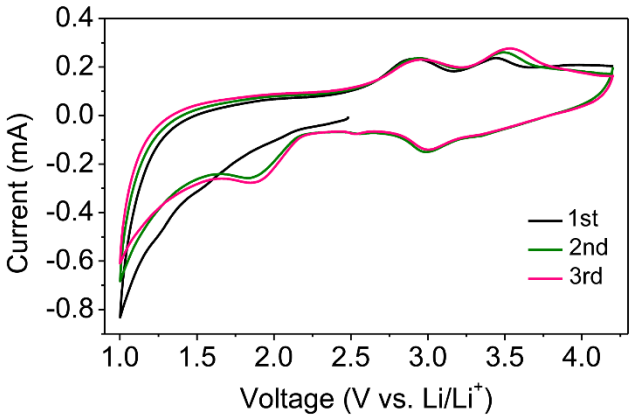

Figure 36. CV curves of the FeF_3-C NF 600 electrode at a scan rate of 0.5 mV s^{-1} with a voltage range of 1–4.2 V (vs. Li/Li^+).

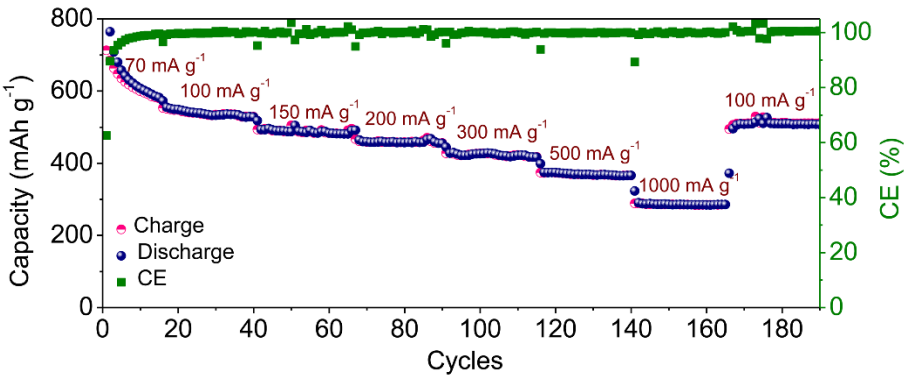

Figure 37. Charge/discharge capacity and coulombic efficiency (CE) of the FeF_3-C NF 600 electrode. Tester instrument error < 1%.

Rate capability was evaluated at different current densities (100–1000 mA g^{-1}) after 15 pre-cycles. The voltage profiles of different rates (Figure 35b) demonstrate similar loops with typical redox plateaus, suggesting good reversibility and favorable rate capability. A comparison of rate performance for different FeF_3 electrodes is presented in Figure 35c. It is found the FeF_3-C NF 600 electrode exhibits the best performance. A specific discharge capacity of ~550 mAh g^{-1} is achieved at 100 mA g^{-1}, much better than the FeF_3-C NF 500 (~380 mAh g^{-1}), FeF_3-C NF 700 (~440 mAh g^{-1}), commercial FeF_3 (280 mAh g^{-1}) and conventional cathodes such as $LiCoO_2$ (~150 mAh g^{-1})[87] and $LiMn_2O_4$ (120–140 mA h g^{-1}).[88-89] Although the capacity gradually decreases as the current density increases from 100 to 1000 mA g^{-1}, the FeF_3-C NF electrodes demonstrate excellent rate capability with high capacity retentions. Particularly, a high retention of 52% (~285 mAh g^{-1}) is achieved (at 1000 mA g^{-1}) for the FeF_3-C NF 600 electrode, in contrast to only 27% for commercial FeF_3. More notably, the FeF_3 electrode (FeF_3-NF 600) maintains a high capacity over 510 mAh g^{-1} after 190 cycles of the rate test, along with a high average CE of approximately 100 % (Figure 37).

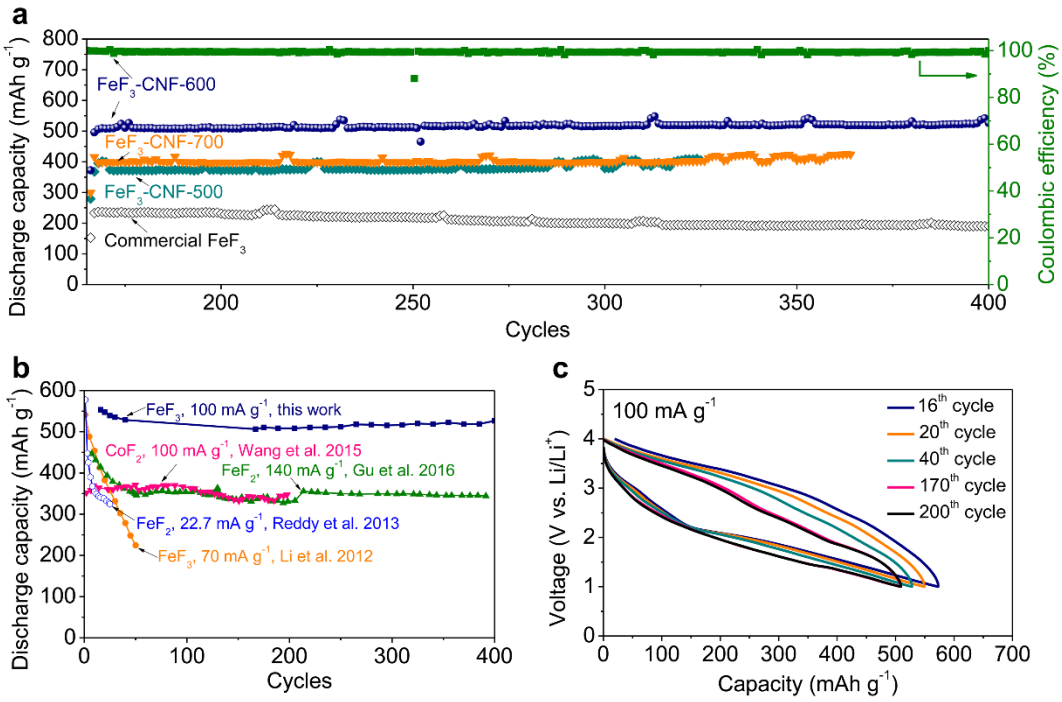

Figure 38. (a) Cycling performance of the cell based on free-standing FeF_3-C NFs and commercial FeF_3 at a current density of 100 mA g^{-1}; (b) a comparison of capacity and stability for various materials and previous prior-art studies; (c) voltage profiles of the FeF_3-C NF 600 at 100 mA g^{-1} for different discharge/charge cycles, showing reduction in the voltage hysteresis (overpotential). Tester instrument error < 1%.

Long-term cycling performance of the samples was evaluated at a current density of 100 mA g^{-1} after rate capability tests. Figure 38a compares the cycling stability of different electrodes. All the FeF_3-C NF electrodes show better stability compared to commercial FeF_3. Particularly, the FeF_3-C NF 600 electrode achieves an impressive reversible capacity over 520 mAh g^{-1} after 400 cycles, without any visible capacity decay. In contrast, the commercial FeF_3 sample possesses only 190 mAh g^{-1} with a retention of 68% of its initial value (the capacity of 16th cycle). Figure 38b summarizes the results and recent state-of-the-art studies on metal fluorides, including FeF_3,[70, 76] FeF_2,[77, 84] and CoF_2.[71] As expected, the free-standing electrodes (particularly FeF_3-C NF 600) stand out with unprecedentedly high capacity and stability, while the prior studies could not surmount the

limitations of low specific capacity and repaid capacity fading. For instance, the FeF_3 nanowire cathode showed a high discharge capacity of 543 mAh g^{-1} but retained only 223 mAh g^{-1} after 50 cycles.[70] In addition, the electrodes can deliver a high average CE of 99.8% for 400 stable cycles. Voltage profiles at different cycles are presented in Figure 38c and show similar shape with gradual decreasing hysteresis, which is indicative of reduced cell resistance, favoring the cell stability. Besides, the Li/FeF_3-C cells may exhibit a very high specific energy (Figure 39).[59]

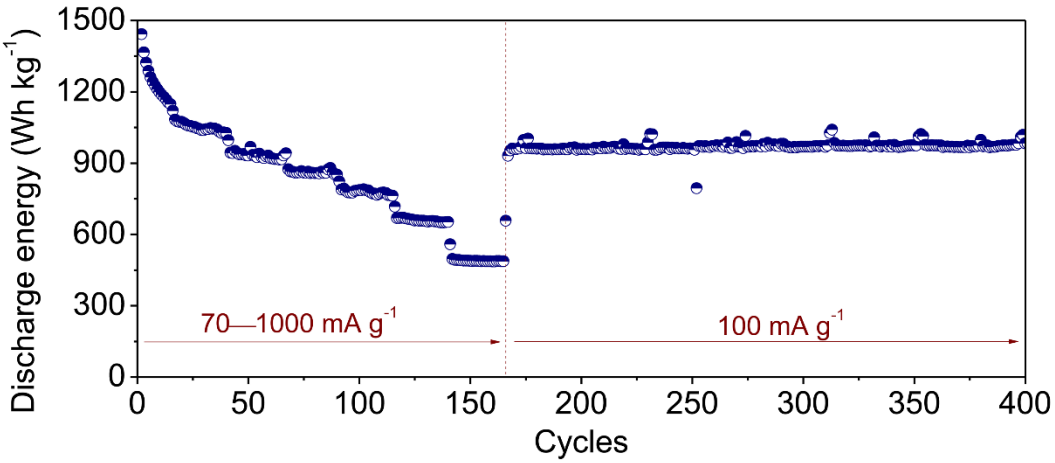

Figure 39. Discharge energy of the FeF_3-C NF 600 electrode, as defined by multiplying the FeF_3 specific capacity by an average voltage against Li/Li^+. Note that energy of the FeF_3/Li cell calculating unit (comprising 0.5 of the cathode current collector, one side of the cathode filled with electrolyte, separator filled with electrolyte, one side of the anode filled with electrolyte, 0.5 of the anode current collector) is different and substantially smaller. Tester instrument error < 1%.

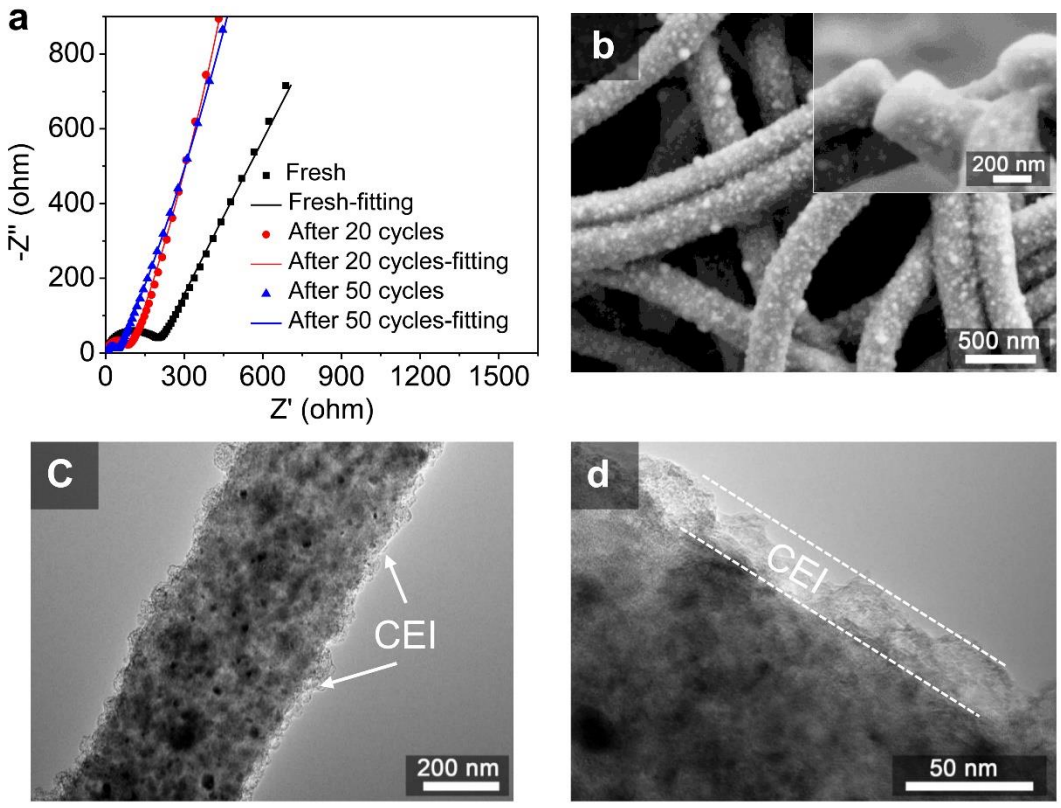

Figure 40. (a) Nyquist plots of the FeF_3-C NF 600 electrode after different cycles: fresh, after 20 and 50 cycles; (b) SEM and (c and d) TEM images of the FeF_3-C NF 600 electrode surface after 50 cycles.

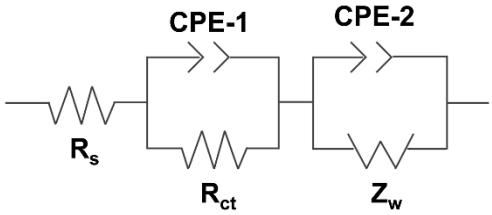

	R_s (Ω)	R_{ct} (Ω)
Fresh	3.1	189
After 20 cycles	2.2	82
After 50 cycles	2.4	38

Figure 41. The fitted equivalent circuit and corresponding R_s and R_{ct} valutes for the Nyquist plots.

Additional insights into the ion diffusion and charge transfer kinetics during cycling were assessed by electrochemical impedance spectroscopy (EIS). Figure 40a shows the obtained Nyquist plots of the FeF_3-C NF 600 electrode before and after 20 and 50 cycles (at 100 mA g^{-1}), which can be fitted with an equivalent circuit (detailed in Figure 41). The

change of bulk series resistance (R_s) remains small even after 50 cycles. The semi-circle associated with charge-transfer resistance (R_{ct}) gradually decreases as cycle number increases, demonstrating gradually enhancing ion diffusion and charge transfer, which was linked to the use of favorable electrolyte with good ionic conductivity (~5.7 mS cm^{-1}) and the formation of conductive CEI/SEI on both electrodes.[83, 90-91] The CEI passivation film can serves as a good Li^+ permeable layer and the possible formation of some small cracks within the NFs (which should be sealed by the self-passivating CEI) may enhance Li^+ transport to electrochemically reactive sites in the bulk of the NFs. To further reveal morphological changes during cycling, post-mortem SEM (Figure 40b) and TEM (Figure 40c, d) analyses were conducted after 50 cycles. Such studies reveled excellent mechanical integrity of the FeF_3-C electrodes after cycling, which retained their free-standing structure. The long nanocomposite NFs did not show any significant structural changes except for a thin-layer CEI coating (with a thickness of 10–20 nm) on the NF cathode (Figure 40d), as observed in our previous studies and involved *in situ* polymerization of LiFSI(-F) radicals to form a passivation layer on the cathode.[84] These analyses further suggest a great potential of the reported approach for applications of conversion-type FeF_3 and other metal fluoride cathodes in next-generation higher-energy Li or Li-ion batteries, including those for wearable electronics.

5.4 Conclusions

In conclusion, advanced lithium-metal fluoride batteries with high energy and long life has been realized by forming flexible, free-standing cathodes comprising nanocomposite FeF_3-C nanofibers, where FeF_3 nanoparticles nanoconfined within the conductive C matrix are produced by selective fluorination of Fe nanoparticles using

thermal treatment in a NF_3 gas. Compared with conventionally prepared electrodes, the free-standing FeF_3-C NFs demonstrate excellent capacity utilization and electrochemical stability with specific capacity over 500 mAh g^{-1} even after 400 cycles, which is largely improved compared with previously reported results. Post-mortem analysis revealed that promising performance characteristics could be attributed to the unique electrode structure which can effectively protect the FeF_3 nanoparticles from undesirable coarsening and segregation, while providing fast ion/electron pathways. Replacement of toxic, rare and expensive Co in conventional battery electrodes (LCO, NCM, NCA) by extremely cheap, abundant and much environmentally friendlier Fe in FeF_3 is particularly important for EV battery and grid storage applications, while the high specific cathode capacity (and thus light cathode weight) of FeF_3 in combination with FeF_3–C NF electrode flexibility may be attractive for energy storage applications in wearable electronics or conformable batteries. Other metal fluorides may be similarly integrated into such flexible, free-standing electrode and nanoconfined within carbon using the proposed methodology. Similar methodology of nanoconfinement FeF_3 and other metal fluorides in carbon is also applicable for the formation of regular particles and slurry-based electrodes.

CHAPTER 6. STABILIZATION OF IRON (III) FLUORIDE VIA SHELL CONFINEMENT

Reproduced from **Advanced Energy Materials**, 2018, 1800721, E. Zhao, O. Borodin, X. Gao, D. Lei, Y. Xiao, X. Ren, W. Fu, A. Magasinski, K. Turcheniuk, G. Yushin, *Lithium-Iron (III) Fluoride Battery with Double Surface Protection*, Copyright (2018), with permission from WILEY-VCH Verlag GmbH & Co. KGaA, Weinheim. (See Appendix A for the permission letter)

Lithium-metal fluoride batteries promise significantly higher energy density than the state-of-the-art lithium-ion batteries and lithium-sulfur batteries. Unfortunately, commercialization of metal fluoride cathodes is prevented by their high resistance, irreversible structural change, and rapid degradation. This study demonstrates substantial boost in metal fluoride (MF) cathode stability by designing nanostructure with two layers of protective shell confinement – one deposited *ex-situ* and the other *in-situ*. Such methodology achieves over 90% capacity retention after 300 charge-discharge cycles, producing the first report on FeF_3 as a cathode material, where a very high capacity utilization in combination with excellent stability is approaching to the level needed for practical applications of FeF_3. The CEI containing lithium oxalate and B-F bond containing anions is found to effectively protect the cathode material from direct contact with electrolytes, thus greatly suppressing the dissolution of Fe. Mechanism study reveals that CEI is formed due to chemical and electrochemical decompositions. As a result, this work not only demonstrates unprecedented performances, but also provides the readers with a

better fundamental understanding of electrochemical behavior of MF cathodes and the positive impact observed with the application of a LiBoB salt in the electrolyte.

6.1 Introduction

FeF_3 is considered one of the most attractive due to the low cost and toxicity, abundance of Fe, the highest specific capacity of 712 mA h g^{-1} and high average potential of ~2.74 V,[92] offering an exceptionally high cell-level theoretical energy density in excess of 1500 W h L^{-1} (on a repeat unit basis) and cell-level specific energy in excess of 800 W h kg^{-1} (also on a repeat unit basis).[59]

Unfortunately, commercialization of FeF_3 is still prevented by multiple challenges. One major barrier is its notoriously poor electronic conductivity, resulting from the large band gap induced by strong ionicity of Fe-F and Li-F bonds.[93-94] Thus, large voltage hysteresis during charge-discharge is typically observed. Another barrier is the rapid degradation typically observed during cycling, induced by the significant volume change during the conversion reaction and the consequent mechanical failures, as well as the dissolution of FeF_3 triggered by free protons produced from undesired electrolyte decomposition or oxidation.[69, 84]

In order to address the two challenges above, recent endeavors have been devoted to intrinsic structure manipulation, such as open framwork strategy,[95] and design of various nanostructures, including high-energy ball milling,[96] coating with polymers,[76] HF-based aqueous solution synthesis,[70, 73] ionic liquid assisted synthesis,[97] pre-lithiation,[92] pulse laser deposition,[98] *etc*. But in spite of these efforts, the majority of previous works still showed limited capacity and fast decay in less than 50 cycles at room temperature. In some cases,

although FeF_3 was only discharged to 2.0 V at the current rate of 20 mA g^{-1}, utilizing 1/3 of the total capacity and undergoing one e^- reaction, it still failed to show stable cyclability after 30 cycles.[73, 76] In general, the dissolution issue of FeF_3 has not been properly addressed. To inhibit such detrimental reactions occurred at the interface of cathodes and electrolytes, two strategies are commonly utilized. One involves the introduction of inert surface coatings to prevent direct contact, such as carbon and metal oxide coatings.[83] However, the associated highly reductive atmospheres commonly required for chemical vapor deposition (CVD) or carbonization of hydrocarbon and organometallic precursors at elevated temperatures readily reduces FeF_3. Alternatively, effective design and selection of electrolyte additives become more attractive due to the *in situ* formation of the conformal Li^+ permeable cathode solid electrolyte interphase (CEI).[65, 84] The presence of this passivation shell confinement inhibits capacity loss during long-term cycling upon initial cell charge-discharge. LiBoB as an electrolyte additive has been extensively studied for intercalation cathode materials such as lithium manganese oxide (LMO), lithium nickel manganese oxide (NMO), *etc*. with high cutoff voltages due to the generation of a borate-rich stable passivating CEI on the surface of cathode.[99-101] Dual salt difluoro(oxalate) borate and $LiPF_6$-based electrolytes also showed improved capacity retention compared with single $LiPF_6$-based electrolytes for cells with the Li-excess layered oxide cathodes. However, the application of LiBoB for conversion materials still remains mostly unknown, which inspired us to explore the impact of LiBoB on the degradation of conversion cathode materials.

This research reports a holistic strategy to overcome the above limitations and improve the electrochemical performances of Li-FeF_3 cells by a novel design of the FeF_3

nanostructure (~20 nm), combined with a protective shell confinement surrounding the composite particles and careful electrolyte optimization. The rational architecture of uniform FeF_3-multiwalled carbon nanotube nanocomposites (FeF_3-CNTs) provides enhanced electronic conductivity and effectively accommodates the volume expansion during lithiation. This simple approach is applicable for the synthesis of a broad range of MFs and does not require the use of hazardous starting materials, such as HF. The use of uniform Al_2O_3 coatings produced by plasma-enhanced (PE) atomic layer deposition (ALD) at a low temperature in combination with the CEI induced by lithium bis(oxalato)borate (LiBoB) prevent the active material from undesirable direct contact with electrolytes. As a result, Li-FeF_3 cells cycled between 2-4.2 V (one e^- reaction) demonstrate remarkable performance characteristics, showing capacity of over 150 mA h g^{-1} at the current rate of 100 mA g^{-1} with a robust capacity retention of over 90% after 300 cycles. Post-mortem analyses provided insights on the mechanisms of the stability improvements by LiBoB additions to electrolyte. To my knowledge of published peer-reviewed publications, this is the first report on FeF_3 as a cathode material achieving 300 charge-discharge cycles. When compared with previously published work on FeF_3, the as-fabricated cells improve electrochemical stability for up to 10 times.

6.2 Experimental Methods

6.2.1 Synthesis of Fe-CNTs

First, 170 mg of MWCNTs (>90%, Research Nanomaterials, Inc., USA) and 150 mL of *N*-methyl-2-pyrrolidone (NMP, anhydrous, 99.5%, Sigma- Aldrich, USA) were mixed together to form a slurry. After 1 h of sonication, the slurry was blended with 1.039

g of $Fe(NO_3)_2 \cdot 9H_2O$ (99.99%; Sigma- Aldrich, USA) and magnetically stirred for 1 h. Then the slurry was refluxed in a 300-mL three-necked round-bottomed flask with continuous magnetic stirring for another 1 h. Reflux temperature was maintained at 180 °C by an oil bath. Next, the suspension was cooled down at room temperature, filtered (pore size of 2.5 μm; Whatman, USA), and washed with ethanol for 3 times. After drying at 80 °C overnight in a vacuum oven, the filtered solid composites were annealed under 4% H_2 in argon at 600 °C for 2 h.

6.2.2 Synthesis of FeF_3-CNTs

The as-prepared Fe-CNTs was contained in a metal crucible made of Inconel (made in house), followed by placing the crucible in the middle of an Inconel tube (made in-house) and flowing helium (Airgas, USA). After elevating the temperature to 300 ^oC at the rate of 4 ^oC min^{-1}, the flowing gas was switched from helium to a mixture gas of 2% NF_3 balanced with helium (Linde Gas Electronics, USA). The Fe-CNTs was fluorinated completely into FeF_3-CNTs after 2 h at 300 ^oC.

6.2.3 FeF_3-CNTs Electrode Fabrication

The active material (FeF_3-CNTs) powders were mixed with carbon black (Superior Graphite, USA), and PVDF (Alfa Aesar, USA) in NMP with a ratio of 80:10:10 by weight, stirred for 8 h then casted on an Al foil and dried in vacuum at 60 ^oC for 12 h. PEALD was performed using the Cambridge Fiji Plasma ALD system (Ultratech, CA). Alumina film was coated on the FeF_3-CNTs electrode using trimethylaluminium ($Al(CH_3)_3$) as a precursor and oxygen plasma at 120 ^oC for 60 cycles. The precursor pulse time was set to 0.06 s.

6.2.4 Materials Characterization

XRD patterns were collected using Cu Kα radiation at a voltage of 40 kV and a current of 20 mA on X'Pert PRO Alpha-1 (PANalytical, The Netherlands). SEM images and EDS elemental mapping were acquired by Hitachi SU8010 (Japan). HR-TEM images were collected on a Tecnai F30 (FEI, The Netherlands). Thermogravimetric analysis was performed on a Pyris 1 TGA. XPS was done using the Thermo K-Alpha system (Thermo Scientific, USA). NMR spectra were obtained using a Bruker AMX 400 (USA).

6.2.5 Electrochemical Measurements

Electrochemical characterization was carried out using type 2032 coin cells at room temperature. The cathode was FeF_3-CNTs electrode and the anode was pure lithium foil (99.9%, Alfa Aesar), separated by a piece of Celgard 2500 (Celgard, USA). As discussed above, a variety of electrolytes were studied. They all contained 0.7 M solute in a mixed solvent, ethyl carbonate, propyl carbonate and dimethyl carbonate (EC: PC: DMC= 1:1:3 in weight). $LiPF_6$, LiTFSI and LiBoB were used solely or hybrid as the solute. The EIS and cyclic voltammetry tests were carried out using a Gamry Reference 600 potentiostat (Gamry Instruments, Inc., USA). Galvanostatic charge−discharge tests were performed with an Arbin BT-2043 (Arbin Instruments, USA). All the specific capacity calculations involved in this work are based on the mass of FeF_3 active material only.

6.3 Results and Discussions

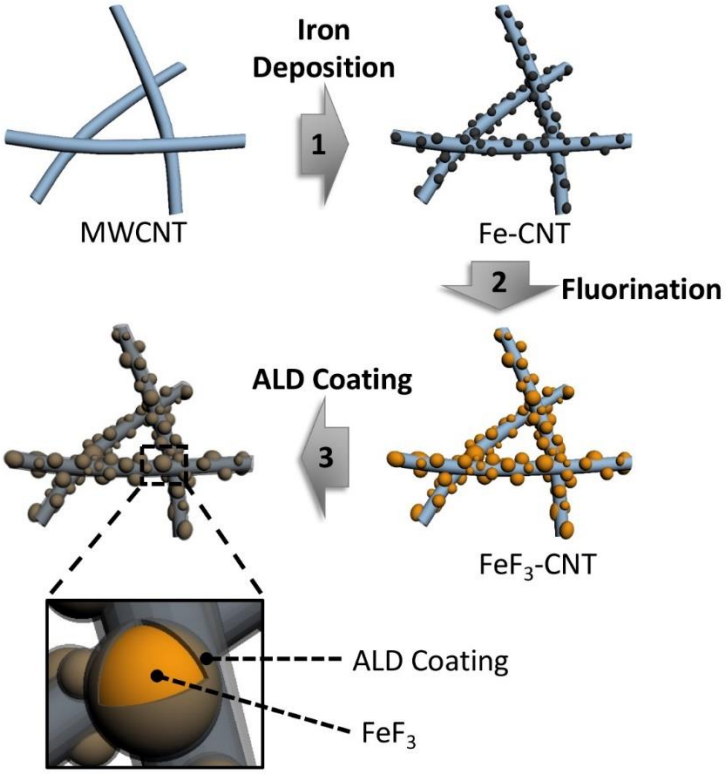

Figure 42. Schematic illustration of the synthesis of FeF_3-CNT nanocomposites: (1) iron nanoparticle deposition on MWCNT; (2) fluorination of Fe-CNT; (3) ALD coating of FeF_3-CNT.

The synthetic protocol for FeF_3-CNTs is schematically illustrated in Figure 42. As the first step, the low-cost and highly scalable solution-based synthesis of Fe-CNTs have been applied, as previously described by our group for alkaline batteries.[102] The as-prepared Fe-CNTs are then directly fluorinated under the flow of highly diluted NF_3 gas at a mild temperature, yielding the FeF_3-CNTs, which retained the uniform morphology of the Fe-CNTs.[103-105] I would like to highlight the great flexibility and safety that this approach offers. The design and synthesis of nanostructured metals have been extensively reported, however, the research on the nanoscale architecture of MFs still remains rare today. This methodology could be utilized for the fluorination of a broad range of MFs. This is very different from the conventional fluorination reactions based on aqueous HF

solution, which induce severe pulverization of metal (nano)particles. In addition, NF_3 is a low cost, widely used chemical commonly employed during dry etching process in semiconductor manufacturing. This solid-gas phase reaction is also operation-friendly and safe when diluted NF_3 is utilized (2% by weight mixed with an inert gas). It should also be clarified that the proposed procedure is general and could be utilized for diverse conductive carbon materials, such as graphene, porous carbon, carbon cloth, to name a few.

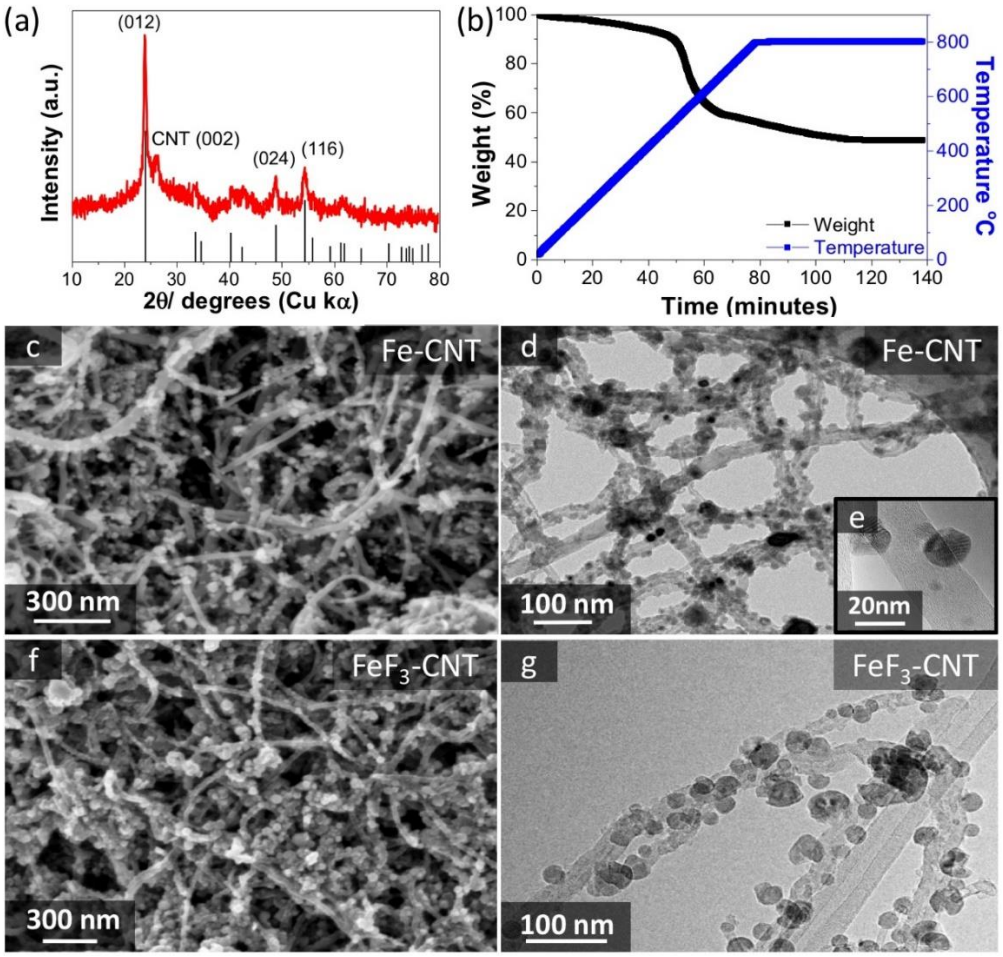

Figure 43. XRD patterns (a) and TGA curve at 10 $^oC\ min^{-1}$ in air (b) of FeF_3-CNT nanocomposites. SEM images of Fe-CNT (c) and FeF_3-CNT composites (f); TEM images of Fe-CNT (d, e) and FeF_3-CNT (g), showing uniform and consistent morphologies before and after fluorination.

Figure 43 presents the results of the selected characterizations. The X-ray diffraction (XRD) pattern of FeF_3-CNTs is shown in Figure 43a. The 2Θ peak at 26 ° originates from the presence of CNTs. All the other Bragg peaks can be ascribed to the hexagonal FeF_3 phase (JCPDS card no. 33-0647, space group *R3c*) without any significant content of impurities. In order to determine the content of FeF_3 and CNTs in the composites, thermogravimetric analysis (TGA) was conducted in air, as shown in Figure 43b. The weight loss observed at 550-600 ºC is corresponding to the burning of CNTs into CO and CO_2 gases and associated with the conversion of FeF_3 to iron oxide. According to the XRD patterns of the red-brown residue after TGA test (Figure 44), pure phase Fe_2O_3 is detected. Therefore, the weight of FeF_3 in initial composites could be calculated based on the remained mass of Fe_2O_3. In a result, the weight fraction of FeF_3 turns out to be 80 wt.% and may likely be further increased with further optimization.

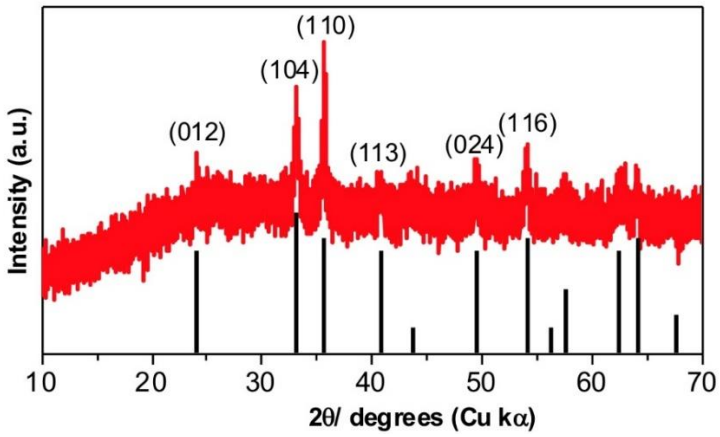

Figure 44. XRD patterns of the residue of FeF_3-CNT nanocomposites after TGA in air, showing pure phase of Fe_2O_3.

Once the FeF_3-CNTs electrode was fabricated, rapid PEALD of multiple metal oxides was performed in order to produce a protective shell surrounding the composites to

suppress the dissolution of FeF_3 during charge-discharge cycling. Relevant parameters were controlled to be optimal, according to a previous ALD study.[103-105] Among the candidates of coating materials, titanium oxide (TiO_2), aluminum oxide (Al_2O_3) and zirconium oxide (ZrO_2) are selected and compared because of their excellent Li^+ conductivity and good mechanical properties. The deposition procedures of all three coating materials were identical.

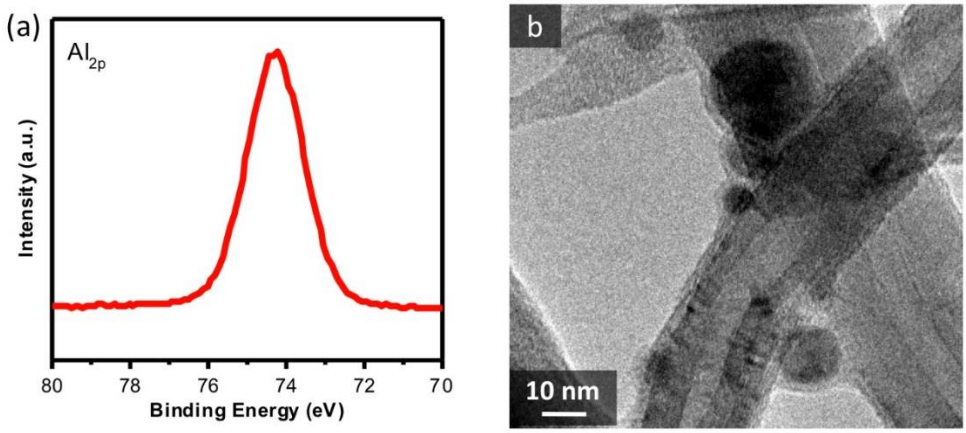

Figure 45. XPS spectrum of Al_{2p} (a) and HR-TEM image (b) of the fresh electrode after Al_2O_3 ALD.

The morphologies and microstructures of as-prepared Fe-CNTs and FeF_3-CNTs have been characterized by scanning electron microscopy (SEM) and high-resolution transmission electron microscopy (HR-TEM) studies. Figure 43c exhibits the SEM images of Fe particles with an average diameter of 15 nm uniformly deposited on the surface of MWCNTs, which is further confirmed by TEM images in Figure 43d and Figure 43e. After fluorination, as observed in Figure 43f and Figure 43g, the particle size of FeF_3 (~20 nm) becomes approximately twice as large as the initial Fe nanoparticles, meanwhile, every single FeF_3 particle remained attached to the MWCNTs. Such a composite morphology enables one to effectively accommodate the volume expansion during both fluorination

and electrochemical lithiation when discharge. The amount of the deposited metal oxides was below the detection limit of the analytical balance. Therefore, XPS spectrum of Al_{2p} was conducted and the strong peak at ~74.5 eV implies the existence of Al_2O_3, as shown in Figure 45a. High resolution TEM image of the composites (Figure 45b) after ALD clearly indicates a uniform coating with the thickness of ~2 nm.

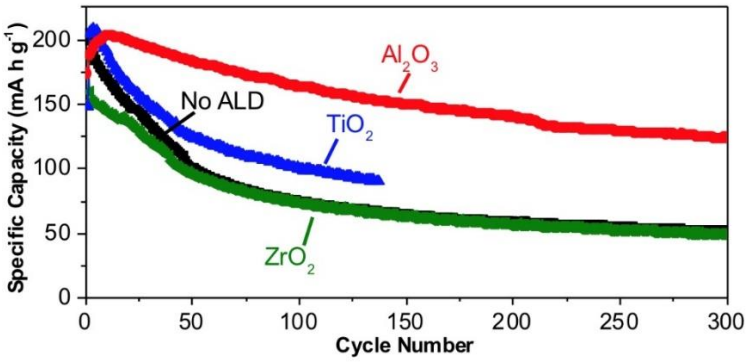

Figure 46. Electrochemical characterization of the FeF_3-CNT electrodes with different ALD coatings cycled at 100 mA g^{-1} using 0.7 M $LiPF_6$. Tester instrument error < 1%.

This work selects a limited voltage range of 2-4.2 V and allow only one e^- reaction to occur, in order to best understand the impacts of protective shells from ALD coating and CEI formation by diminishing the pulverization of FeF_3. Such a voltage range is also adopted by other groups working on FeF_3.[73, 76] First, the electrodes with different metal oxide coatings were compared in simple commercial electrolytes without additives (Figure 46). After 300 cycles at the current rate of 100 mA g^{-1}, the electrode coated by Al_2O_3 thin film appear to be the most robust. TiO_2 coating does modestly improve the cycling stability, while no improvement was also observed by using ZrO_2 coating. Thus, all the electrodes used in the following endeavors were pre-treated by Al_2O_3 ALD coating.

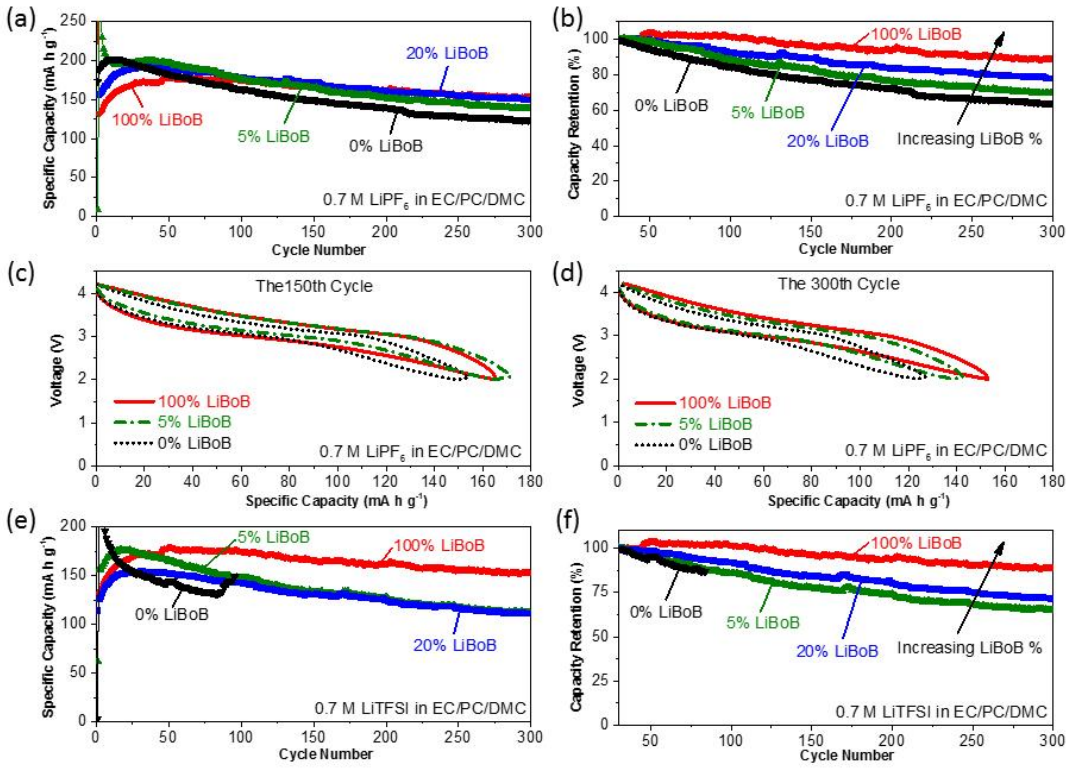

Figure 47. Electrochemical characterization of the half cells cycled at 100 mA g^{-1} using 0.7 M $LiPF_6$ with different percentages of LiBoB: cycling stability (a), capacity retention recorded from the 31st cycle (b), selected voltage-capacity profiles at the 150th cycle (c) and the 300th cycle (d). Additional cycling stability (e) and capacity retention (f) of the half cells using LiTFSI instead of $LiPF_6$ with all other conditions being the same. Tester instrument error < 1%.

In the next step, the carbonate-based electrolyte was modified to further improve cycling performance. After initial screening, LiBoB was identified a promising electrolyte additive, which has low solubility in a majority of common electrolyte solvents, but could be dissolved modestly in cyclic carbonates. In this work a commonly used EC/PC/DMC (1:1:3 wt.%) co-solvent system was applied and the molarity of Li^+ was fixed at a low level of 0.7 M to maintain the Li^+ concentration constant in all electrolytes (limited by the solubility of pure LiBOB in this solvent system).[106-108] As shown in Figure 47, charge-discharge (C-D) cycling stabilities of the cells containing $LiPF_6$ (Figure 47a-d) or lithium

bis(trifluoromethanesulfonyl)imide (LiTFSI) (Figure 47e, f) with different LiBoB percentages are compared at the current density of 100 mA g^{-1}. While the specific capacity of cells using $LiPF_6$-LiBoB system tends to be similar after 300 cycles (Figure 47a), increasing LiBoB additive percentage from 0%, 5% and 20% to 100% has a tremendous impact on capacity retention (Figure 47b) and coulombic efficiency (Figure 48). The 100% LiBoB without $LiPF_6$ or LiTFSI exhibited noticeably improved stability, achieving over 90% capacity retention after 300 cycles with 99.3% average coulombic efficiency. To my knowledge, such a stable performance of FeF_3 as a cathode material is unprecedented, particularly considering low electrolyte molarity. In fact, very few previously reported works reached more than 20-50 cycles with comparable capacity degradation. After observing the dramatic degradation of the cathode without any ALD coatings in 100% LiBoB (Figure 49), it can be concluded that such performance improvement is resulted from the synergy of Al_2O_3 coating and SEI layer.

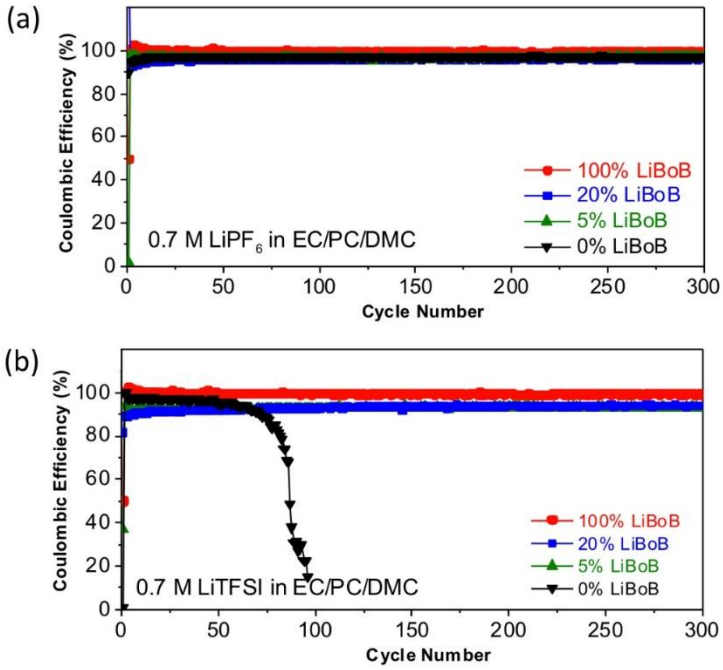

Figure 48. Coulombic efficiencies of the half cells cycled at 100 mA g^{-1} using 0.7 M $LiPF_6$ (a) and 0.7 M LiTFSI (b) in EC/PC/DMC with different percentages of LiBoB. Tester instrument error < 1%.

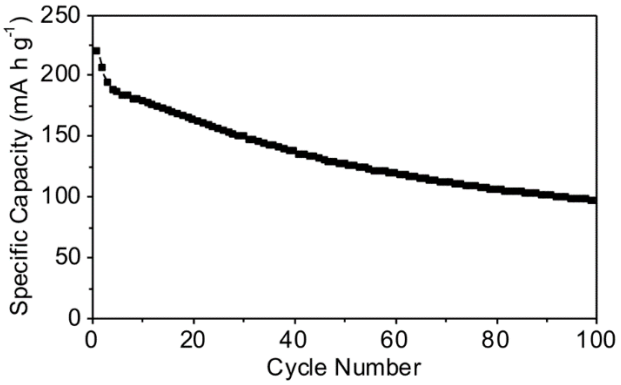

Figure 49. Electrochemical characterization of the cathode without any ALD coatings cycled at 100 mA g^{-1} using 0.7 M LiBoB (100%). Tester instrument error < 1%.

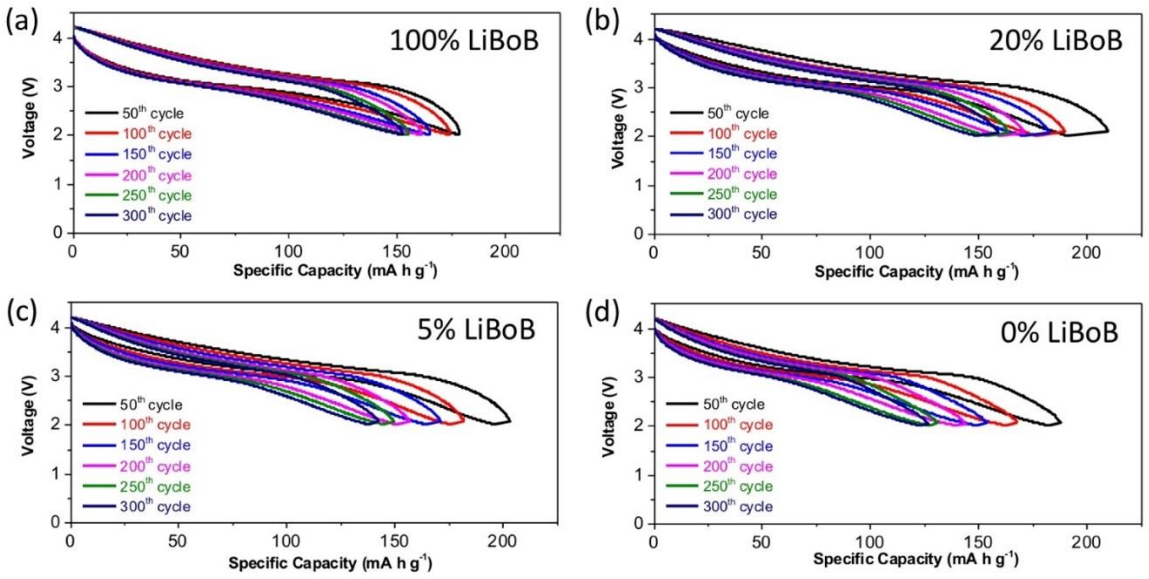

Figure 50. Voltage-capacity profiles of the half cells cycled at 100 mA g^{-1} using 0.7 M $LiPF_6$ with different percentages of LiBoB: (a) 100% LiBoB, (b) 20% LiBoB, (c) 5% LiBoB and (d) 0% LiBoB. Tester instrument error < 1%.

C-D profiles of the cells with different LiBoB percentages are plotted every 50 cycles in Figure 50. Regardless of the LiBoB concentration and the cycle number, all the cells showed a charge plateau at ~3.3 V and a discharge plateau at ~2.9 V, yielding a moderate hysteresis (the difference of discharge and charge voltages) of ~0.4 V. It is clearly revealed that the 100% LiBoB cell demonstrates highest coulombic efficiency (CE), close to 100%, while the cells with low and zero LiBoB contents have their lowest coulombic efficiencies in the first 50 cycles, which gradually increase during cycling, indicating that the Fe dissolution are more intensive at earlier stages. This is consistent with the degradation trend shown in Figure 47a-b and Figure 45. Capacity degradation is the most severe at the first 50 and 100 cycles and tends to be flattened afterwards. Figure 47c and 3d compare the charge-discharge profiles of cells with different LiBoB concentrations after 150 and 300 cycles, respectively. Given a certain cycle index, the cell with 100% LiBoB appears to have the largest hysteresis, while the cell without LiBoB has the smallest

hysteresis, implying growing impedance as the LiBoB ratio increases. To better understand the impact of LiBoB concentration on impedance, electrochemical impedance spectroscopies (EIS) of fresh (Figure 52) and cycled cells (Figure 54) of $LiPF_6$-LiBoB systems are contrasted as an example. Before cycling, higher LiBoB ratio consistently leads to higher charge transfer and electrode-electrolyte interface impedances, which matched with the fact that LiBoB has lower ionic conductivity than $LiPF_6$ and LiTFSI. However, the interface impedance significantly drops after 300 cycles and turned out to be lowest, suggesting a highly conductive layer of solid electrolyte interphase (SEI) has been formed during cycling.

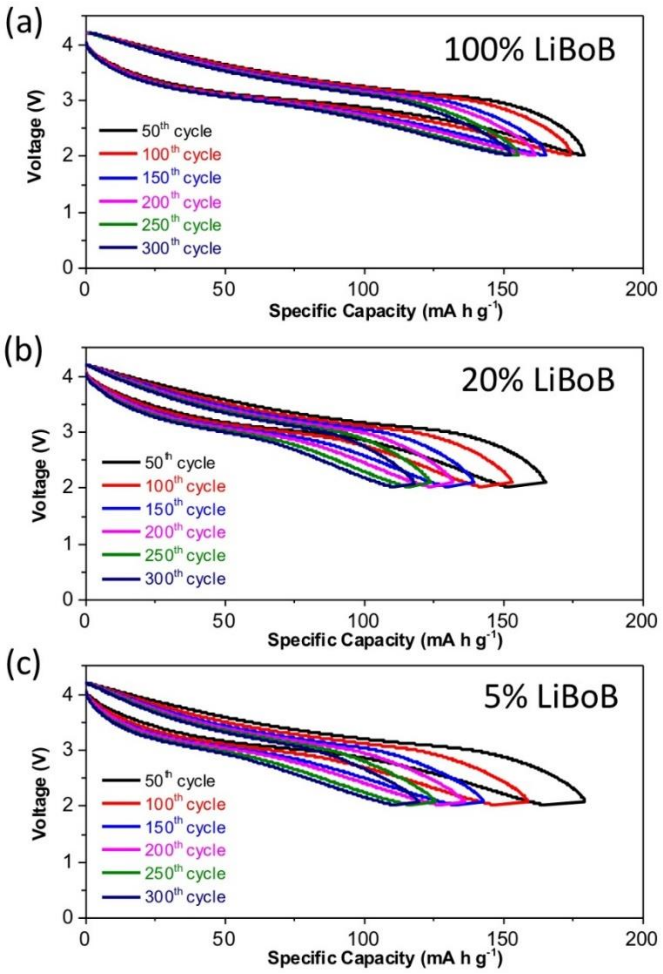

Figure 51. Voltage-capacity profiles of the half cells cycled at 100 mA g^{-1} using 0.7 M LiTFSI with different percentages of LiBoB: (a) 100% LiBoB, (b) 20% LiBoB and (c) 5% LiBoB. Tester instrument error < 1%.

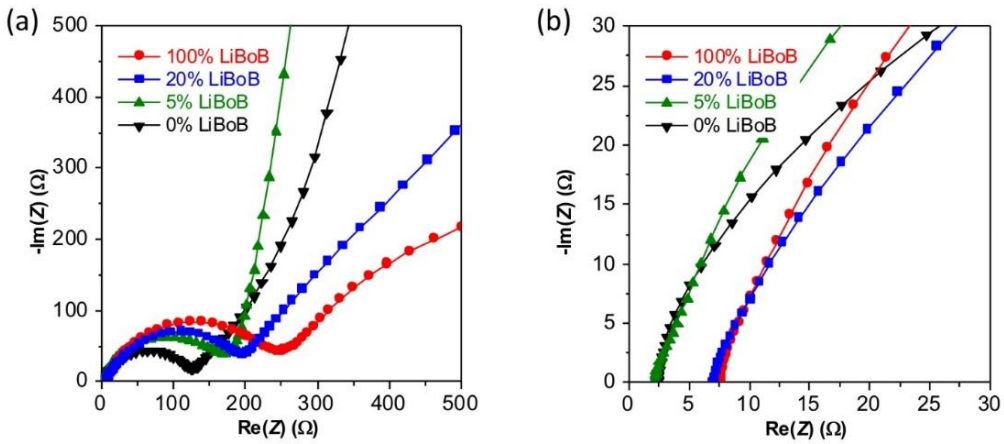

Figure 52. (a) Electrochemical impedance spectroscopy data of the fresh half cells using 0.7 M $LiPF_6$ with different percentages of LiBoB. (b) shows the magnified high-frequency region.

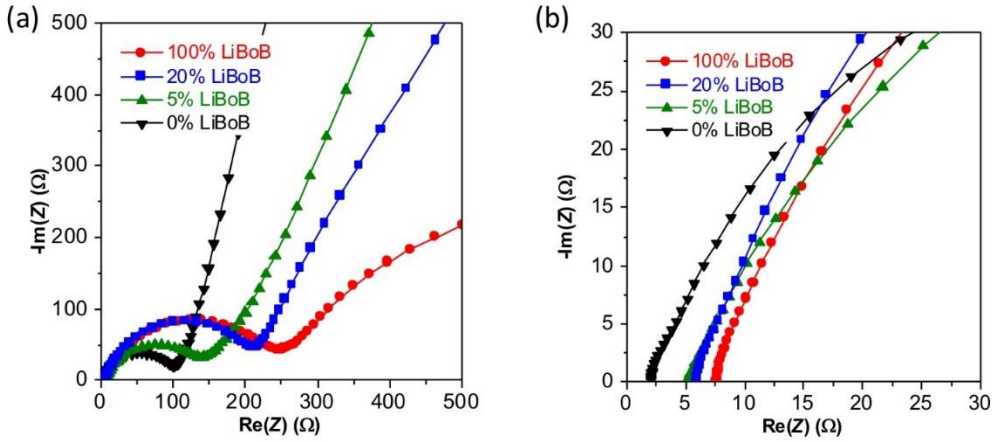

Figure 53. (a) Electrochemical impedance spectroscopy data of the fresh half cells using 0.7 M LiTFSI with different percentages of LiBoB. (b) shows the magnified high-frequency region.

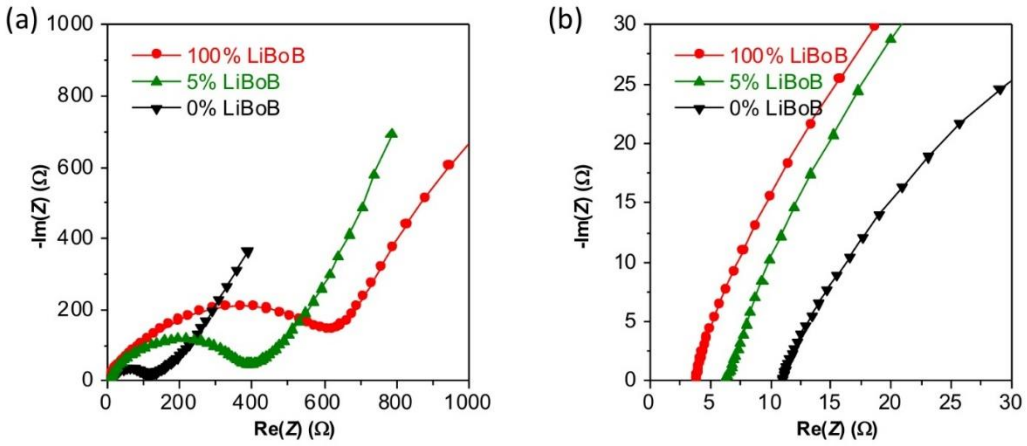

Figure 54. (a) Electrochemical impedance spectroscopy data of the half cells after 300 cycles using 0.7 M $LiPF_6$ with different percentages of LiBoB. (b) shows the magnified high-frequency region.

Additional comparisons are studied to examine the flexibility that LiBoB offers. Figure 47e-f show the charge-discharge cycling stabilities adopting LiTFSI-LiBoB system. The same trend as in $LiPF_6$-LiBoB system was also observed. Meanwhile, the charge-discharge profiles and EIS results of fresh cells are exhibited in Figure 51and Figure 53, supporting the statement concluded above. It is worth mentioning that the cell without LiBoB fails after ~70 cycles due to the electrode corrosion. This results manifests that the protection layer formed by LiBoB effectively prevents the corrosion and is instrumental for cell stability.

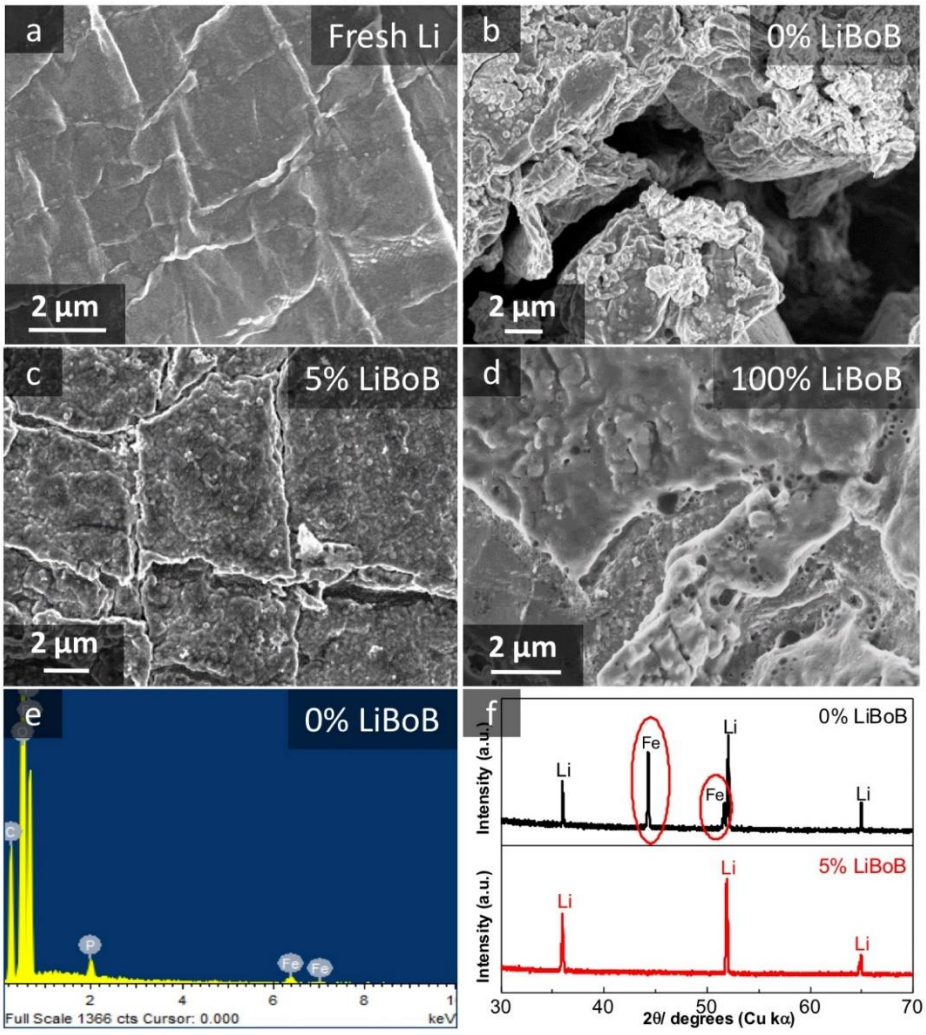

Figure 55. Characterization of the Li foils: (a) SEM micrograph of a fresh Li foil before cycling; (b)-(d) SEM images of Li anodes from selected half cells after 300 cycles using 0.7 M $LiPF_6$ with different percentages of LiBoB: (b) 0%, (c) 5% and (d) 100%; (e) EDS analysis of the Li anode as in (b); (f) comparison of the XRD patterns of the Li anodes as in (b) and (c).

Post-mortem studies of cycled Li foils reveal a dramatic impact of LiBoB on the morphologies. The fresh Li foil presents a smooth and flat surface as shown in Figure 55a, while cycled Li anode in the cell without LiBoB additive has uneven and rough surface with large cracks covered by deposited Fe particles, which is confirmed by EDX result (Figure 55e) and XRD patterns collected in Figure 55f. The formation of such a surface

layer resulting from Fe dissolution diminishes the cell-level capacity due to irreversible reactions and associated lack of active material on the cathode side. In sharp contrast, the Li foil anode cycled with 5% LiBoB (Figure 55c) has a visually much smoother surface of a SEI layer, while 100% LiBoB (Figure 55d) yielded the smoothest morphology of the anode SEI. No Fe was detected in the XRD patterns of the anode cycled (300 cycles) with the presence of LiBoB in electrolyte (Figure 55f), indicating that Fe dissolution was dramatically reduced.

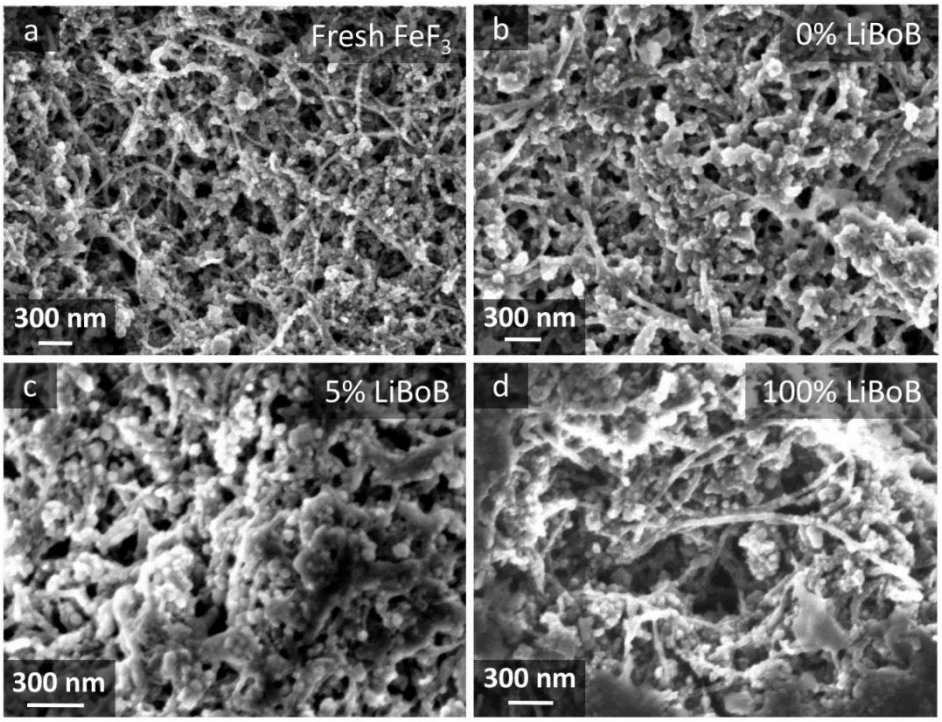

Figure 56. SEM images of (a) a fresh FeF_3-CNT cathode before cycling; and cycled cathodes from selected half cells after 300 cycles using 0.7 M $LiPF_6$ with different percentages of LiBoB: (b) 0%, (c) 5% and (d) 100%.

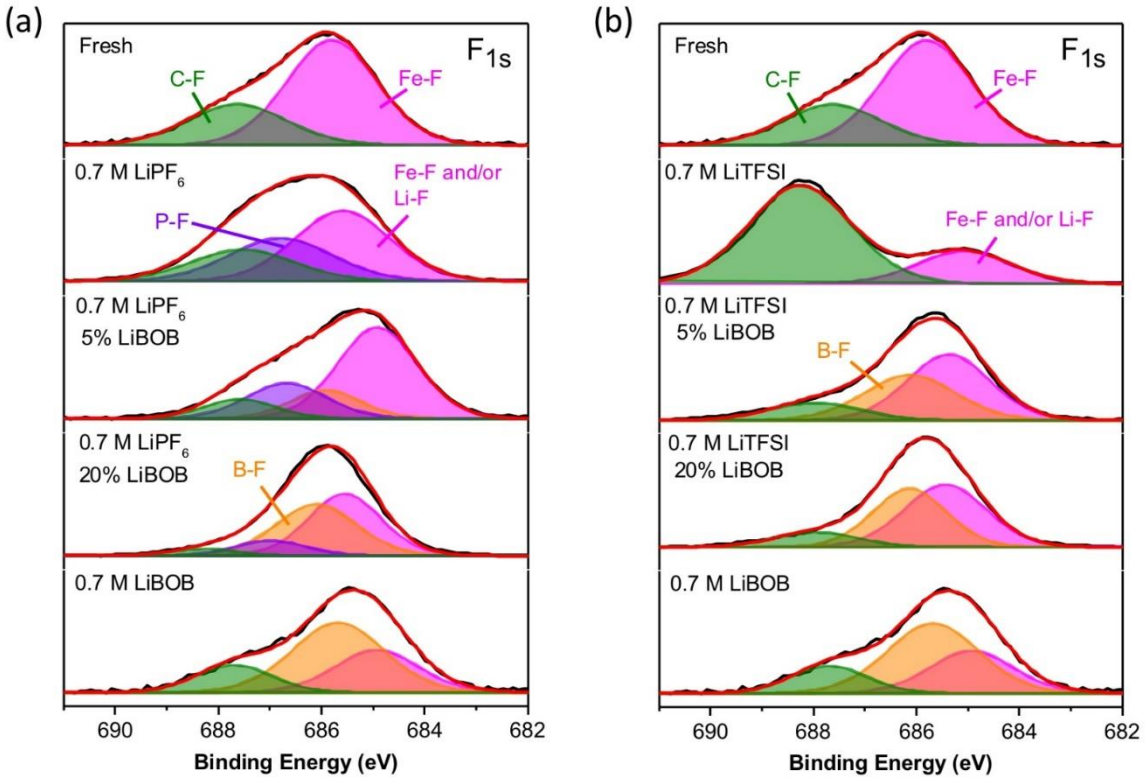

Figure 57. High-resolution XPS spectra for F_{1s} from FeF_3-CNT cathodes before and after cycling in 0.7 M $LiPF_6$ (a) and LiTFSI (b) with different percentages of LiBoB.

To clarify the impact of the LiBoB additive on the formation of the CEI on the cathode surfaces, SEM images of cycled cathodes are compared in Figure 56a and Figure 59 for LiBoB-$LiPF_6$ system, and Figure 60 for LiTFSI-LiBoB system. There are no major structural changes as the percentage of LiBoB increases, however, the morphologies become smoother due to the formation of CEI. To examine its chemical nature, X-ray photoelectron spectroscopies (XPS) of cycled cathodes were additionally studied. In $LiPF_6$-LiBoB system (Figure 57a), the major peak at 685-685.5 eV of the F_{1s} spectra in all samples is attributed to FeF_3 (fresh electrode) and/or LiF (cycled electrodes) as they have overlapped peak positions. The peak at 687.8-688.3 eV is assigned to C-F bonds from PVDF used as a binder and/or decomposed electrolyte solvent. For the cathodes cycled

with $LiPF_6$, P-F peak at 686.9 eV appears primarily due to the formed $Li_xPO_yF_z$ in the CEI, which is a common composition in $LiPF_6$-contained electrolytes as reported in previous publications.[99-100, 109-110] At the meantime, the rise of B-F peak at 685.9 eV is attributed to the generated $Li_xBO_yF_z$ species according to related LiBoB and LiDFOB study conducted before.[109-110] The B_{1s} spectra (Figure 61a) confirm the existence of boron and could be contributed to B-F and/or B-O bonds. Switching to LiTFSI-LiBoB system, similar results in Figure 57b for F_{1s} spectra and Figure 61b for B_{1s} spectra were observed. Interestingly, the cell containing merely LiTFSI without LiBoB has very different CEI nature from the others. This is consistent with a reported research previously.[83] Pure LiTFSI electrolyte could help to induce a CEI layer with heavy C-F content, as well as N and S rich decomposed salts (shown in Figure 62). While cycled cathodes with LiBoB additive don't have traceable N or S contained CEIs, demonstrating that LiBoB could effectively tune the chemical nature of CEI in the LiTFSI system. Therefore, LiBoB performs as an impactful substance on the CEI formation at a high voltage in both common electrolyte system based on $LiPF_6$ and LiTFSI salts.

Please notice that though Figure 57 is finally used in the publication, there's no unique peak fitting for XPS analysis. For example, the peaks could also be fitted more explicitly as shown in Figure 58. Fe(II)-F peak at 684.8 eV is added in Figure 58a to better align the peak position of Fe(III)-F bond across all samples. It is very possible to have the intermediate FeF_2 in the electrode, especially if the cell was dissected during charge-discharge. To my knowledge, in such environment, the most likely formed -F bond at a lower binding energy than Fe(III)-F would be Fe(II)-F. Same trend of B-F contents could be concluded as from Figure 57a. In the contrast, if the cell was dissected after fully

delithiation, no Fe(II)-F bond would be observed then. While in Figure 58b, N-F at 688.5 eV is a reasonable deduction in the cell with 0.7 M LiTFSI. The severe decomposition of electrolyte and electrode materials precipitated N-F heavy CEI, and finally caused the cell to fail. Again, B-F content follows the trend as LiBoB concentration increases.

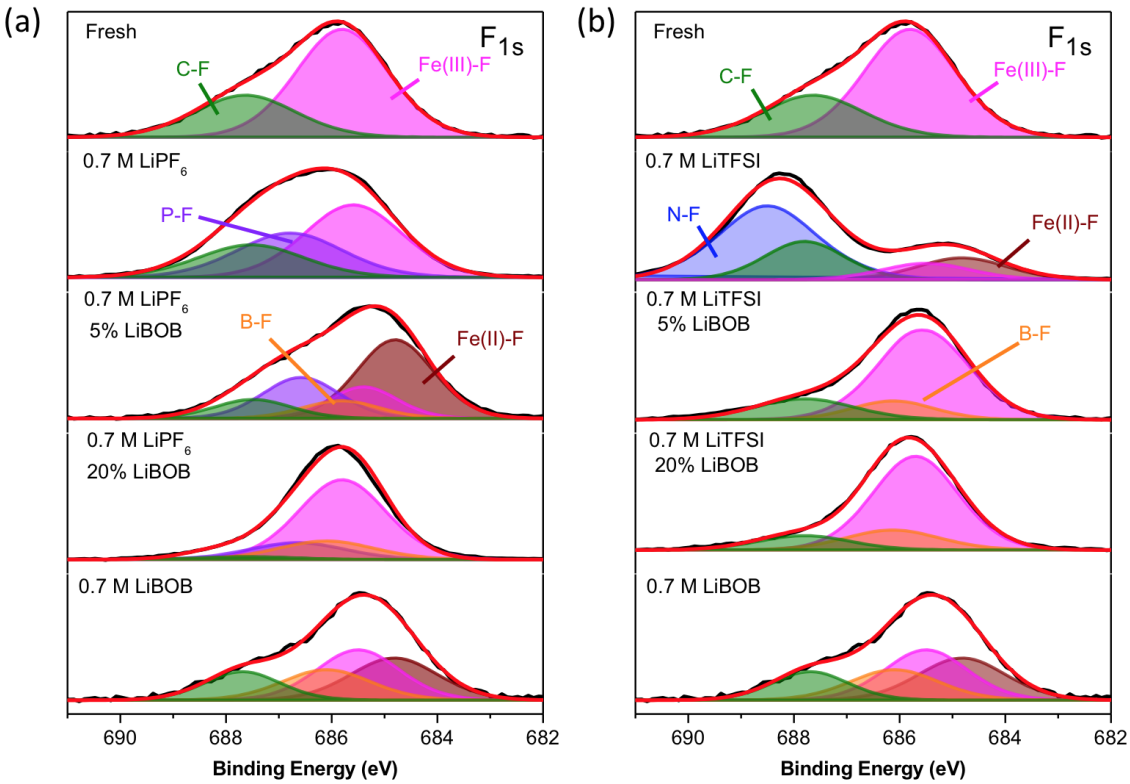

Figure 58. Alternative peak fitting to Figure 57.

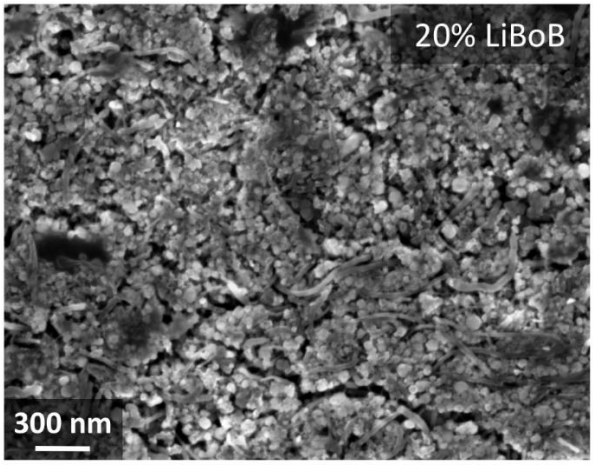

Figure 59. SEM image of cycled cathode in 0.7 M $LiPF_6$ with 20% LiBoB after 300 cycles.

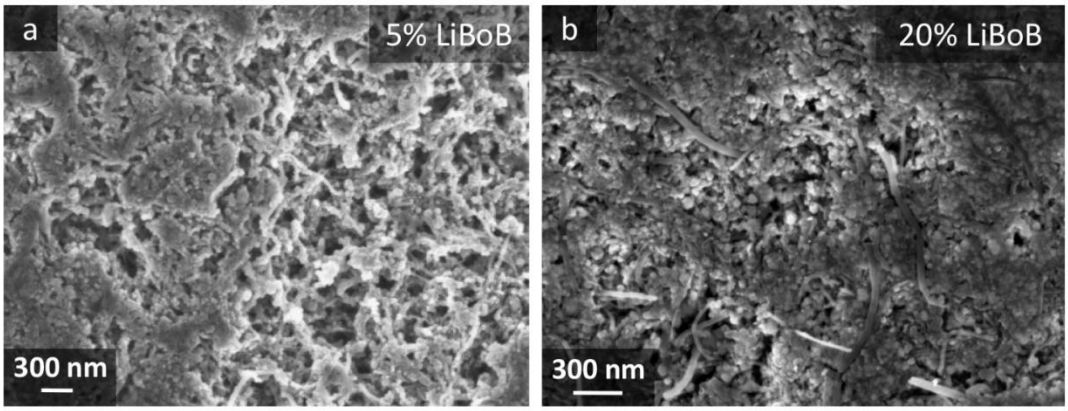

Figure 60. SEM images of cycled cathodes in 0.7 M LiTFSI with 5% LiBoB (a) and 20% LiBoB (b) after 300 cycles.

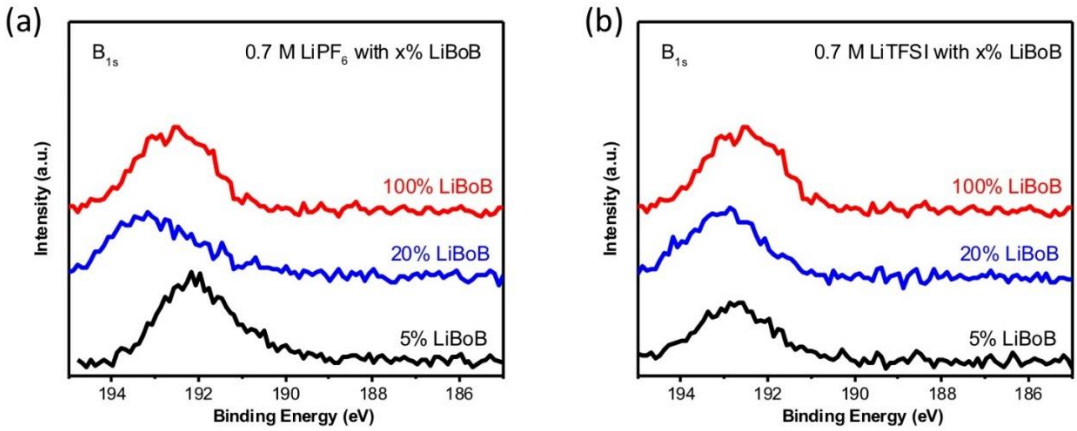

Figure 61. High-resolution XPS spectra for B_{1s} from FeF_3-CNT cathodes after cycling in 0.7 M $LiPF_6$ (a) and 0.7 M LiTFSI (b) with different percentages of LiBoB.

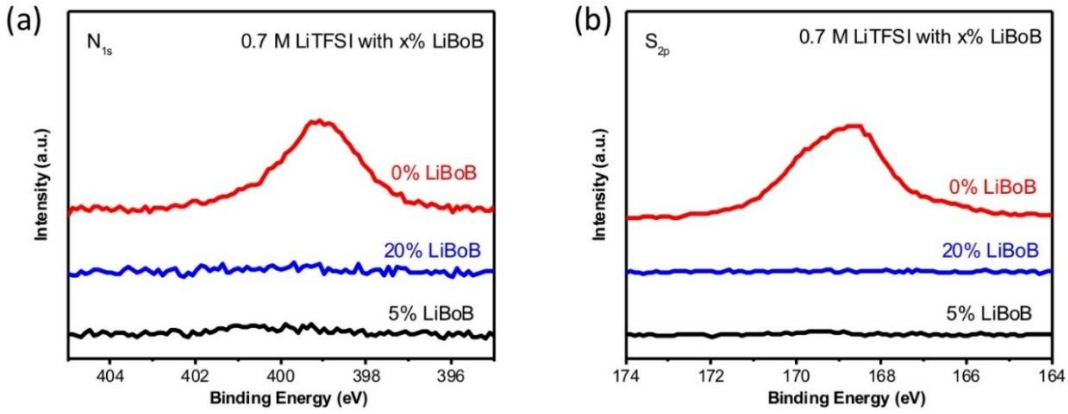

Figure 62. High-resolution XPS spectra for N_{1s} (a) and S_{2p} (b) from FeF_3-CNT cathodes after cycling in 0.7 M LiTFSI with different percentages of LiBoB.

Two mechanisms of CEI formation are proposed – chemical decomposition and/or electrochemical decomposition. First, to test the decomposition possibility via fluorination, *in-situ* NMR analysis of the reaction mixture was conducted after mixing 0.7 M LiBOB, 0.5 M LiF and 0.5 M FeF_3 in EC/PC/DMC and stirring at 85 °C for 120 hours. In ^{11}B NMR (Figure 63), $LiBF_4$ (-1.5 ppm) and LiDFOB (-2.7 ppm) showed up along with the initial LiBOB (-7.2ppm). According to ^{11}B NMR, the molar ratio of the LiBOB to $LiBF_4$/LiDFOB was calculated to be 5.74:1. These results are further corroborated by the ^{19}F NMR

spectrum (Figure 64). Two sets of signals at around -153.4 ppm and -154.1 ppm reveal, referring to the LiBOB decomposition products – $LiBF_4$ and LiDFOB, respectively. The coupling pattern of fluorine nuclei in ^{19}F NMR has been complicated with coupling peaks on both ^{11}B and ^{10}B nuclei due to the boron isotopes natural abundance. The integral intensity of the $LiBF_4$ as compared to the LiDFOB varies within the range 2.1-3.4 to 1 according to the ^{11}B and ^{19}F NMR. Remarkably, that the LiBOB also follows the decomposition route into $LiBF_4$ in the presence of FeF_3 with no LiF added, though no LiDFOB signal is seen. (Figure 65).

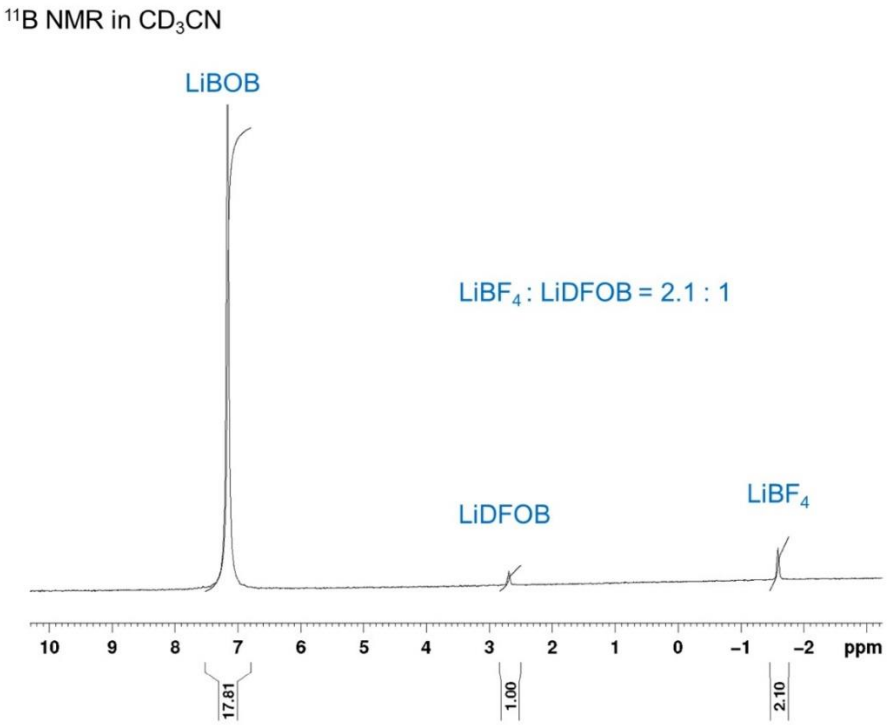

Figure 63. ^{11}B NMR of the reaction mixture (LiBOB, LiF, FeF_3 in EC/PC/DMC heated at 85 °C for 120 hours).

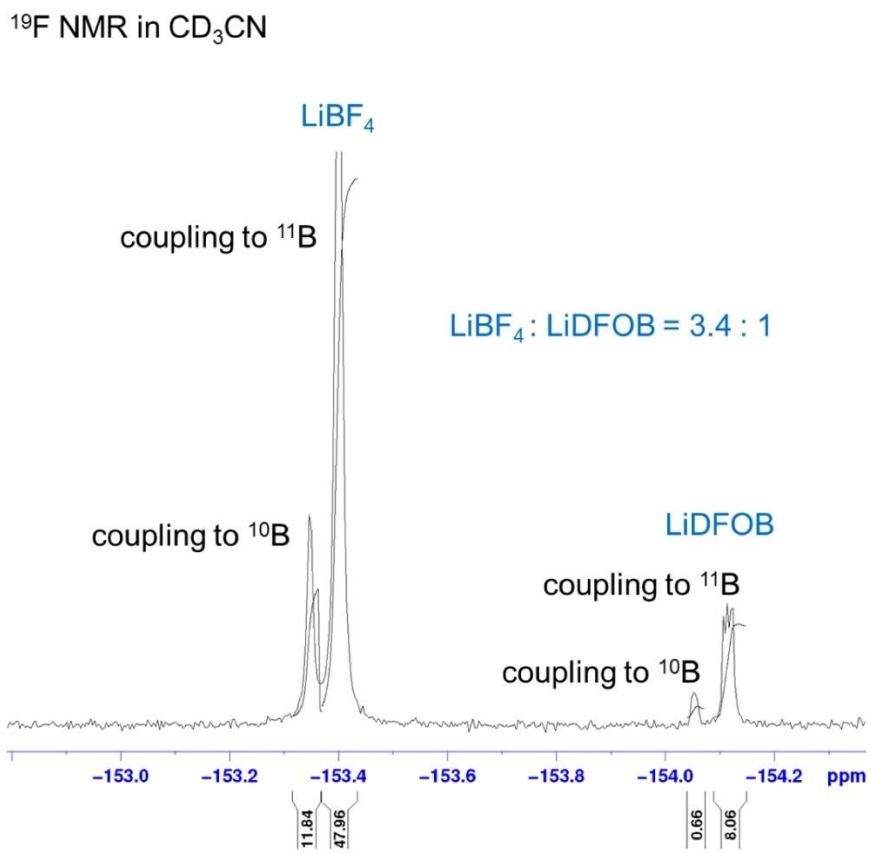

Figure 64. ^{19}F NMR of the reaction mixture (LiBOB, LiF, FeF_3 in EC/PC/DMC heated at 85 °C for 120 hours).

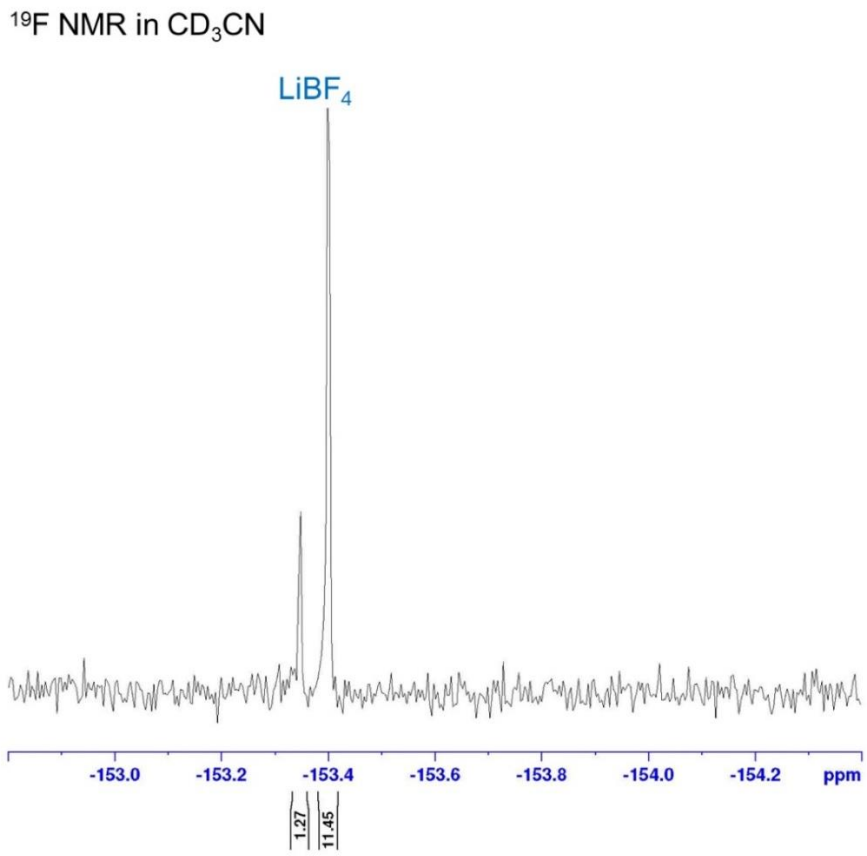

Figure 65. ^{19}F NMR of the reaction mixture (LiBOB, FeF_3 in EC/PC/DMC heated at 85 °C for 120 hours).

Therefore, the analyses of the spectra of the reaction mixture provide valuable insights about possible mechanism of the CEI formation, which is likely to occur through the decomposition of the LiBOB to $LiBF_4$ and LiDFOB in the presence of the F^-. The latter is likely to be given by LiF or FeF_3 because of their dissolution in the EC/PC/DMC mixture. F^- is a strong nucleophile, which attacks the BOB anion with the formation of the DFOB anion, which is then further fluorinated to the BF_4^- anion. Please note that $LiPF_6$ is not used, as it is a strong fluorination agent and can be readily decomposed with the formation of F^-, therefore facilitating the fluorination of LiBOB and the CEI formation. Therefore, the rate of the fluorination reaction can likely be increased in the presence of the large excess of F^-

, which is probably the case of chemical reaction in the real battery tests conditions. In the absence of LiF, the rate of the fluorination reaction is considerably slower (Figure 65). This can indicate the importance of the dissolved F^- presence to induce the LiBOB decomposition.

Moving forward, electrochemical decomposition has been studied next. A bare aluminum foil versus a Li counter electrode cell containing 0.7 M LiBoB and 0.5 M LiF (as a recourse of F) in EC/PC/DMC was tested for 300 charge-discharge cycles. Areal current density and voltage window were identical to those used in regular cells. Due to the lack of active materials, this test was completed in 2 hours, thus pure chemical decomposition was negligible. Post-mortem XPS analyses in Figure 66 demonstrated consistent chemical nature of the CEI. The peak of B-F bonding rises at 685.9 eV in the F_{1s} spectrum (Figure 66a) along with the peak at 193.5 eV in the B_{1s} spectrum (Figure 66b). Please note that no aluminum signals are detected in Al_{2p} spectrum (Figure 66c), suggesting that the CEI layer formed on Al is sufficiently thick. Therefore, electrochemical decomposition was found to play a key role in the CEI formation.

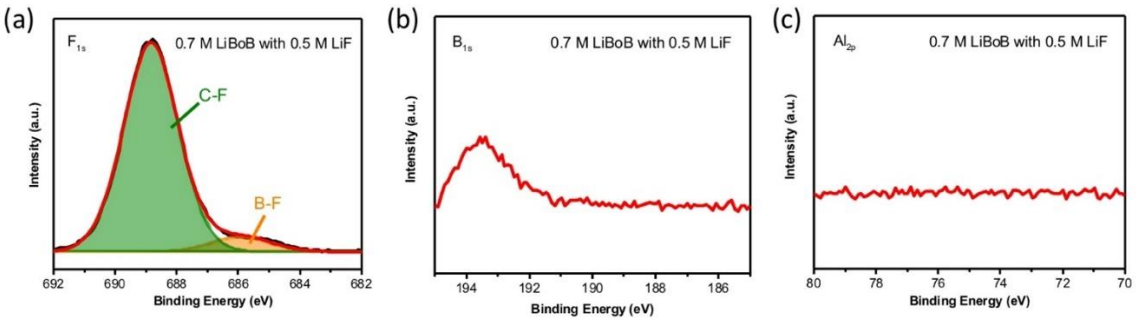

Figure 66. High-resolution XPS spectra for F_{1s} (a), B_{1s} (b) and Al_{2p} (c) from the bare aluminum foil after cycling versus Li anode in 0.7 M LiBoB.

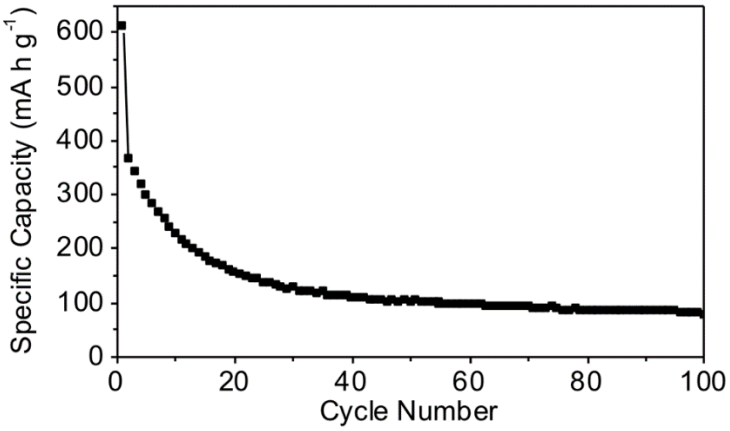

Figure 67. Electrochemical characterization of FeF_3-CNT electrode with Al_2O_3 ALD coating in 0.7 M LiBoB (100%) cycled at 100 mA g^{-1} between 1.2 V- 4.2 V, allowing the occurrence of both intercalation and conversion reactions. Tester instrument error < 1%.

Finally, for the sake of exploration, this study extends the voltage window to 1.2 V-4.2 V to allow the occurrence of both intercalation and conversion reactions ($3e^-$ reaction). Figure 67 shows the cycling performances of FeF_3-CNT cathode in 100% LiBoB. The initial specific capacity reached 620 mA h g^{-1}, however, it drops to ~100 mA h g^{-1} in 60 cycles, implying diminished protection, which may due to the destroying of protective SEI when discharged to a lower voltage. Further study of cyclic stability of the $3e^-$ reaction of FeF_3 and its SEI protection are out of the scope of this work but will be covered in the future.

6.4 Conclusions

In summary, the efforts to develop a commercially viable cathode technology based on low-cost and extremely abundant Fe revealed multiple important observations. First, this work has demonstrated an efficient approach to improving the electrochemical performances of Li-FeF_3 cells by the introduction of a novel nanostructure of electrically

connected FeF_3-CNT network, further comprising two layers of protective shell confinement – one deposited *ex-situ* and another one *in-situ*. This proposed synthesis pathway is broadly applicable for a wide range of MFs, and is advantageous due to a minimal use of hazardous materials, such as HF. The first protection shell, uniform Al_2O_3 coating, produced by PEALD, significantly improved the capacity retention of FeF_3. The second level of surface protection, *in-situ* formed CEI, induced both chemically and electrochemically by LiBoB additive in electrolytes, successfully elevated the capacity retention of Li-FeF_3 cells to over 90% after 300 cycles. The combination of these approaches allowed us produce the first report on FeF_3 as a cathode material, where a very high capacity utilization in combination with excellent stability is approaching to the level needed for practical applications of FeF_3. The CEI containing lithium oxalate and B-F bond contained anions was found to effectively protect the cathode material from direct contact with electrolytes, thus greatly suppressing the dissolution of Fe. Compared with open literature reports on FeF_3, this work not only demonstrated up to 10 time higher electrochemical stability, but also provided the readers with a better fundamental understanding of electrochemical behavior of MF cathodes above 2 V and the positive impact observed with the application of a LiBoB salt in the electrolyte.

CHAPTER 7. CONCLUSIONS AND RECOMMENDATIONS

7.1 Conclusions

In this thesis, the nanoconfinement of selected metal oxides and metal fluorides for energy storage applications has been systematically investigated, from synthesis, characterization, to structure-property relationships, and methodology optimization. Additionally, the CEI surface layer formation mechanisms and its impacts on electrochemical performances have also been studied and discussed.

Specifically, I demonstrated that uniform composites can be synthesized by infiltration or electrospinning to embed precursors into nanoporous carbons, which serve as nucleation sites for the formation of precursor particles from the solution. Under optimal parameters, heat-treatment, coupling with hydrothermal reactions if needed, it is possible to convert precursor nanoparticles to active material nanoparticles (herein, LTO, TiO_2, MnO, NiO, Cu_2O and FeF_3) without changing the morphology of the composites. The process variables (e.g. carbon porosity in case of infiltration and carbonization temperature in case of electrospan precursor carbonization) have profound effects on both the morphology and the electrochemical properties. I identified the nanoconfinement can overcome some limitations of common electrode materials, including poor electronic and ionic conductivities, volume changes, phase separation and particle aggregation. For example, the LTO-AC sample in Chapter 3 showed more than 100 mA h g^{-1} at the rate of over 60 A g^{-1}, where charge or discharge takes place in only 6 s. This is 12 times higher gravimetric and volumetric capacities than pure AC. The FeF_3-C nanofibers in Chapter 5

demonstrated over 500 mAh g^{-1} after 400 cycles, which is significantly superior to previously reports.

CEI properties can be controlled and tuned by electrolyte optimization, and the favorable CEI may play a key role to significantly reduce or prevent transition metal dissolution. In Chapter 6, CEI improved the capacity retention of Li-FeF_3 cells to over 90% after 300 cycles, which is almost an order of magnitude better than what was previously described in the open literature for FeF_3. Chapter 6 also presented experimental evidence of CEI formation mechanisms, suggesting both chemical and electrochemical decompositions of electrode and electrolyte materials were taking place and likely contributed to CEI composition and properties.

7.2 Recommendations

I would like to highlight three interesting directions for possible future research from my personal view:

1. The nanoconfinement of lithium transition metal oxides as cathode materials, such as $LiMn_2O_4$, $LiNi_{0.5}Mn_{0.5}O_2$, $LiNi_xMn_yCo_zO_2$ to improve electronic conductivity and electrochemical reversibility. These are among the promising candidate materials for use in LIBs. They contain transition metals at highly oxidative states, meanwhile require good crystal structures for high capacity utilization and high stability. Their compatibility with the conductive and reductive templates may be very challenging though. Conversion-type cathodes widely adopted in practical applications may become attractive later.

2. The modeling (for precursor and process selection), scalability and automation of nanoconfinement technique may be important for practical applications of this approach and should be explored.
3. The applications of nanoconfinement beyond energy storage materials may become interesting as well. It may serve as a promising technique for photovoltaics, semiconductors, catalysis, medical applications, among others. Transparent materials, silicon, porous polymers may be able to substitute porous carbon depending on the application requirements.

APPENDIX A. PERMISSION LETTERS FOR THE REUSE OF COPYRIGHTED MATERIALS

(Start from the next page)

Figure 3 and Figure 4

ELSEVIER LICENSE
TERMS AND CONDITIONS

Aug 07, 2018

This Agreement between Georgia Institute of Technology -- Enbo Zhao ("You") and Elsevier ("Elsevier") consists of your license details and the terms and conditions provided by Elsevier and Copyright Clearance Center.

License Number	4403730735505
License date	Aug 07, 2018
Licensed Content Publisher	Elsevier
Licensed Content Publication	Materials Today
Licensed Content Title	Li-ion battery materials: present and future
Licensed Content Author	Naoki Nitta,Feixiang Wu,Jung Tae Lee,Gleb Yushin
Licensed Content Date	Jun 1, 2015
Licensed Content Volume	18
Licensed Content Issue	5
Licensed Content Pages	13
Start Page	252
End Page	264
Type of Use	reuse in a thesis/dissertation
Intended publisher of new work	other
Portion	figures/tables/illustrations
Number of figures/tables/illustrations	2
Format	electronic
Are you the author of this Elsevier article?	No
Will you be translating?	No
Original figure numbers	Figure 1, Figure 2.
Title of your thesis/dissertation	THE NANOCONFINEMENT OF LITHIUM TITANATE, TITANIUM OXIDE, IRON FLUORIDE AND OTHERS IN CARBON FOR ENERGY STORAGE APPLICATIONS
Expected completion date	Aug 2018
Estimated size (number of pages)	150
Requestor Location	Georgia Institute of Technology 631 Cherry St NW ATLANTA, GA 30313 United States Attn: Georgia Institute of Technology
Publisher Tax ID	98-0397604
Total	0.00 USD

Figure 5 and Figure 7

JOHN WILEY AND SONS LICENSE TERMS AND CONDITIONS

Aug 07, 2018

This Agreement between Georgia Institute of Technology -- Enbo Zhao ("You") and John Wiley and Sons ("John Wiley and Sons") consists of your license details and the terms and conditions provided by John Wiley and Sons and Copyright Clearance Center.

License Number	4403721130043
License date	Aug 07, 2018
Licensed Content Publisher	John Wiley and Sons
Licensed Content Publication	Wiley Books
Licensed Content Title	Electrical Energy Storage: Supercapacitors
Licensed Content Author	Enbo Zhao, Wentian Gu, Gleb Yushin
Licensed Content Date	Aug 9, 2017
Licensed Content Pages	36
Type of use	Dissertation/Thesis
Requestor type	University/Academic
Format	Electronic
Portion	Figure/table
Number of figures/tables	2
Original Wiley figure/table number(s)	Figure 9, Figure 14.
Will you be translating?	No
Title of your thesis / dissertation	THE NANOCONFINEMENT OF LITHIUM TITANATE, TITANIUM OXIDE, IRON FLUORIDE AND OTHERS IN CARBON FOR ENERGY STORAGE APPLICATIONS
Expected completion date	Aug 2018
Expected size (number of pages)	150
Requestor Location	Georgia Institute of Technology 631 Cherry St NW ATLANTA, GA 30313 United States Attn: Georgia Institute of Technology
Publisher Tax ID	EU826007151
Total	0.00 USD
Terms and Conditions	

TERMS AND CONDITIONS

This copyrighted material is owned by or exclusively licensed to John Wiley & Sons, Inc. or one of its group companies (each a"Wiley Company") or handled on behalf of a society with which a Wiley Company has exclusive publishing rights in relation to a particular work (collectively "WILEY"). By clicking "accept" in connection with completing this licensing transaction, you agree that the following terms and conditions apply to this transaction

Figure 6

JOHN WILEY AND SONS LICENSE TERMS AND CONDITIONS

Aug 07, 2018

This Agreement between Georgia Institute of Technology -- Enbo Zhao ("You") and John Wiley and Sons ("John Wiley and Sons") consists of your license details and the terms and conditions provided by John Wiley and Sons and Copyright Clearance Center.

License Number	4403720790717
License date	Aug 07, 2018
Licensed Content Publisher	John Wiley and Sons
Licensed Content Publication	ChemElectroChem
Licensed Content Title	High-Performance Hybrid Supercapacitor Based on Graphene-Wrapped Li4Ti5O12 and Activated Carbon
Licensed Content Author	Haegyeom Kim,Kyu-Young Park,Min-Young Cho,Mok-Hwa Kim,Jihyun Hong,Sung-Kyun Jung,Kwang Chul Roh,Kisuk Kang
Licensed Content Date	Dec 13, 2013
Licensed Content Pages	6
Type of use	Dissertation/Thesis
Requestor type	University/Academic
Format	Electronic
Portion	Figure/table
Number of figures/tables	1
Original Wiley figure/table number(s)	Figure 1
Will you be translating?	No
Title of your thesis / dissertation	THE NANOCONFINEMENT OF LITHIUM TITANATE, TITANIUM OXIDE, IRON FLUORIDE AND OTHERS IN CARBON FOR ENERGY STORAGE APPLICATIONS
Expected completion date	Aug 2018
Expected size (number of pages)	150
Requestor Location	Georgia Institute of Technology 631 Cherry St NW ATLANTA, GA 30313 United States Attn: Georgia Institute of Technology
Publisher Tax ID	EU826007151
Total	0.00 USD
Terms and Conditions	

TERMS AND CONDITIONS

This copyrighted material is owned by or exclusively licensed to John Wiley & Sons, Inc. or one of its group companies (each a"Wiley Company") or handled on behalf of a society with which a Wiley Company has exclusive publishing rights in relation to a particular work

Figure 8

ELSEVIER LICENSE
TERMS AND CONDITIONS

Aug 07, 2018

This Agreement between Georgia Institute of Technology -- Enbo Zhao ("You") and Elsevier ("Elsevier") consists of your license details and the terms and conditions provided by Elsevier and Copyright Clearance Center.

License Number	4403731021566
License date	Aug 07, 2018
Licensed Content Publisher	Elsevier
Licensed Content Publication	Journal of Fluorine Chemistry
Licensed Content Title	Fluoride based electrode materials for advanced energy storage devices
Licensed Content Author	Glenn G. Amatucci,Nathalie Pereira
Licensed Content Date	Apr 1, 2007
Licensed Content Volume	128
Licensed Content Issue	4
Licensed Content Pages	20
Start Page	243
End Page	262
Type of Use	reuse in a thesis/dissertation
Intended publisher of new work	other
Portion	figures/tables/illustrations
Number of figures/tables/illustrations	1
Format	electronic
Are you the author of this Elsevier article?	No
Will you be translating?	No
Original figure numbers	Figure 17
Title of your thesis/dissertation	THE NANOCONFINEMENT OF LITHIUM TITANATE, TITANIUM OXIDE, IRON FLUORIDE AND OTHERS IN CARBON FOR ENERGY STORAGE APPLICATIONS
Expected completion date	Aug 2018
Estimated size (number of pages)	150
Requestor Location	Georgia Institute of Technology 631 Cherry St NW ATLANTA, GA 30313 United States Attn: Georgia Institute of Technology
Publisher Tax ID	98-0397604

Chapter 3

Dear Dr.Zhao,

Thank you for contacting ACS Publications Support.

Your permission request is granted and there is no fee for this reuse. In your planned reuse, you must cite the ACS article as the source, add this direct link https://pubs.acs.org/doi/abs/10.1021/acsnano.6b00479 , and include a notice to readers that further permissions related to the material excerpted should be directed to the ACS.

If you need further assistance, please let me know.

Sincerely,

Ashley Gibson

ACS Publications

Customer Services & Information

Website: https://help.acs.org

Chapter 5

JOHN WILEY AND SONS LICENSE TERMS AND CONDITIONS

Aug 07, 2018

This Agreement between Georgia Institute of Technology -- Enbo Zhao ("You") and John Wiley and Sons ("John Wiley and Sons") consists of your license details and the terms and conditions provided by John Wiley and Sons and Copyright Clearance Center.

License Number	4403701118590
License date	Aug 07, 2018
Licensed Content Publisher	John Wiley and Sons
Licensed Content Publication	Advanced Functional Materials
Licensed Content Title	Iron Fluoride–Carbon Nanocomposite Nanofibers as Free-Standing Cathodes for High-Energy Lithium Batteries
Licensed Content Date	Jun 21, 2018
Licensed Content Pages	1
Type of use	Dissertation/Thesis
Requestor type	Author of this Wiley article
Format	Electronic
Portion	Full article
Will you be translating?	No
Title of your thesis / dissertation	THE NANOCONFINEMENT OF LITHIUM TITANATE, TITANIUM OXIDE, IRON FLUORIDE AND OTHERS IN CARBON FOR ENERGY STORAGE APPLICATIONS
Expected completion date	Aug 2018
Expected size (number of pages)	150
Requestor Location	Georgia Institute of Technology 631 Cherry St NW ATLANTA, GA 30313 United States Attn: Georgia Institute of Technology
Publisher Tax ID	EU826007151
Total	0.00 USD
Terms and Conditions	

TERMS AND CONDITIONS

This copyrighted material is owned by or exclusively licensed to John Wiley & Sons, Inc. or one of its group companies (each a"Wiley Company") or handled on behalf of a society with which a Wiley Company has exclusive publishing rights in relation to a particular work (collectively "WILEY"). By clicking "accept" in connection with completing this licensing transaction, you agree that the following terms and conditions apply to this transaction (along with the billing and payment terms and conditions established by the Copyright Clearance Center Inc., ("CCC's Billing and Payment terms and conditions"), at the time that you opened your RightsLink account (these are available at any time at http://myaccount.copyright.com).

Chapter 6

JOHN WILEY AND SONS LICENSE TERMS AND CONDITIONS

Aug 07, 2018

This Agreement between Georgia Institute of Technology -- Enbo Zhao ("You") and John Wiley and Sons ("John Wiley and Sons") consists of your license details and the terms and conditions provided by John Wiley and Sons and Copyright Clearance Center.

License Number	4403720308348
License date	Aug 07, 2018
Licensed Content Publisher	John Wiley and Sons
Licensed Content Publication	Advanced Energy Materials
Licensed Content Title	Lithium–Iron (III) Fluoride Battery with Double Surface Protection
Licensed Content Date	Jul 18, 2018
Licensed Content Pages	1
Type of use	Dissertation/Thesis
Requestor type	Author of this Wiley article
Format	Electronic
Portion	Full article
Will you be translating?	No
Title of your thesis / dissertation	THE NANOCONFINEMENT OF LITHIUM TITANATE, TITANIUM OXIDE, IRON FLUORIDE AND OTHERS IN CARBON FOR ENERGY STORAGE APPLICATIONS
Expected completion date	Aug 2018
Expected size (number of pages)	150
Requestor Location	Georgia Institute of Technology 631 Cherry St NW ATLANTA, GA 30313 United States Attn: Georgia Institute of Technology
Publisher Tax ID	EU826007151
Total	0.00 USD
Terms and Conditions	

TERMS AND CONDITIONS

This copyrighted material is owned by or exclusively licensed to John Wiley & Sons, Inc. or one of its group companies (each a"Wiley Company") or handled on behalf of a society with which a Wiley Company has exclusive publishing rights in relation to a particular work (collectively "WILEY"). By clicking "accept" in connection with completing this licensing transaction, you agree that the following terms and conditions apply to this transaction (along with the billing and payment terms and conditions established by the Copyright Clearance Center Inc., ("CCC's Billing and Payment terms and conditions"), at the time that you opened your RightsLink account (these are available at any time at http://myaccount.copyright.com).

REFERENCES

1. Nitta, N.; Wu, F. X.; Lee, J. T.; Yushin, G., Li-Ion Battery Materials: Present and Future. *Materials Today* **2015,** *18* (5), 252-264.

2. Lee, J. T.; Zhao, Y.; Thieme, S.; Kim, H.; Oschatz, M.; Borchardt, L.; Magasinski, A.; Cho, W.-I.; Kaskel, S.; Yushin, G., Sulfur-Infiltrated Micro- and Mesoporous Silicon Carbide-Derived Carbon Cathode for High-Performance Lithium Sulfur Batteries. *Advanced Materials* **2013,** *25* (33), 4573-4579.

3. Roy, P.; Srivastava, S. K., Nanostructured Anode Materials for Lithium Ion Batteries. *Journal of Materials Chemistry A* **2015,** *3* (6), 2454-2484.

4. Krause, L. J.; Lamanna, W.; Summerfield, J.; Engle, M.; Korba, G.; Loch, R.; Atanasoski, R., Corrosion of Aluminum at High Voltages in Non-Aqueous Electrolytes Containing Perfluoroalkylsulfonyl Imides; New Lithium Salts for Lithium-Ion Cells. *Journal of Power Sources* **1997,** *68* (2), 320-325.

5. Xu, K., Nonaqueous Liquid Electrolytes for Lithium-Based Rechargeable Batteries. *Chemical Reviews* **2004,** *104* (10), 4303-4417.

6. Rodríguez, A.; Canosa, J.; Domínguez, A.; Tojo, J., Viscosities of Dimethyl Carbonate or Diethyl Carbonate with Alkanes at Four Temperatures. New UNIFAC−VISCO Parameters. *Journal of Chemical & Engineering Data* **2003,** *48* (1), 146-151.

7. Tang, S.; Zhao, H., Glymes as Versatile Solvents for Chemical Reactions and Processes: from the Laboratory to Industry. *RSC Advances* **2014,** *4* (22), 11251-11287.

8. Miller, J. R.; Simon, P., Materials Science - Electrochemical Capacitors for Energy Management. *Science* **2008,** *321* (5889), 651-652.

9. Simon, P.; Gogotsi, Y., Materials for electrochemical capacitors. *Nature Materials* **2008,** *7* (11), 845-854.

10. Zhao, E.; Qin, C.; Jung, H.-R.; Berdichevsky, G.; Nese, A.; Marder, S.; Yushin, G., Lithium Titanate Confined in Carbon Nanopores for Asymmetric supercapacitors. *ACS Nano* **2016,** *10* (4), 3977-3984.

11. Zhao, E.; Gu, W.; Yushin, G. Electrical Energy Storage: Supercapacitors. In *Handbook of Solid State Chemistry*; Richard, D.; Shinichi, K.; Andreas, S., Ed.; Wiley-VCH: Weinheim, 2017; Vol. 6; p 25.

12. Kim, H., Park, K.-Y., Cho, M.-Y., Kim, M.-H., Hong, J., Jung, S.-K., Roh, K. C., Kang, K., High-Performance Hybrid Supercapacitor Based on Graphene-Wrapped $Li_4Ti_5O_{12}$ and Activated Carbon. *ChemElectroChem* **2014,** *1* (1), 125-130.

13. Croguennec, L.; Palacin, M. R., Recent Achievements on Inorganic Electrode Materials for Lithium-Ion Batteries. *Journal of the American Chemical Society* **2015,** *137* (9), 3140-3156.

14. Amatucci, G. G.; Pereira, N., Fluoride Based Electrode Materials for Advanced Energy Storage Devices. *Journal of Fluorine Chemistry* **2007,** *128* (4), 243-262.

15. Hildebrand, J. H., Solubility. *Journal of the American Chemical Society* **1916,** *38* (8), 1452-1473.

16. Hildebrand, J. H., Solubility. III. Relative Values of Internal Pressures and Their Practical Application. *Journal of the American Chemical Society* **1919,** *41* (7), 1067-1080.

17. Abraham, D. P.; Spila, T.; Furczon, M. M.; Sammann, E., Evidence of Transition-Metal Accumulation on Aged Graphite Anodes by SIMS. *Electrochemical and Solid State Letters* **2008,** *11* (12), A226-A228.

18. Philippe, B.; Dedryvere, R.; Gorgoi, M.; Rensmo, H.; Gonbeau, D.; Edstrom, K., Role of the $LiPF_6$ Salt for the Long-Term Stability of Silicon Electrodes in Li-Ion Batteries - A Photoelectron Spectroscopy Study. *Chemistry of Materials* **2013,** *25* (3), 394-404.

19. El Ouatani, L.; Dedryvere, R.; Ledeuil, J. B.; Siret, C.; Biensan, P.; Desbrieres, J.; Gonbeau, D., Surface Film Formation on A Carbonaceous Electrode: Influence of the Binder Chemistry. *Journal of Power Sources* **2009,** *189* (1), 72-80.

20. Choi, N. S.; Han, J. G.; Ha, S. Y.; Park, I.; Back, C. K., Recent Advances in the Electrolytes for Interfacial Stability of High-Voltage Cathodes in Lithium-Ion Batteries. *RSC Advances* **2015,** *5* (4), 2732-2748.

21. Kang, E.; Jung, Y. S.; Kim, G. H.; Chun, J.; Wiesner, U.; Dillon, A. C.; Kim, J. K.; Lee, J., Highly Improved Rate Capability for a Lithium-Ion Battery Nano-$Li_4Ti_5O_{12}$ Negative Electrode via Carbon-Coated Mesoporous Uniform Pores with a Simple Self-Assembly Method. *Advanced Functional Materials* **2011,** *21* (22), 4349-4357.

22. Borghols, W. J. H.; Wagemaker, M.; Lafont, U.; Kelder, E. M.; Mulder, F. M., Size Effects in the $Li_{4+x}Ti_5O_{12}$ Spinel. *Journal of the American Chemical Society* **2009,** *131* (49), 17786-17792.

23. Lu, X.; Zhao, L.; He, X. Q.; Xiao, R. J.; Gu, L.; Hu, Y. S.; Li, H.; Wang, Z. X.; Duan, X. F.; Chen, L. Q.; Maier, J.; Ikuhara, Y., Lithium Storage in $Li_4Ti_5O_{12}$ Spinel: The Full Static Picture from Electron Microscopy. *Advanced Materials* **2012,** *24* (24), 3233-3238.

24. Prosini, P. P.; Mancini, R.; Petrucci, L.; Contini, V.; Villano, P., $Li_4Ti_5O_{12}$ as Anode in All-Solid-State, Plastic, Lithium-Ion Batteries for Low-Power Applications. *Solid State Ionics* **2001,** *144* (1-2), 185-192.

25. Shen, L. F.; Zhang, X. G.; Uchaker, E.; Yuan, C. Z.; Cao, G. Z., $Li_4Ti_5O_{12}$ Nanoparticles Embedded in a Mesoporous Carbon Matrix as a Superior Anode Material for High Rate Lithium Ion Batteries. *Advanced Energy Materials* **2012,** *2* (6), 691-698.

26. Hasegawa, G.; Kanamori, K.; Kiyomura, T.; Kurata, H.; Nakanishi, K.; Abe, T., Hierarchically Porous $Li_4Ti_5O_{12}$ Anode Materials for Li- and Na-Ion Batteries: Effects of Nanoarchitectural Design and Temperature Dependence of the Rate Capability. *Advanced Energy Materials* **2015,** *5* (1), 1400730.

27. Du, G. D.; Sharma, N.; Peterson, V. K.; Kimpton, J. A.; Jia, D. Z.; Guo, Z. P., Br-Doped $Li_4Ti_5O_{12}$ and Composite TiO_2 Anodes for Li-ion Batteries: Synchrotron X-Ray and in situ Neutron Diffraction Studies. *Advanced Functional Materials* **2011,** *21* (20), 3990-3997.

28. Zhang, Q. Y.; Lu, H. S.; Zhong, H. X.; Yan, X. D.; Ouyang, C. Y.; Zhang, L. Z., W^{6+} & Br^- Codoped $Li_4Ti_5O_{12}$ Anode with Super Rate Performance for Li-Ion Batteries. *Journal of Materials Chemistry A* **2015,** *3* (26), 13706-13716.

29. Choi, N.-S., Chen, Z., Freunberger, S. A., Ji, X., Sun, Y.-K., Amine, K., Yushin, G., Nazar, L. F., Cho, J., Bruce, P. G., Challenges Facing Lithium Batteries and Electrical Double-Layer Capacitors. *Angewandte Chemie International Edition* **2012,** *51* (40), 9994-10024.

30. Yu, L.; Wu, H. B.; Lou, X. W., Mesoporous $Li_4Ti_5O_{12}$ Hollow Spheres with Enhanced Lithium Storage Capability. *Advanced Materials* **2013,** *25* (16), 2296-2300.

31. Zhu, G. N.; Liu, H. J.; Zhuang, J. H.; Wang, C. X.; Wang, Y. G.; Xia, Y. Y., Carbon-Coated Nano-Sized $Li_4Ti_5O_{12}$ Nanoporous Micro-Sphere as Anode Material for High-Rate Lithium-Ion Batteries. *Energy & Environmental Science* **2011,** *4* (10), 4016-4022.

32. Amine, K.; Belharouak, I.; Chen, Z. H.; Tran, T.; Yumoto, H.; Ota, N.; Myung, S. T.; Sun, Y. K., Nanostructured Anode Material for High-Power Battery System in Electric Vehicles. *Advanced Materials* **2010,** *22* (28), 3052-3057.

33. Shen, L. F.; Uchaker, E.; Zhang, X. G.; Cao, G. Z., Hydrogenated $Li_4Ti_5O_{12}$ Nanowire Arrays for High Rate Lithium Ion Batteries. *Advanced Materials* **2012,** *24* (48), 6502-6506.

34. Liu, J.; Song, K. P.; van Aken, P. A.; Maier, J.; Yu, Y., Self-Supported $Li_4Ti_5O_{12}$-C Nanotube Arrays as High-Rate and Long-Life Anode Materials for Flexible Li-Ion Batteries. *Nano Letters* **2014,** *14* (5), 2597-2603.

35. Chen, S.; Xin, Y. L.; Zhou, Y. Y.; Ma, Y. R.; Zhou, H. H.; Qi, L. M., Self-Supported $Li_4Ti_5O_{12}$ Nanosheet Arrays for Lithium Ion Batteries with Excellent Rate Capability and Ultralong Cycle Life. *Energy & Environmental Science* **2014,** *7* (6), 1924-1930.

36. Ren, Y.; Armstrong, A. R.; Jiao, F.; Bruce, P. G., Influence of Size on the Rate of Mesoporous Electrodes for Lithium Batteries. *Journal of the American Chemical Society* **2010,** *132* (3), 996-1004.

37. Benson, J.; Kovalenko, I.; Boukhalfa, S.; Lashmore, D.; Sanghadasa, M.; Yushin, G., Multifunctional CNT-Polymer Composites for Ultra-Tough Structural Supercapacitors and Desalination Devices. *Advanced Materials* **2013,** *25* (45), 6625-6632.

38. Wang, G. P.; Zhang, L.; Zhang, J. J., A Review of Electrode Materials for Electrochemical Supercapacitors. *Chemical Society Reviews* **2012,** *41* (2), 797-828.

39. Snook, G. A.; Kao, P.; Best, A. S., Conducting-Polymer-Based Supercapacitor Devices and Electrodes. *Journal of Power Sources* **2011,** *196* (1), 1-12.

40. Zhi, M. J.; Xiang, C. C.; Li, J. T.; Li, M.; Wu, N. Q., Nanostructured Carbon-Metal Oxide Composite Electrodes for Supercapacitors: A Review. *Nanoscale* **2013,** *5* (1), 72-88.

41. Augustyn, V.; Simon, P.; Dunn, B., Pseudocapacitive Oxide Materials for High-Rate Electrochemical Energy Storage. *Energy & Environmental Science* **2014,** *7* (5), 1597-1614.

42. Acerce, M.; Voiry, D.; Chhowalla, M., Metallic 1T Phase Mos_2 Nanosheets as Supercapacitor Electrode Materials. *Nature Nanotechnology* **2015,** *10* (4), 313-318.

43. Mai, L. Q.; Yang, F.; Zhao, Y. L.; Xu, X.; Xu, L.; Luo, Y. Z., Hierarchical $MnMoO_4/CoMoO_4$ Heterostructured Nanowires with Enhanced Supercapacitor Performance. *Nature Communications* **2011,** *2*, 381.

44. Benson, J.; Boukhalfa, S.; Magasinski, A.; Kvit, A.; Yushin, G., Chemical Vapor Deposition of Aluminum Nanowires on Metal Substrates for Electrical Energy Storage Applications. *ACS Nano* **2012,** *6* (1), 118-125.

45. Boukhalfa, S.; Evanoff, K.; Yushin, G., Atomic Layer Deposition of Vanadium Oxide on Carbon Nanotubes for High-Power Supercapacitor Electrodes. *Energy & Environmental Science* **2012,** *5* (5), 6872-6879.

46. Wang, X. R.; Yushin, G., Chemical Vapor Deposition and Atomic Layer Deposition for Advanced Lithium Ion Batteries and Supercapacitors. *Energy & Environmental Science* **2015,** *8* (7), 1889-1904.

47. Presser, V.; Heon, M.; Gogotsi, Y., Carbide-Derived Carbons - From Porous Networks to Nanotubes and Graphene. *Advanced Functional Materials* **2011,** *21* (5), 810-833.

48. Kyotani, T.; Ma, Z. X.; Tomita, A., Template Synthesis of Novel Porous Carbons Using Various Types of Zeolites. *Carbon* **2003,** *41* (7), 1451-1459.

49. Borchardt, L.; Oschatz, M.; Kaskel, S., Tailoring Porosity in Carbon Materials for Supercapacitor Applications. *Materials Horizons* **2014,** *1* (2), 157-168.

50. Gogotsi, Y.; Nikitin, A.; Ye, H. H.; Zhou, W.; Fischer, J. E.; Yi, B.; Foley, H. C.; Barsoum, M. W., Nanoporous Carbide-Derived Carbon with Tunable Pore Size.

Nature Materials **2003,** *2* (9), 591-594.

51. Chen, Z.; Wen, J.; Yan, C. Z.; Rice, L.; Sohn, H.; Shen, M. Q.; Cai, M.; Dunn, B.; Lu, Y. F., High-Performance Supercapacitors Based on Hierarchically Porous Graphite Particles. *Advanced Energy Materials* **2011,** *1* (4), 551-556.

52. Strubel, P.; Thieme, S.; Biemelt, T.; Helmer, A.; Oschatz, M.; Bruckner, J.; Althues, H.; Kaskel, S., ZnO Hard Templating for Synthesis of Hierarchical Porous Carbons with Tailored Porosity and High Performance in Lithium-Sulfur Battery. *Advanced Functional Materials* **2015,** *25* (2), 287-297.

53. Jung, H. G.; Jang, M. W.; Hassoun, J.; Sun, Y. K.; Scrosati, B., A High-Rate Long-Life $Li_4Ti_5O_{12}/Li[Ni_{0.45}Co_{0.1}Mn_{1.45}]O_4$ Lithium-Ion Battery. *Nature Communications* **2011,** *2*, 516.

54. Wang, Y. Q.; Guo, L.; Guo, Y. G.; Li, H.; He, X. Q.; Tsukimoto, S.; Ikuhara, Y.; Wan, L. J., Rutile-TiO_2 Nanocoating for a High-Rate $Li_4Ti_5O_{12}$ Anode of a Lithium-Ion Battery. *Journal of the American Chemical Society* **2012,** *134* (18), 7874-7879.

55. Peng, S. J.; Li, L. L.; Wu, H. B.; Madhavi, S.; Lou, X. W., Controlled Growth of $NiMoO_4$ Nanosheet and Nanorod Arrays on Various Conductive Substrates as Advanced Electrodes for Asymmetric Supercapacitors. *Advanced Energy Materials* **2015,** *5* (2).

56. Ghidiu, M.; Lukatskaya, M. R.; Zhao, M. Q.; Gogotsi, Y.; Barsoum, M. W., Conductive Two-Dimensional Titanium Carbide 'Clay' with High Volumetric Capacitance. *Nature* **2014,** *516*, 78-81.

57. Yu, X. Z.; Lu, B. A.; Xu, Z., Super Long-Life Supercapacitors Based on the Construction of Nanohoneycomb-Like Strongly Coupled $CoMoO_4$-3D Graphene Hybrid Electrodes. *Advanced Materials* **2014,** *26* (7), 1044-1051.

58. Fu, W.; Zhao, E.; Sun, Z.; Ren, X.; Magasinski, A.; Yushin, G., Iron Fluoride–Carbon Nanocomposite Nanofibers as Free-Standing Cathodes for High-Energy Lithium Batteries. *Advanced Functional Materials* **2018**, *28*, 1801711.

59. Wu, F. X.; Yushin, G., Conversion Cathodes for Rechargeable Lithium and Lithium-Ion Batteries. *Energy & Environmental Science* **2017,** *10* (2), 435-459.

60. Ji, X. L.; Lee, K. T.; Nazar, L. F., A Highly Ordered Nanostructured Carbon-Sulphur Cathode for Lithium-Sulphur Batteries. *Nature Materials* **2009,** *8* (6), 500-506.

61. Li, Z.; Jiang, Y.; Yuan, L. X.; Yi, Z. Q.; Wu, C.; Liu, Y.; Strasser, P.; Huang, Y. H., A Highly Ordered Meso@Microporous Carbon-Supported Sulfur@Smaller Sulfur Core-Shell Structured Cathode for Li-S Batteries. *ACS Nano* **2014,** *8* (9), 9295-9303.

62. Wu, F. X.; Lee, J. T.; Zhao, E. B.; Zhang, B.; Yushin, G., Graphene-Li_2S-Carbon Nanocomposite for Lithium-Sulfur Batteries. *ACS Nano* **2016,** *10* (1), 1333-1340.

63. Wu, F. X.; Thieme, S.; Ramanujapuram, A.; Zhao, E. B.; Weller, C.; Althues, H.; Kaskel, S.; Borodin, O.; Yushin, G., Toward In-Situ Protected Sulfur Cathodes by Using Lithium Bromide and Pre-Charge. *Nano Energy* **2017,** *40*, 170-179.

64. Barghamadi, M.; Best, A. S.; Bhatt, A. I.; Hollenkamp, A. F.; Musameh, M.; Rees, R. J.; Ruther, T., Lithium-Sulfur Batteries-the Solution Is in the Electrolyte, but Is the Electrolyte a Solution? *Energy & Environmental Science* **2014,** *7* (12), 3902-3920.

65. Wu, F. X.; Lee, J. T.; Fan, F. F.; Nitta, N.; Kim, H.; Zhu, T.; Yushin, G., A Hierarchical Particle-Shell Architecture for Long-Term Cycle Stability of Li_2S Cathodes. *Advanced Materials* **2015,** *27* (37), 5579-5586.

66. Wu, F. X.; Kim, H.; Magasinski, A.; Lee, J. T.; Lin, H. T.; Yushin, G., Harnessing Steric Separation of Freshly Nucleated Li_2S Nanoparticles for Bottom-Up Assembly of High-Performance Cathodes for Lithium-Sulfur and Lithium-Ion Batteries. *Advanced Energy Materials* **2014,** *4* (11), 1400196.

67. Li, C. L.; Gu, L.; Tong, J. W.; Maier, J., Carbon Nanotube Wiring of Electrodes for High-Rate Lithium Batteries Using an Imidazolium-Based Ionic Liquid Precursor as Dispersant and Binder: A Case Study on Iron Fluoride Nanoparticles. *ACS Nano* **2011,** *5* (4), 2930-2938.

68. Li, C..; Mu, X.; Van Aken, P. A.; Maier, J., A High-Capacity Cathode for Lithium Batteries Consisting of Porous Microspheres of Highly Amorphized Iron Fluoride Densified from Its Open Parent Phase. *Advanced Energy Materials* **2013,** *3* (1), 113-119.

69. Gu, W.; Magasinski, A.; Zdyrko, B.; Yushin, G., Metal Fluorides Nanoconfined in Carbon Nanopores as Reversible High Capacity Cathodes for Li and Li-Ion Rechargeable Batteries: FeF_2 as an Example. *Advanced Energy Materials* **2015,** *5* (4),

1401148.

70. Li, L. S.; Yu, Y. H.; Meng, F.; Tan, Y. Z.; Hamers, R. J.; Jin, S., Facile Solution Synthesis of α-$FeF_3 \cdot 3H_2O$ Nanowires and Their Conversion to α-Fe_2O_3 Nanowires for Photoelectrochemical Application. *Nano Letters* **2012,** *12* (2), 724-731.

71. Wang, X. R.; Gu, W. T.; Lee, J. T.; Nitta, N.; Benson, J.; Magasinski, A.; Schauer, M. W.; Yushin, G., Carbon Nanotube-CoF_2 Multifunctional Cathode for Lithium Ion Batteries: Effect of Electrolyte on Cycle Stability. *Small* **2015,** *11* (38), 5164-5173.

72. Kim, H.; Lim, H. D.; Kim, S. W.; Hong, J.; Seo, D. H.; Kim, D. C.; Jeon, S.; Park, S.; Kang, K., Scalable Functionalized Graphene Nano-platelets as Tunable Cathodes for High-performance Lithium Rechargeable Batteries. *Scientific Reports* **2013,** *3*, 1506.

73. Kim, S. W.; Seo, D. H.; Gwon, H.; Kim, J.; Kang, K., Fabrication of FeF3 Nanoflowers on CNT Branches and Their Application to High Power Lithium Rechargeable Batteries. *Advanced Materials* **2010,** *22* (46), 5260-5264.

74. Badway, F.; Mansour, A. N.; Pereira, N.; Al-Sharab, J. F.; Cosandey, F.; Plitz, I.; Amatucci, G. G., Structure and Electrochemistry of Copper Fluoride Nanocomposites Utilizing Mixed Conducting Matrices. *Chemistry of Materials* **2007,** *19* (17), 4129-4141.

75. Li, H.; Richter, G.; Maier, J., Reversible Formation and Decomposition of LiF Clusters Using Transition Metal Fluorides as Precursors and Their Application in Rechargeable Li Batteries. *Advanced Materials* **2003,** *15* (9), 736-739.

76. Ma, D. L.; Cao, Z. Y.; Wang, H. G.; Huang, X. L.; Wang, L. M.; Zhang, X. B., Three-Dimensionally Ordered Macroporous FeF_3 and Its In Situ Homogenous Polymerization Coating for High Energy and Power Density Lithium Ion Batteries. *Energy & Environmental Science* **2012,** *5* (9), 8538-8542.

77. Anji, R. M.; Ben, B.; Kiran, C. V. S.; Clemens, W.; Michael, E.; Christian, K.; K., P. A.; Horst, H.; Maximilian, F., CF_x Derived Carbon–FeF_2 Nanocomposites for Reversible Lithium Storage. *Advanced Energy Materials* **2013,** *3* (3), 308-313.

78. Jost, K.; Perez, C. R.; McDonough, J. K.; Presser, V.; Heon, M.; Dion, G.; Gogotsi, Y., Carbon Coated Textiles for Flexible Energy Storage. *Energy & Environmental Science* **2011,** *4* (12), 5060-5067.

79. Li, N.; Chen, Z. P.; Ren, W. C.; Li, F.; Cheng, H. M., Flexible Graphene-Based Lithium Ion Batteries with Ultrafast Charge and Discharge Rates. *Proceedings of the National Academy of Sciences of the United States of America* **2012,** *109* (43), 17360-17365.

80. Zhou, G. M.; Li, F.; Cheng, H. M., Progress in Flexible Lithium Batteries and Future Prospects. *Energy & Environmental Science* **2014,** *7* (4), 1307-1338.

81. Liu, Y.; Zhou, J. Y.; Chen, L. L.; Zhang, P.; Fu, W. B.; Zhao, H.; Ma, Y. F.; Pan, X. J.; Zhang, Z. X.; Han, W. H.; Xie, E. Q., Highly Flexible Freestanding Porous Carbon Nanofibers for Electrodes Materials of High-Performance All-Carbon Supercapacitors. *ACS Applied Materials & Interfaces* **2015,** *7* (42), 23515-23520.

82. Abouali, S.; Garakani, M. A.; Zhang, B.; Xu, Z. L.; Heidari, E. K.; Huang, J. Q.; Huang, J. Q.; Kim, J. K., Electrospun Carbon Nanofibers with in Situ Encapsulated Co_3O_4 Nanoparticles as Electrodes for High-Performance Supercapacitors. *ACS Applied Materials & Interfaces* **2015,** *7* (24), 13503-13511.

83. Kim, H.; Wu, F. X.; Lee, J. T.; Nitta, N.; Lin, H. T.; Oschatz, M.; Cho, W. I.; Kaskel, S.; Borodin, O.; Yushin, G., In Situ Formation of Protective Coatings on Sulfur Cathodes in Lithium Batteries with LiFSI-Based Organic Electrolytes. *Advanced Energy Materials* **2015,** *5* (6), 1401792.

84. Gu, W.; Borodin, O.; Zdyrko, B.; Lin, H.; Kim, H.; Nitta, N.; Huang, J.; Magasinski, A.; Milicev, Z.; Berdichevsky, G.; Yushin, G., Lithium-Iron Fluoride Battery with In Situ Surface Protection. *Advanced Functional Materials* **2016,** *26* (10), 1507-1516.

85. Arai, H.; Okada, S.; Sakurai, Y.; Yamaki, J., Cathode Performance and Voltage Estimation of Metal Trihalides. *Journal of Power Sources* **1997,** *68* (2), 716-719.

86. Li, L. S.; Jacobs, R.; Gao, P.; Gan, L. Y.; Wang, F.; Morgan, D.; Jin, S., Origins of Large Voltage Hysteresis in High-Energy-Density Metal Fluoride Lithium-Ion Battery Conversion Electrodes. *Journal of the American Chemical Society* **2016,** *138* (8), 2838-2848.

87. Cho, J.; Kim, Y. J.; Park, B., Novel $LiCoO_2$ Cathode Material with Al_2O_3 Coating for a Li Ion Cell. *Chemistry of Materials* **2000,** *12* (12), 3788-3791.

88. Shaju, K. M.; Bruce, P. G., A Stoichiometric Nano-$LiMn_2O_4$ Spinel Electrode Exhibiting High Power and Stable Cycling. *Chemistry of Materials* **2008,** *20* (17),

5557-5562.

89. Lee, S.; Cho, Y.; Song, H. K.; Lee, K. T.; Cho, J., Carbon-Coated Single-Crystal $LiMn_2O_4$ Nanoparticle Clusters as Cathode Material for High-Energy and High-Power Lithium-Ion Batteries. *Angewandte Chemie-International Edition* **2012,** *51* (35), 8748-8752.

90. Qian, J. F.; Henderson, W. A.; Xu, W.; Bhattacharya, P.; Engelhard, M.; Borodin, O.; Zhang, J. G., High Rate and Stable Cycling of Lithium Metal Anode. *Nature Communications* **2015,** *6*, 6362.

91. Basile, A.; Bhatt, A. I.; O'Mullane, A. P., Stabilizing Lithium Metal Using Ionic Liquids for Long-Lived Batteries. *Nature Communications* **2016,** *7*, 11794.

92. Fan, X.; Zhu, Y.; Luo, C.; Suo, L. M.; Lin, Y.; Gao, T.; Xu, K.; Wang, C. S., Pomegranate-Structured Conversion-Reaction Cathode with a Built-in Li Source for High-Energy Li-Ion Batteries. *ACS Nano* **2016,** *10* (5), 5567-5577.

93. Wang, F.; Robert, R.; Chernova, N. A.; Pereira, N.; Omenya, F.; Badway, F.; Hua, X.; Ruotolo, M.; Zhang, R.; Wu, L.; Volkov, V.; Su, D.; Key, B.; Whittingharn, M. S.; Grey, C. P.; Amatucci, G. G.; Zhu, Y.; Graetz, J., Conversion Reaction Mechanisms in Lithium Ion Batteries: Study of the Binary Metal Fluoride Electrodes. *Journal of the American Chemical Society* **2011,** *133* (46), 18828-18836.

94. Yamakawa, N.; Jiang, M.; Key, B.; Grey, C. P., Identifying the Local Structures Formed during Lithiation of the Conversion Material, Iron Fluoride, in a Li Ion Battery: A Solid-State NMR, X-ray Diffraction, and Pair Distribution Function Analysis Study. *Journal of the American Chemical Society* **2009,** *131* (30), 10525-10536.

95. Li, C.; Yin, C.; Gu, L.; Dinnebier, R. E.; Mu, X.; van Aken, P. A.; Maier, J., An $FeF_3{\cdot}0.5H_2O$ Polytype: A Microporous Framework Compound with Intersecting Tunnels for Li and Na Batteries. *Journal of the American Chemical Society* **2013,** *135* (31), 11425-11428.

96. Wang, F.; Kim, S. W.; Seo, D. H.; Kang, K.; Wang, L.; Su, D.; Vajo, J. J.; Wang, J.; Graetz, J., Ternary Metal Fluorides as High-Energy Cathodes with Low Cycling Hysteresis. *Nature Communications* **2015,** *6*, 6668.

97. Li, C.; Gu, L.; Tong, J.; Tsukimoto, S.; Maier, J., A Mesoporous Iron-Based Fluoride

Cathode of Tunnel Structure for Rechargeable Lithium Batteries. *Advanced Functional Materials* **2011,** *21* (8), 1391-1397.

98. Makimura, Y.; Rougier, A.; Tarascon, J. M., Pulsed Laser Deposited Iron Fluoride Thin Films for Lithium-Ion Batteries. *Applied Surface Science* **2006,** *252* (13), 4587-4592.

99. Zheng, J.; Engelhard, M. H.; Mei, D.; Jiao, S.; Polzin, B. J.; Zhang, J.; Xu, W., Electrolyte Additive Enabled Fast Charging and Stable Cycling Lithium Metal Batteries. *Nature Energy* **2017,** *2* (3), 17012.

100. Pieczonka, N. P. W.; Yang, L.; Balogh, M. P.; Powell, B. R.; Chemelewski, K.; Manthiram, A.; Krachkovskiy, S. A.; Goward, G. R.; Liu, M.; Kim, J. H., Impact of Lithium Bis(oxalate)borate Electrolyte Additive on the Performance of High-Voltage Spinel/Graphite Li-Ion Batteries. *Journal of Physical Chemistry C* **2013,** *117* (44), 22603-22612.

101. Xu, M.; Tsiouvaras, N.; Garsuch, A.; Gasteiger, H. A.; Lucht, B. L., Generation of Cathode Passivation Films via Oxidation of Lithium Bis(oxalato) Borate on High Voltage Spinel ($LiNi_{0.5}Mn_{1.5}O_4$). *Journal of Physical Chemistry C* **2014,** *118* (14), 7363-7368.

102. Lei, D.; Lee, D.-C.; Magasinski, A.; Zhao, E.; Steingart, D.; Yushin, G., Performance Enhancement and Side Reactions in Rechargeable Nickel-Iron Batteries with Nanostructured Electrodes. *ACS Applied Materials & Interfaces* **2016,** *8* (3), 2088-2096.

103. Niu, X.; Sun, L.; Wang, Y.; Wu, H.; Xu, X., NF_3 Decomposition over Some Metal Oxides in the Absence of Water. *Journal of Natural Gas Chemistry* **2010,** *19* (5), 463-467.

104. Vileno, E.; Leclair, M. K.; Suib, S. L.; Cutlip, M. B.; Galasso, F. S.; Hardwick, S. J., Thermal-Decomposition of NF_3 by Ti, Si, and Sn Powders. *Chemistry of Materials* **1995,** *7* (4), 683-687.

105. Vileno, E.; LeClair, M. K.; Suib, S. L.; Cutlip, M. B.; Galasso, F. S.; Hardwick, S. J., Thermal Decomposition of NF_3 with Various Oxides. *Chemistry of Materials* **1996,** *8* (6), 1217-1221.

106. Xu, K.; Zhang, S.; Lee, U.; Allen, J. L.; Jow, T. R., LiBOB: Is It an Alternative Salt

for Lithium Ion Chemistry? *Journal of Power Sources* **2005,** *146* (1), 79-85.

107. Xu, K.; Zhang, S.; Jow, T. R., LiBOB as Additive in $LiPF_6$-Based Lithium Ion Electrolytes. *Electrochemical and Solid-State Letters* **2005,** *8* (7), A365-A368.

108. Xu, K., Tailoring Electrolyte Composition for LiBOB. *Journal of the Electrochemical Society* **2008,** *155* (10), A733-A738.

109. Xiao, A.; Yang, L.; Lucht, B. L.; Kang, S. H.; Abraham, D. P., Examining the Solid Electrolyte Interphase on Binder-Free Graphite Electrodes. *Journal of the Electrochemical Society* **2009,** *156* (4), A318-A327.

110. Xu, M.; Zhou, L.; Hao, L.; Xing, L.; Li, W.; Lucht, B. L., Investigation and Application of Lithium Difluoro(oxalate)borate (LiDFOB) as Additive to Improve the Thermal Stability of Electrolyte for Lithium-Ion Batteries. *Journal of Power Sources* **2011,** *196* (16), 6794-6801.

VITA

Enbo Zhao

Enbo was born in Mudanjiang, China. He received his B.S. from Po-ling Class (chemistry division) at Nankai University in 2013 before flying to the U.S. for his Ph.D. During college, Enbo had a chance to study at University of California, Berkeley for a summer, which was his first time stepping to the world outside China. Throughout graduate school at Georgia Tech, he has been looking for his future and had some trials in different industries, but he hasn't yet found the best path that fits him. Putting his career aside, Enbo enjoys exploring every corner of the world with his family and friends.